Synthesis of Silver and Platinum Nanocrystals and Surface Modifications of Gold Nanocrystals

A Dissertation
Presented to
The Academic Faculty

by

Shan Zhou

In Partial Fulfillment
of the Requirements for the Degree
of Doctor of Philosophy in the
School of Chemistry and Biochemistry

Georgia Institute of Technology
August 2018

Synthesis of Silver and Platinum Nanocrystals and Surface Modifications of Gold Nanocrystals

Approved by:

Dr. Younan Xia, Advisor
School of Chemistry and Biochemistry
Department of Biomedical Engineering
Georgia Institute of Technology

Dr. Jake D. Soper
School of Chemistry and Biochemistry
Georgia Institute of Technology

Dr. Angus P. Wilkinson
School of Chemistry and Biochemistry
Georgia Institute of Technology

Dr. Z. John Zhang
School of Chemistry and Biochemistry
Georgia Institute of Technology

Dr. Meilin Liu
School of Materials Science and Engineering
Georgia Institute of Technology

Date Approved: July 16, 2018

Dedicated to my parents, Yuting Luo and Maoli Zhou,

for their endless love and support.

ACKNOWLEDGEMENTS

The fulfillment of this dissertation would not be possible without the contributions from many wonderful people. First and foremost, I would like to acknowledge my PhD advisor, Prof. Younan Xia, for constantly mentoring, motivating and stimulating my research with great patience, enthusiasm and knowledge. He has greatly improved my critical thinking and scientific writing skills, as well as my overall independence in research. I would also like to express my gratitude to Prof. Angus P. Wilkinson, Prof. Z. John Zhang, Prof. Jake. D. Soper and Prof. Meilin Liu for serving on my dissertation committee, and for being always helpful and supportive.

My interest in noble-metal nanocrystals was initially sparked by Prof. Yujie Xiong and Dr. Ran Long during my undergraduate studies at the University of Science and Technology of China (USTC). I am sincerely grateful for their guidance and encouragement. Throughout the graduate school, many individuals have inspired me personally and professionally. Here, I would like to express my deepest gratitude to: Prof. Dong Qin, Dr. Da Huo, Dr. Tung-Han Yang, Dr. Zachary Hood, Dr. Kyle Gilroy, Dr. Xuan Yang, Dr. Miaoxin Yang, Dr. Shixiong Bao, Ming Zhao, Chi-Ta Lee, Dr. Hsin-Chieh Peng, Dr. Jiajia Xue, Zhiheng Lyu, Dr. Jing Qian, Xiaohuan Zhao, Haoyan Cheng, Wenxia Wang, Yiren Wu, Wenjuan Shang, Whitney Breech, and many other friends, for their tremendous help and encouragement.

At last, I would like to sincerely thank my parents, Yuting Luo and Maoli Zhou, for their endless support and unconditional love.

TABLE OF CONTENTS

LIST OF TABLES

LIST OF FIGURES

LIST OF SYMBOLS AND ABBREVIATIONS

AA	Ascorbic acid
Ag	Silver
Au	Gold
CMC	Critical micelle concentration
CTAB	Cetyltrimethylammonium bromide
CTAC	Cetyltrimethylammonium chloride
DDA	Discrete dipole approximation
DEG	Diethylene glycol
DI	Deionized
EDX	Energy dispersive X-ray spectroscopy
EF	Enhancement factor
EG	Ethylene glycol
FAO	Formic acid oxidation
FT	Fourier transform
HRTEM	High-resolution transmission electron microscopy
ICP-MS	Inductively-coupled plasma mass spectrometry
IR	Infrared spectroscopy
k	Rate constant
LSPR	Localized surface plasmon resonance
Na_3CA	Sodium citrate
ORR	Oxygen reduction reaction
Pd	Palladium

Pt	Platinum
PEG	Poly(ethylene glycol)
PVP	Poly(vinylpyrrolidone)
r_0	Initial reduction rate
SEM	Scanning electron microscopy
SERS	Surface enhanced Raman spectroscopy
TEM	Transmission electron microscopy
UV-vis	Ultraviolet-visible
XPS	X-ray photoelectron spectroscopy
XRD	X-ray diffraction
γ	Surface free energy

SUMMARY

Noble-metal nanocrystals with controlled sizes, shapes and surface properties have received considerable interests owing to their extensive use in applications related to plasmonics, electronics, catalysis, and biomedicine. This dissertation is focused on development of synthetic methods for tightly controlling the shape of nanocrystals and for modifying their surface properties. I begin by demonstrating two methods for shape-controlled synthesis, including one-pot synthesis and seed-mediated growth, to obtain Ag nanocubes with sharp corners and edges in a water-based system. I then demonstrate an indirect ligand exchange method for effectively replacing the surface ligands on Au nanocrystals with different morphologies. Finally, I conduct a quantitative analysis of the reduction kinetics to establish the relationship between the reduction pathways and the final morphologies taken by the Pt nanocrystals. This dissertation concludes by highlighting opportunities and perspectives for future research. The approaches elaborated in this work can provide guidelines for the rational design of nanocrystal synthesis to achieve precise control over the shape and surface properties of the products.

CHAPTER 1

INTRODUCTION

1.1 Noble-Metal Nanocrystals and Their Applications

Noble-metal nanocrystals with well-controlled shapes have received ever increasing attentions for both fundamental studies and industrial applications [1-3]. Many of them have been extensively explored for photonics [4-6], electronics [7,8], energy conversion/storage [9], biomedicine [10], and catalysis [11-14]. For example, both silver (Ag) and gold (Au) nanocrystals have unique localized surface plasmon resonance (LSPR) properties [15,16]. The LSPR is a phenomenon arising from the collective oscillations of conduction electrons in a metal nanocrystal stimulated by the oscillating electric field of the incident light. The number and position of the LSPR peaks are dependent on the size, shape, and the surrounding medium of the nanocrystal [17,18]. The LSPR properties of Au and Ag nanocrystals make them well-suited for surface-enhanced Raman spectroscopy (SERS) applications [19]. By functionalizing the surface of nanocrystals with the probe molecules, it is possible to obtain enhancement for the SERS peaks. Mosquera *et al.* measured the enhancement factor of 4-nitrobenzenethiol immobilized on Au decahedral nanocrystals with an average edge length of 30 nm, and the value was measured to be 7.3×10^6 [20]. The enhanced signals exhibited by the Au decahedral nanocrystals were ascribed to sharp tips and edges present on the surface of the nanocrystals. In addition to Au, Ag nanocrystals such as Ag nanocubes and their dimers [21], nanorods [22], nanoplates [23], decahedrons [24], and immobilized nanocrystals [25] have also shown significantly enhanced SERS activity.

In addition to the unique optical properties, noble-metal nanocrystals have also been widely used in various catalytic reactions. For example, one particular electrochemical reaction that has received considerable attention is oxygen reduction reaction (ORR), which plays an important role in the development of clean energy technologies [3]. The platinum (Pt) nanocrystals and Pt hollow nanocages showed significantly enhanced activity toward ORR relative to the state-of-art Pt/C commercial catalysts [26]. Formic acid oxidation (FAO) is another important electrocatalytic reaction that has received considerable attention recently owing to its lower toxicity and crossover flux compared with methanol oxidation [27]. Our group demonstrated that palladium (Pd) icosahedra exhibited enhanced activity towards the FAO reaction [28]. Noble-metal nanocrystals have also shown enhanced activities and/or selectivities in many other catalytic reactions, such as CO oxidation [29], CO_2 reduction [30], Suzuki coupling reaction [31], glucose oxidation [32], ethylene epoxidation [33,34], etc.

Due to the relatively low abundances of these noble metals in the Earth's crust and high prices, there is an urgent need to develop strategies to utilize them more efficiently. The size, shape, internal structure and surface chemistry taken by a noble-metal nanocrystal can significantly influence its physicochemical properties and therefore determines its performances in the aforementioned applications. Over the past decade, many research efforts have been devoted to achieving tight control over noble-metal nanocrystals to optimize their performances. Now we can easily access noble-metal nanocrystals with diversified but well-defined shapes or morphologies; notable examples include spheres [35], tetrahedrons [36], cubes [37-40], octahedrons [41], cuboctahedrons [42],

dodecahedrons [43], decahedrons [44-46], icosahedrons [46], trisoctahedrons [47], and tetrahexahedrons [48,49].

1.2 Controlling the Shape and Surface Properties of Nanocrystals

The shape and surface properties of noble-metal nanocrystals can greatly influence their performance in photonics, catalysis, and sensing. For example, the exposed facets, with typical examples including {100}, {110}, and {111}, ultimately define the active sites on the noble-metal nanocrystals for catalysis [50]. Our group have systematically explored the FAO activities of Pd nanocrystals enclosed with different facets and/or structures using the same setup and under essentially identical conditions [28]. In terms of Pd nanocrystals with a single-crystal structure, the cubes enclosed by {100} facets exhibited enhancement in specific activity relative to both the octahedrons and tetrahedrons enclosed by {111} facets.

The surface property of nanocrystals is also an important factor in determining their performances in optical [51], catalytic [52], and biomedical applications [53], as well as their self-assembly behavior [54]. Nanocrystals obtained from wet chemical synthesis often have surface ligands (*i.e.*, stabilizer and capping agent) which are used to direct growth or prevent aggregation [1,55,56]. Post-synthesis surface modifications with targeting surface molecules are often needed in order to achieve desired functionalities [57-67]. In biomedical applications, nanocrystals have to be delivered to the site of interest without being accumulated in healthy tissues and organs. Surface modifications using poly(ethylene glycol) (PEG) is widely used to mask nanocrystals from clearance by

reticuloendothelial system, helping the nanocrystals circulate in bloodstream for a long period of time and preferentially accumulate at target area [66].

To better control the shape and surface properties of noble-metal nanocrystals, it is necessary to understand the fundamentals of how these nanocrystals are synthesized. Noble-metal nanocrystals are often prepared in aqueous or non-aqueous solutions by the reduction of a dissolved metal precursor with a reducing agent. The synthesis is often conducted in the presence of a stabilizing agent, which can prevent the nanocrystals from aggregation. Some ionic species, small molecules, or macromolecules can also be introduced into the reaction system, to act as a facet-directing capping agent, or to regulate the reduction kinetics [68-70]. By controlling the nucleation and growth events through careful design of the reaction system, one can achieve a tight control over the shape of the final products. Post-synthesis methods can also be adopted to alter the surface properties of nanocrystals for further use in various applications, which will be discussed in the following sections.

1.2.1 Fundamentals of Nucleation and Growth

The formation of nanocrystals starts from nucleation, which is the formation of a new thermodynamic phase from an old phase with high Gibbs free energy. Classical nucleation theory has been widely used to describe the nucleation of noble-metal nanocrystals. The theory was originally proposed to describe the condensation of liquid from the vapor phase, but was then transferred to the synthesis of nanocrystals by LaMer and his colleagues. According to the LaMer theory, the nucleation can be divided into three stages: *i)* production of monomers as the building blocks for nanocrystals, *ii)* rapid aggregation of

the monomers into nuclei after reaching the level of supersaturation *via* homogeneous nucleation, and *iii)* growth of nuclei into seeds and the nanocrystals [71]. For noble-metal nanocrystals, the monomers typically refer to atoms at the zero valence state [1]. When the concentration of metal atoms increases and reach supersaturation, the nuclei will be rapidly generated and then continue to grow in an accelerated manner while the concentration of metal atoms quickly drops. If the concentration of atoms drops quickly below the minimum supersaturation concentration, no additional nucleation event would occur. The nuclei will keep growing into seeds and finally nanocrystals. Besides the homogeneous nucleation, the growth of nanocrystals can also occur through heterogeneous nucleation when there are external surfaces or pre-formed seeds present in the solution [70]. These external surfaces can significantly reduce the surface free energy and thus lower the energy barrier for nucleation.

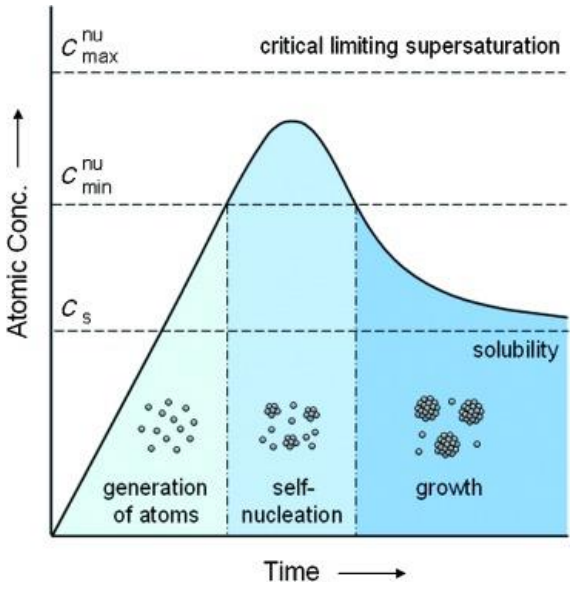

Figure 1.1. LaMer plot showing the atomic concentration as a function of time. (Reprinted with permission from [1]. Copyright 2008 Wiley-VCH.)

However, it is still unclear how the metal precursor is reduced to atoms for their evolution into nuclei, seeds, and then nanocrystals. It has been challenging to resolve the details of such a process due to the lack of analytical tools [72,73]. Recently, my colleagues and I used reduction kinetics to quantitatively study the reduction pathways of metal precursors in the synthesis of Pd nanocrystals [70]. As illustrated in Figure 1.2, the reduction of a metal precursor can take two completely different pathways during a synthesis of metal nanocrystals. When the metal ions are introduced into a solution containing a reductant and growing nanocrystals (or preformed seeds), they can be directly reduced to atoms in the solution phase through collision and electron transfer with the reductant molecules (Figure 1.2a, solution pathway) [74]. The resultant atoms then undergo homogeneous or heterogeneous nucleation, with the latter being more favorable due to its lower activation energy barrier. At the beginning of a one-pot synthesis, solution-phase reduction should be the only option for the salt precursor for the formation of nuclei/seeds through homogeneous nucleation. However, once seeds have been formed (or in the case of seed-mediated growth with the introduction of preformed seeds), the reduction of a metal precursor can undertake an alternative mechanism (Figure 1.2b, surface pathway). In this case, the precursor ions first adsorb onto the surface of a growing nanocrystal or a preformed seed, followed by their reduction to atoms [75-78]. These two reduction pathways can result in completely different types of products, with the second pathway capable of excluding the possible involvement of homogeneous nucleation, preventing the formation of self-nucleated products. Our quantitative analyses of the reduction kinetics of $PdCl_4^{2-}$ and $PdBr_4^{2-}$ by ascorbic acid at room temperature in the absence and presence of Pd nanocubes, respectively, suggesting that $PdCl_4^{2-}$ was reduced in the solution phase

while $PdBr_4^{2-}$ was reduced on the surface of a growing nanocrystal. Our results also demonstrate that the reduction pathway of $PdBr_4^{2-}$ by ascorbic acid could be switched from surface to solution by raising the reaction temperature. Kinetics studies have also been conducted to study how Pd precursor would be reduced in the presence of Pd seeds enclosed by different types of facets and with different crystal structures. However, the quantitative understanding of the exact reduction pathways is still under development for the formation of nanocrystals with compositions other than Pd.

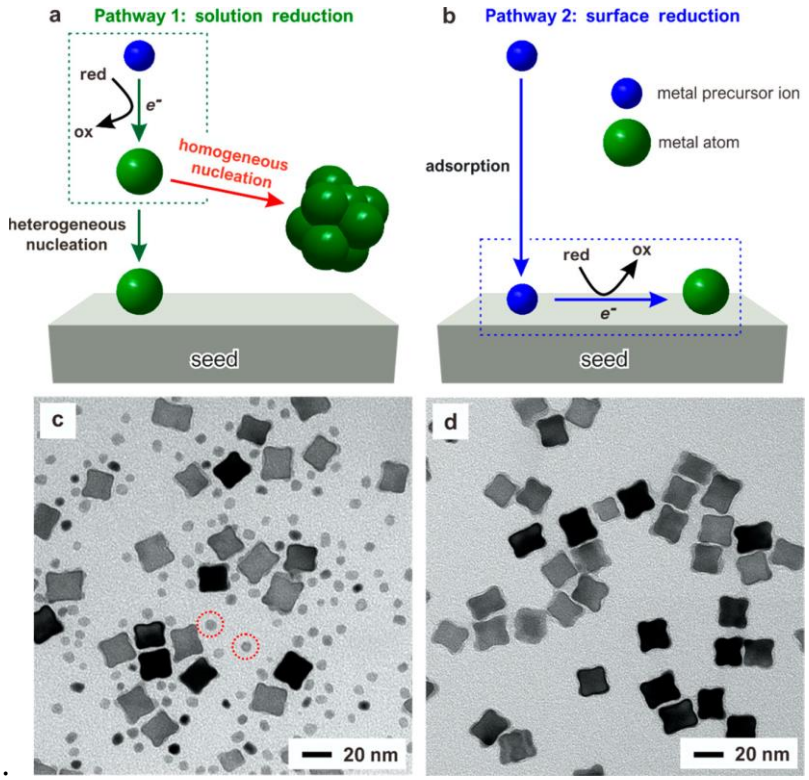

Figure 1.2. Two different reduction pathways involved in a seed-mediated synthesis. (a, b) Schematic illustrations of the reduction pathways (solution reduction *vs.* surface reduction) for a precursor ion in the seed-mediated growth of metal nanocrystals. (c, d) TEM images of products obtained when (c) $PdCl_4^{2-}$ and (d) $PdBr_4^{2-}$ were used as precursors, respectively, in the presence of 18-nm Pd cubic seeds. The smaller particles marked in panel (c) were formed through homogeneous nucleation. (Reprinted with permission from [70]. Copyright 2017 American Chemical Society.)

1.2.2 Relationship between the Shape of Nanocrystal and Reduction Kinetics

In a typical solution-phase synthesis, it is rare to obtain products that exhibit a minimum in the overall Gibbs free energy. This fact can be attributed to the relatively high energy barriers for atom diffusion to achieve shape transformation compared to the thermal energy involved in a typical synthesis. As a result, most of the protocols developed for synthesizing nanocrystals can well preserve the symmetry of the nulcei and are simply controlled by the reaction kinetics, rather than the thermodynamics. With the synthesis of Pd nanocrystals as an example, we demonstrated that the initial reduction rate of the precursor was crucial to the formation of products with a particular shape in high purity [79]. As shown in Figure 1.3, the percentages of Pd nanocrystals with different internal defect structures (*i.e.*, icosahedrons, plates, cuboctahedrons) as a function of the initial reduction rate of $PdCl_4^{2-}$ indicate that different shapes are favored at specific regimes of reduction rate.

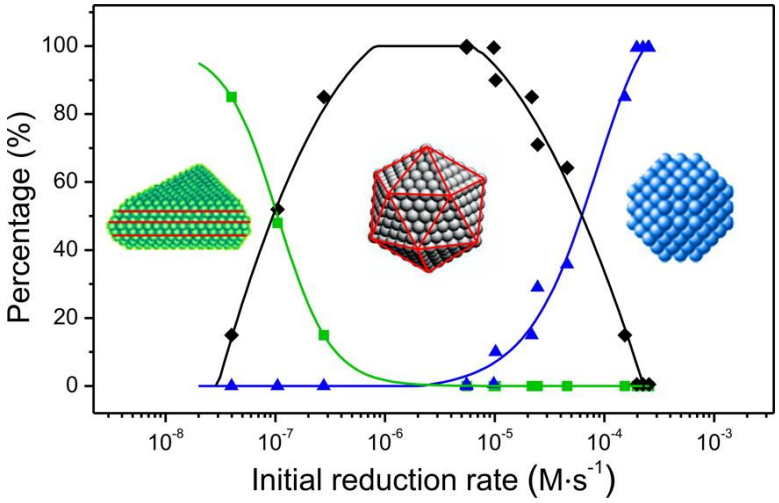

Figure 1.3. A plot showing the population of Pd nanocrystals as a function of the initial reduction rate (r_0) of a synthesis. The percentages of single-crystal cuboctahedrons, multiply twinned icosahedrons, and plates with stacking faults are denoted in blue, black,

and green colors, respectively. (Reprinted with permission from [79]. Copyright 2017 American Chemical Society.)

While reduction kinetics have been proposed to be an important factor in determining the structure and shape of nanocrystals based on the observations from wet-chemical synthesis, there are only limited number of papers reporting a quantitative insight into the relationship [70,79-81]. Acquiring a quantitative understanding of the reduction kinetics for the synthesis of other noble-metal nanocrystals (such as Pt, Ag or Au) will offer important insights into the rational design of the reaction system to achieve their shape control.

1.2.3 Polyol Synthesis vs. Aqueous Synthesis

The current solution-based synthetic strategies for noble-metal nanocrystals can be categorized based on the solvents involved. There are a variety of solvents that are commonly used, including water and organic solvents such as polyol [82], oleic acid/oleylamine [83,84], and toluene [85], among others. Polyols are alcohols with multiple hydroxyl groups, and can thus act as both the solvents and reducing agents. The most common polyols for the synthesis of noble-metal nanocrystals are ethylene glycol and diethylene glycol. A high reaction temperature (140-160 °C) is often needed to activate the reducing power of the polyols. Taking the synthesis of Ag nanocrystals as an example, polyol synthesis might be the most popular method to obtain Ag nanocrystals with distinct shapes such as nanospheres, tetrahedrons, nanocubes, nanobars, and nanowires [86-89].

Despite of the success of polyol synthesis in fabricating noble-metal nanocrystals, the use of an organic solvent always brings the safety/toxicity concerns and the potential environmental issues. Furthermore, many synthetic approaches based on polyols

sometimes suffer reproducibility issues. For example, the batch and manufacturer of the solvent can significantly influence the outcome of a synthesis. Water, as an environmentally friendly solvent with the most abundant supply, can avoid the safety concerns and reduce the cost of the solvent [90]. At the meantime, water-based methods can avoid the impurities that might originate from the manufacture of organic solvents, thus enhancing the reproducibility of a synthesis. The typically lower reaction temperature involved in an aqueous synthesis can also provide an opportunity to obtain nanocrystals adopting shapes with sharp corners and edges that are not readily accessible using the polyol synthesis.

1.2.4 One-pot Synthesis vs. Seed-mediated Growth

The synthetic strategies for noble-metal nanocrystals can also be divided into two types: one-pot synthesis and seed-mediated growth. In the one-pot synthesis, the homogeneous nucleation and nanocrystal growth occur in the same batch of reaction. While it is easy to conduct a one-pot synthesis, the optimal parameters for the nucleation and growth processes might be different, posing obstacles to obtaining nanocrystals with a uniform size, shape, and internal structure. Alternatively, seed-mediated growth separates the nucleation and growth events by synthesizing seeds first, and then employing them for further growth [91]. This method can thus offer an opportunity to individually fine tune the reaction parameters for both the homogeneous nucleation and growth. The careful control over the growth also makes it possible to produce nanocrystals with well-controlled compositions, sizes, structures, and shapes.

Although the concept of seed-mediated growth is simple, there are still several challenges to be addressed [91]. The first concern is that reaction parameters such as the type and concentration of the chemicals, temperature, and pH value need to be properly chosen to avoid homogeneous nucleation during the seed-mediated growth. Secondly, the as-synthesized seeds are sometimes needed to be collected and washed before they can be used for further growth. During these processes, the surface properties of the seeds can drastically change, and the metal seeds might be oxidized if exposing to O_2, leading to substantial changes to the shape or the structure of the seeds. Additionally, a redox reaction known as galvanic replacement can occur if the metal precursor has a higher reduction potential compared to that of the seed metal. It is necessary to carefully choose the proper metal precursor, use foreign ligands (such as halides), or use stronger reducing agent to suppress the galvanic replacement.

1.2.5 Effects of Facet-selective Capping

Capping agents are ionic species, small molecules, or macromolecules that can selectively bind to certain facets on the nanocrystals. In a solution-phase synthesis of noble-metal nanocrystals, facet-specific capping can profoundly influence the shape of the final products [1]. The use of a capping agent can reduce the surface free energy (γ) of the targeted facet through chemisorption. For Ag nanocrystals in the absence of capping agents, the surface free energies of low-index facets increase in the following order: $\gamma\{111\} < \gamma\{100\} < \gamma\{110\}$ [92]. This means the {111} facets are the most thermodynamically stable, and the other facets will gradually be replaced with {111} during the growth of seeds. The surface free energies of the low-index facets can be altered by introducing capping agents, and thus leading to the formation of nanocrystals enclosed

by different facets. For example, our group has studied the role played by different capping agents in the evolution of Ag nanocrystals [93]. The experiments were carried out under the same conditions except for using poly(vinylpyrrolidone) (PVP) or sodium citrate (Na_3CA). As can be seen from Figure 1.4, when using Na_3CA as a capping agent, spherical seeds evolved into octahedrons, while use of PVP led to the formation of cubes and nanobars. The PVP molecule was reported to selectively adsorb onto the Ag(100) facets and can greatly lower their surface free energy, resulting in the formation of nanocubes or nanobars enclosed by {100} facets. In contrast, citrate ions have been reported to selectively stable the Ag(111) facets, leading to the formation of Ag octahedrons enclosed by {111} surfaces.

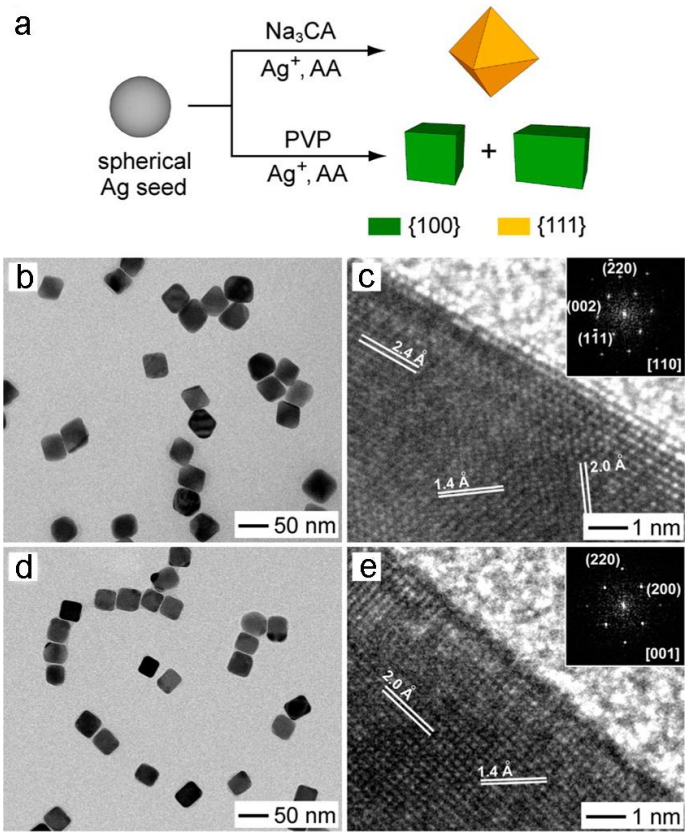

Figure 1.4. (a) Schematic showing the growth of a spherical Ag seed in the presence of citrate or PVP as the capping agent. (b) TEM and (c) HRTEM images of Ag octahedrons obtained using citrate. (d) TEM and (e) HRTEM images of Ag cubes and short bars obtained using PVP. (Reprinted with permission from [92]. Copyright 2012 American Chemical Society.)

There are a variety of facet-selective capping agents commonly used for the synthesis of noble-metal nanocrystals in addition to the above-mentioned PVP and citrate ions. For example, I^- ions has been identified as an effective capping agent toward Pd(100) and Au(111) surfaces; Br^- ions act as effective capping agent toward Pd(100), Pt(100), Rh(100) and Ag(100) surfaces; CO has selectivity binding toward Pt(100) and Pd(111) surfaces [91]. Taken together, facet-selective capping is a simple and effective method for achieving the shape-controlled synthesis of noble-metal nanocrystals.

1.2.6 Surface Modifications

Nanocrystals obtained from a wet-chemical synthesis are inevitably covered by capping agents and/or stabilizers. In order to achieve a targeted surface functionality, post-synthesis methods are needed to replace the surface ligands. The most commonly used protocol for achieving the replacement of surface molecules is direct ligand exchange [57,67]. In this protocol, the nanocrystals capped with the original ligand are collected and then directly re-dispersed in a solution of the targeted ligand, followed by shaking or incubation for a long time. The driving force for direct ligand exchange is the difference in binding energies of two ligands toward the nanocrystal surface, so it is difficult to completely replace one surface ligand with another one. Our group has quantitatively analyzed a process known as PEGylation to modify the surface of Au nanocrystals originally capped by different ligands with poly(ethylene glycol) [67]. The result shows that the variance in binding strengths of different ligands plays an important role in completing the PEGylation process. The final coverage density of HS-PEG-NH_2 was found to decrease significantly when the binding between the original ligand and Au nanocrystals was stronger. The direct ligand exchange may also cause severe aggregation in a suspension of colloidal nanocrystals when the two ligands carry opposite charges.

In addition to the conventional direct ligand exchange method, a few other approaches to the removal of the original surface ligand have also been reported, with notable examples including acid treatment [94], sonication [94], solvent extraction [95], and chemical oxidation [96-99]. However, only incomplete removal could be achieved in order to prevent the nanocrystals from aggregation, which means it still relies on the direct replacement when introducing the desired surface ligand, posing the similar challenges as the conventional one-step method.

1.3 Scope of This Work

The aim of this work is to develop synthetic methods to obtain noble-metal nanocrystals with desired sizes and shapes through precisely control over the reduction kinetics and/or rational design of the reaction systems, and to develop post-synthesis ligand exchange methods to precisely control the surface properties of these nanocrystals. This dissertation is organized into three parts: *i)* developing synthetic approaches (both one-pot synthesis and seed-mediated growth) to obtain Ag nanocubes with controllable sizes while maintaining sharp corners and edges in aqueous systems, *ii)* developing an indirect ligand exchange method to achieve complete ligand exchange on the surface of Au nanocrystals, and *iii)* understanding the correlation between the reduction kinetics and the outcome of a synthesis of Pt nanocrystal.

In Chapter 2, I describe a one-pot method for the synthesis of Ag nanocubes with an average edge length of 35-95 nm in an aqueous system. It involves the formation of AgCl octahedra by mixing CF_3COOAg with cetyltrimethylammonium chloride (CTAC), followed by the nucleation and growth of Ag nanocrystals in the presence of ascorbic acid (AA) and $FeCl_3$. The Fe^{3+}/Fe^{2+} redox pair is responsible for the removal of multiply twinned seeds through oxidative etching. The Cl^- ions play two critical roles in the nucleation and growth of Ag nanocubes with a single-crystal structure. Firstly, the Cl^- ions react with Ag^+ ions to generate nanometer-sized AgCl octahedra in the initial stage of a synthesis. In the presence of room light and a proper reducing agent such as AA, the AgCl can be reduced to generate Ag_n nuclei, followed by their evolution into single-crystal seeds and then Ag nanocrystals. Secondly, the Cl^- ions can act as a specific capping toward the Ag(100) surface, enabling the formation of Ag nanocubes with sharp corners and edges.

Based on the results from a set of time-elapse studies and control experiments, I formulate a plausible mechanism to account for the formation of Ag nanocubes, which resembles the formation and development of latent image centers in silver halide grains in the photographic process.

In Chapter 3, I demonstrate the use of a site-selective growth to sharpen the corners and edges of truncated Ag nanocubes with sizes down to 18 nm, followed by their elongation into nanobars with aspect ratios up to 2. The key to the success of this synthesis is the site-selective deposition at corners and edges, as enabled by CTAC. While CTA^+ is an effective colloidal stabilizer, Cl^- can react with Ag^+ to generate AgCl precipitates, slowing down the reduction kinetics. In addition, Cl^- can serve as a facet-selective capping agent towards the {100} side faces and thereby confine the growth mainly to corners and edges. Interestingly, once all the corners and edges have been sharpened, the growth is switched to an asymmetric mode to favor deposition on one of the six side faces only, leading to the formation of Ag nanobars with controllable aspect ratios. The symmetry reduction takes place as a result of the limited supply of Ag atoms, the strong capping of Cl^- ions toward the {100} facets, and the possible involvement of localized oxidative etching caused by Cl^-/O_2. I also demonstrate that the Ag nanocubes with sharp corners and edges can serve as a better sacrificial template than their truncated counterparts in generating Au hollow nanostructures with ultrathin walls.

In Chapter 4, I report an indirect method for the effective replacement of ligands on the surface of Au nanocrystals with different morphologies. The method involves the deposition of an ultrathin layer of Ag to remove a strong capping agent such as CTAC, followed by selective etching of the Ag layer in the presence of citrate ions as a stabilizer.

Using multiple characterization techniques, I confirm that the surface of the Au nanocrystals is solely covered by citrate ions after the indirect ligand exchange process, and there is essentially no aggregation during the entire process. I also demonstrate that this method is effective in suppressing the toxicity of Au nanospheres by completely replacing the initially used CTAC with citrate.

In Chapter 5, I report a quantitative analysis of how a Pt(II) precursor is reduced to atoms at different temperatures for the formation of Pt nanocrystals with different morphologies and sizes. My results suggest that in the early stage of a synthesis, the Pt(II) precursor is reduced to atoms exclusively in the solution phase, followed by homogeneous nucleation to generate nuclei and then seeds. At a relatively low reaction temperature such as 22 ^{o}C, the growth of the seeds is dominated by autocatalytic, surface reduction that involves the adsorption and then reduction of the Pt(II) precursor on the surface of the just-formed seeds. This particular growth pathway results in relatively large assemblies of Pt nanocrystals. When the reaction temperature is increased to 100 ^{o}C, the dominant reduction pathway will be switched from surface to solution phase, producing much smaller assemblies of Pt nanocrystals. My results also demonstrate that a similar trend applies to the seed-mediated growth of Pt nanocrystals in the presence of Pd nanocubes.

1.4 Notes to Chapter 1

Parts of this chapter are adapted from "Facile Synthesis of Silver Nanocubes With Sharp Corners and Edges in an Aqueous Solution" published in *ACS Nano* [100], "Site-selective Growth of Ag Nanocubes for Sharpening Their Corners and Edges, Followed by Elongation into Nanobars through Symmetry Reduction" published in *Journal of Materials*

Chemistry C [101], "Enabling Complete Ligand Exchange on the Surface of Gold Nanocrystals through the Deposition and then Etching of Silver" recently submitted for publication, "Quantitative Analysis of the Reduction Kinetics of a Pt(II) Precursor in the Context of Pt Nanocrystal Synthesis" accepted by *Chinese Journal of Chemical Physics* [102], "Toward a Quantitative Understanding of the Reduction Pathways of a Salt Precursor in the Synthesis of Metal Nanocrystals" published in *Nano Letter* [70], "Decahedral Nanocrystals of Noble Metals: Synthesis, Characterization, and Applications" published in *Materials Today* [103], and "Icosahedral Nanocrystals of Noble Metals: Synthesis and Applications" published in *Nano Today* [26]. All of these publications were co-authored by me.

1.5 References

(1) Xia, Y.; Xiong, Y.; Lim, B.; Skrabalak, S. E. *Angew. Chem. Int. Ed.* **2009**, *48*, 60–103.

(2) Tao, A. R.; Habas, S.; Yang, P. *Small* **2008**, *4*, 310–325.

(3) Wu, J.; Yang, H. *Acc. Chem. Res.* **2013**, *46*, 1848–1857.

(4) Maier, S. A.; Brongersma, M. L.; Kik, P. G.; Meltzer, S.; Requicha, A. A. G.; Atwater, H. A. *Adv. Mater.* **2001**, *13*, 1501–1505.

(5) Kauranen, M.; Zayats, A. V. *Nat. Photonics* **2012**, *6*, 737–748.

(6) Koenderink, A. F.; Alù, A.; Polman, A. *Science* **2015**, *348*, 516–521.

(7) Jeong, S.; Woo, K.; Kim, D.; Lim, S.; Kim, J. S.; Shin, H.; Xia, Y.; Moon, J. *Adv. Funct. Mater.* **2008**, *18*, 679–686.

(8) Talapin, D. V.; Lee, J.-S.; Kovalenko, M. V.; Shevchenko, E. V. *Chem. Rev.* **2010**, *110*, 389–458.

(9) Linic, S.; Christopher, P.; Ingram, D. B. *Nat. Mater.* **2011**, *10*, 911–921.

(10) Alivisatos, P. *Nat. Biotechnol.* **2004**, *22*, 47–52.

(11) Zang, W.; Li, G.; Wang, L.; Zhang, X. *Catal. Sci. Technol.* **2015**, *5*, 2532–2553.

(12) Yu, W.; Porosoff, M. D.; Chen, J. G. *Chem. Rev.* **2012**, *112*, 5780–5817.

(13) Fan, Z.; Zhang, H. *Acc. Chem. Res.* **2016**, *49*, 2841–2850.

(14) Wu, B.; Zheng, N. *Nano Today* **2013**, *8*, 168–197.

(15) Rycenga, M.; Cobley, C. M.; Zeng, J.; Li, W.; Moran, C. H.; Zhang, Q.; Qin, D.; Xia, Y. *Chem. Rev.* **2011**, *111*, 3669–3712.

(16) Eustis, S.; El-Sayed, M. A. *Chem. Soc. Rev.* **2006**, *35*, 209–217.

(17) Chen, H.; Kou, X.; Yang, Z.; Ni, W.; Wang, J. *Langmuir* **2008**, *24*, 5233–5237.

(18) Verma, S. S.; Sekhon, J. S. *J. Opt.* **2012**, *41*, 89–93.

(19) Schlücker, S. *ChemPhysChem* **2009**, *10*, 1344–1354.

(20) Goy-López, S.; Juárez, J.; Cambón, A.; Botana, J.; Pereiro, M.; Baldomir, D.; Taboada, P.; Mosquera, V. *J. Mater. Chem.* **2010**, *20*, 6808–6814.

(21) Rycenga, M.; Camargo, P. H. C.; Li, W.; Moran, C. H.; Xia, Y. *J. Phys. Chem. Lett.* **2010**, *1*, 696–703.

(22) Rekha, C. R.; Nayar, V. U.; Gopchandran, K. G. J. *Sci. Adv. Mater. Devices* **2018**, *3*, 196–205.

(23) Tan, T.; Tian, C.; Ren, Z.; Yang, J.; Chen, Y.; Sun, L.; Li, Z.; Wu, A.; Yin, J.; Fu, H. *Phys. Chem. Chem. Phys.* **2013**, *15*, 21034-21042.

(24) Frank, A. J.; McEneny-King, A.; Cathcart, N.; Kitaev, V. *RSC Adv.* **2015**, *5*, 73919–73925.

(25) Tan, S.; Erol, M.; Sukhishvili, S.; Du, H. *Langmuir* **2008**, *24*, 4765–4771.

(26) Wang, H.; Zhou, S.; Gilroy, K. D.; Cai, Z.; Xia, Y. *Nano Today* **2017**, *15*, 121–144.

(27) Yu, X.; Pickup, P. G. *J. Power Sources* **2008**, *182*, 124–132.

(28) Choi, S.-I.; Herron, J. A.; Scaranto, J.; Huang, H.; Wang, Y.; Xia, X.; Lv, T.; Park, J.; Peng, H.-C.; Mavrikakis, M.; Xia, Y. *ChemCatChem* **2015**, *7*, 2077–2084.

(29) Wang, C.; Yin, H.; Chan, R.; Peng, S.; Dai, S.; Sun, S. *Chem. Mater.* **2009**, *21*, 433–435.

(30) Liu, S.; Tao, H.; Zeng, L.; Liu, Q.; Xu, Z.; Liu, Q.; Luo, J.-L. *J. Am. Chem. Soc.* **2017**, *139*, 2160–2163.

(31) Patil, A. B.; Patil, D. S.; Bhanage, B. M. *J. Mol. Catal. A Chem.* **2012**, *365*, 146–153.

(32) Long, R.; Mao, K.; Ye, X.; Yan, W.; Huang, Y.; Wang, J.; Fu, Y.; Wang, X.; Wu, X.; Xie, Y.; Xiong, Y. *J. Am. Chem. Soc.* **2013**, *135*, 3200–3207.

(33) Christopher, P.; Xin, H.; Linic, S. *Nat. Chem.* **2011**, *3*, 467–472.

(34) Christopher, P.; Linic, S. *ChemCatChem* **2010**, *2*, 78–83.

(35) Zheng, Y.; Zhong, X.; Li, Z.; Xia, Y. *Part. Part. Syst. Charact.* **2014**, *31*, 266–273.

(36) Wang, Y.; Xie, S.; Liu, J.; Park, J.; Huang, C. Z.; Xia, Y. *Nano Lett.* **2013**, *13*, 2276–2281.

(37) Sun, Y.; Xia, Y. *Science* **2002**, *298*, 2176–2179.

(38) Zhou, G.; Lu, M.; Yang, Z. *Langmuir* **2006**, *22*, 5900–5903.

(39) Siekkinen, A. R.; McLellan, J. M.; Chen, J.; Xia, Y. *Chem. Phys. Lett.* **2006**, *432*, 491–496.

(40) Zhang, Q.; Li, W.; Wen, L.-P.; Chen, J.; Xia, Y. *Chem. Eur. J.* **2010**, *16*, 10234–10239.

(41) Tao, A.; Sinsermsuksakul, P.; Yang, P. *Angew. Chem. Int. Ed.* **2006**, *45*, 4597–4601.

(42) Umar, A.; Lee, J.; Dey, J.; Choi, S.-M. *Chem. Mater.* **2016**, *28*, 4962–4970.

(43) Wu, H.-L.; Kuo, C.-H.; Huang, M. H. *Langmuir* **2010**, *26*, 12307–12313.

(44) Pietrobon, B.; Kitaev, V. *Chem. Mater.* **2008**, *20*, 5186–5190.

(45) Rodríguez-Fernández, J.; Novo, C.; Myroshnychenko, V.; Funston, A. M.; Sánchez-Iglesias, A.; Pastoriza-Santos, I.; Pérez-Juste, J.; García de Abajo, F. J.; Liz-Marzán, L. M.; Mulvaney, P. *J. Phys. Chem. C* **2009**, *113*, 18623–18631.

(46) Huang, H.; Wang, Y.; Ruditskiy, A.; Peng, H.-C.; Zhao, X.; Zhang, L.; Liu, J.; Ye, Z.; Xia, Y. *ACS Nano* **2014**, *8*, 7041–7050.

(47) Ma, Y.; Kuang, Q.; Jiang, Z.; Xie, Z.; Huang, R.; Zheng, L. *Angew. Chem. Int. Ed.* **2008**, *47*, 8901–8904.

(48) Tian, N.; Zhou, Z.-Y.; Sun, S.-G.; Ding, Y.; Wang, Z. L. *Science* **2007**, *316*, 732–735.

(49) Kim, D. Y.; Im, S. H.; Park, O. O. *Cryst. Growth Des.* **2010**, *10*, 3321–3323.

(50) Stamenkovic, V. R.; Fowler, B.; Mun, B. S.; Wang, G.; Ross, P. N.; Lucas, C. A.; Marković, N. M. *Science* **2007**, *315*, 493–497.

(51) Krause, M. M.; Kambhampati, P. *Phys. Chem. Chem. Phys.* **2015**, *17*, 18882–18894.

(52) Taguchi, T.; Isozaki, K.; Miki, K. *Adv. Mater.* **2012**, *24*, 6462–6467.

(53) Mout, R.; Moyano, D. F.; Rana, S.; Rotello, V. M. *Chem. Soc. Rev.* **2012**, *41*, 2539–2544.

(54) Merg, A. D.; Zhou, Y.; Smith, A. M.; Millstone, J. E.; Rosi, N. L. *ChemNanoMat* **2017**, *3*, 745–749.

(55) Niu, Z.; Li, Y. *Chem. Mater.* **2014**, *26*, 72–83.

(56) Ortiz, N.; Skrabalak, S. E. *Langmuir* **2014**, *30*, 6649–6659.

(57) Burrows, N. D.; Lin, W.; Hinman, J. G.; Dennison, J. M.; Vartanian, A. M.; Abadeer, N. S.; Grzincic, E. M.; Jacob, L. M.; Li, J.; Murphy, C. J. *Langmuir* **2016**, *32*, 9905–9921.

(58) Hu, P.; Chen, L.; Kang, X.; Chen, S. *Acc. Chem. Res.* **2016**, *49*, 2251–2260.

(59) Abdelhameed, M.; Martir, D. R.; Chen, S.; Xu, W. Z.; Oyeneye, O. O.; Chakrabarti, S.; Zysman-Colman, E.; Charpentier, P. A. *Sci. Rep.* **2018**, *8*, 3050.

(60) Gao, J.; Gu, H.; Xu, B. *Acc. Chem. Res.* **2009**, *42*, 1097–1107.

(61) Sekiguchi, S.; Niikura, K.; Matsuo, Y.; Ijiro, K. *Langmuir* **2012**, *28*, 5503–5507.

(62) Zhou, J.; Ralston, J.; Sedev, R.; Beattie, D. A. *J. Colloid Interface Sci.* **2009**, *331*, 251–262.

(63) Yang, X.; Yang, M.; Pang, B.; Vara, M.; Xia, Y. *Chem. Rev.* **2015**, *115*, 10410–10488.

(64) Oh, N.; Park, J.-H. *ACS Nano* **2014**, *8*, 6232–6241.

(65) Tan, S. J.; Jana, N. R.; Gao, S.; Patra, P. K.; Ying, J. Y. *Chem. Mater.* **2010**, *22*, 2239–2247.

(66) Pelaz, B.; del Pino, P.; Maffre, P.; Hartmann, R.; Gallego, M.; Rivera-Fernández, S.; de la Fuente, J. M.; Nienhaus, G. U.; Parak, W. J. *ACS Nano* **2015**, *9*, 6996–7008.

(67) Xia, X.; Yang, M.; Wang, Y.; Zheng, Y.; Li, Q.; Chen, J.; Xia, Y. *ACS Nano* **2012**, *6*, 512–522.

(68) Chen, M.; Wu, B.; Yang, J.; Zheng, N. *Adv. Mater.* **2012**, *24*, 862–879.

(69) Lohse, S. E.; Burrows, N. D.; Scarabelli, L.; Liz-Marzán, L. M.; Murphy, C. J. *Chem. Mater.* **2014**, *26*, 34–43.

(70) Yang, T.-H.; Peng, H.-C.; Zhou, S.; Lee, C.-T.; Bao, S.; Lee, Y.-H.; Wu, J.-M.; Xia, Y. *Nano Lett.* **2017**, *17*, 334–340.

(71) LaMer, V. K.; Dinegar, R. H. *J. Am. Chem. Soc.* **1950**, *72*, 4847–4854.

(72) Cacciuto, A.; Auer, S.; Frenkel, D. *Nature* **2004**, *428*, 404–406.

(73) Yao, T.; Liu, S.; Sun, Z.; Li, Y.; He, S.; Cheng, H.; Xie, Y.; Liu, Q.; Jiang, Y.; Wu, Z.; Pan, Z.; Yan, W.; Wei, S. *J. Am. Chem. Soc.* **2012**, *134*, 9410–9416.

(74) Thanh, N. T. K.; Maclean, N.; Mahiddine, S. *Chem. Rev.* **2014**, *114*, 7610–7630.

(75) Watzky, M. A.; Finke, R. G. *J. Am. Chem. Soc.* **1997**, *119*, 10382–10400.

(76) Watzky, M. A.; Finney, E. E.; Finke, R. G. *J. Am. Chem. Soc.* **2008**, *130*, 11959–11969.

(77) Liu, Q.; Gao, M.-R.; Liu, Y.; Okasinski, J. S.; Ren, Y.; Sun, Y. *Nano Lett.* **2016**, *16*, 715–720.

(78) van den Berg, R.; Elkjaer, C. F.; Gommes, C. J.; Chorkendorff, I.; Sehested, J.; de Jongh, P. E.; de Jong, K. P.; Helveg, S. *J. Am. Chem. Soc.* **2016**, *138*, 3433–3442.

(79) Wang, Y.; Peng, H.-C.; Liu, J.; Huang, C. Z.; Xia, Y. *Nano Lett.* **2015**, *15*, 1445–1450.

(80) Yang, T.-H.; Gilroy, K. D.; Xia, Y. *Chem. Sci.* **2017**, *8*, 6730–6749.

(81) Yang, T.-H.; Zhou, S.; Gilroy, K. D.; Figueroa-Cosme, L.; Lee, Y.-H.; Wu, J.-M.; Xia, Y. *Proc. Natl. Acad. Sci. U. S. A.* **2017**, *114*, 13619–13624.

(82) Dong, H.; Chen, Y.-C.; Feldmann, C. *Green Chem.* **2015**, *17*, 4107–4132.

(83) Wen, J.; Li, J.; Liu, S.; Chen, Q. *Colloids Surfaces A Physicochem. Eng. Asp.* **2011**, *373*, 29–35.

(84) Mourdikoudis, S.; Liz-Marzán, L. M. *Chem. Mater.* **2013**, *25*, 1465–1476.

(85) Li, S.; Liu, P.; Wang, Q.; Chen, X.; Xiao, J. *J. Wuhan Univ. Technol. Sci. Ed.* **2013**, *28*, 1246–1250.

(86) Sun, Y.; Yin, Y.; Mayers, B. T.; Herricks, T.; Xia, Y. *Chem. Mater.* **2002**, *14*, 4736–4745.

(87) Wiley, B.J.; Im, S.H.; Li, Z.-Y.; McLellan, J.; Siekkinen, A.; Xia, Y. *J. Phys. Chem. B* **2006**, *110*, 15666–15675

(88) Wiley, B. J.; Chen, Y.; McLellan, J. M.; Xiong, Y.; Li, Z.-Y.; Ginger, D.; Xia, Y. *Nano Lett.* **2007**, *7*, 1032–1036.

(89) Ruditskiy, A.; Xia, Y. *J. Am. Chem. Soc.* **2016**, *138*, 3161–3167.

(90) Yuan, Q.; Wang, X. *Nanoscale* **2010**, *2*, 2328–2335.

(91) Xia, Y.; Gilroy, K. D.; Peng, H.-C.; Xia, X. *Angew. Chem. Int. Ed.* **2017**, *56*, 60–95.

(92) Xia, X.; Zeng, J.; Zhang, Q.; Moran, C. H.; Xia, Y. *J. Phys. Chem. C* **2012**, *116*, 21647–21656.

(93) Zeng, J.; Zheng, Y.; Rycenga, M.; Tao, J.; Li, Z.-Y.; Zhang, Q.; Zhu, Y.; Xia, Y. *J. Am. Chem. Soc.* **2010**, *132*, 8552–8553.

(94) Kong, W.; Sun, T.; Chen, B.; Chen, X.; Ai, F.; Zhu, X.; Li, M.; Zhang, W.; Zhu, G.; Wang, F. *Inorg. Chem.* **2017**, *56*, 872–877.

(95) Dewi, M. R.; Laufersky, G.; Nann, T. *RSC Adv.* **2014**, *4*, 34217–34220.

(96) Crespo-Quesada, M.; Andanson, J.-M.; Yarulin, A.; Lim, B.; Xia, Y.; Kiwi-Minsker, L. *Langmuir* **2011**, *27*, 7909–7916.

(97) Clark, T.; Ruiz, J.D.; Fan, H.; Brinker, C.J.; Swanson, B.I.; Parikh A.N. *Chem. Mater.* **2000**, *12*, 3879–3884

(98) Elliott, E. W.; Glover, R. D.; Hutchison, J. E. *ACS Nano* **2015**, *9*, 3050–3059.

(99) Aliaga, C.; Park, J. Y.; Yamada, Y.; Lee, H. S.; Tsung, C.-K.; Yang, P.; Somorjai, G. A. *J. Phys. Chem. C* **2009**, *113*, 6150–6155.

(100) Zhou, S.; Li, J.; Gilroy, K. D.; Tao, J.; Zhu, C.; Yang, X.; Sun, X.; Xia, Y. *ACS Nano* **2016**, *10*, 9861–9870.

(101) Zhou, S.; Mesina, D. S.; Organt, M. A.; Yang, T.-H.; Yang, X.; Huo, D.; Zhao, M.; Xia, Y. *J. Mater. Chem. C* **2018**, *6*, 1384–1392.

(102) Zhou, S.; Yang, T.H.; Zhao, M.; Xia, Y. *Chin. J. Chem. Phys.* **2018**, accepted.

(103) Zhou, S.; Zhao, M.; Yang, T.-H.; Xia, Y. *Mater. Today* **2018**, in press.

CHAPTER 2

FACILE SYNTHESIS OF SILVER NANOCUBES WITH SHARP CORNERS AND EDGES IN AN AQUEOUS SYSTEM

2.1 Introduction

Silver (Ag) nanocrystals have found widespread use in a range of applications involving localized surface plasmon resonance (LSPR), surface-enhanced Raman scattering (SERS), metal-enhanced fluorescence, and catalysis [1,2]. For most of these applications, it is critical to have a tight control over the shape taken by nanocrystals in order to maximum their performance. Over the past decade, Ag nanocrystals have been successfully synthesized with a large number of diversified shapes, including spheres [3], cubes [2,4–8], bars [9], tetrahedra [10], octahedra [11], decahedra [12], right bipyramids [13], and pentagonal rods/wires [14]. Among these examples, nanocubes are of great interest because they can serve as sacrificial templates to fabricate Au-based nanocages with tunable LSPR peaks in the near-infrared region [15,16], and as outstanding substrates for optical sensing and SERS detection [17]. Among all synthetic methods that have been developed for the synthesis of Ag nanocubes, polyol reduction is probably the most widely used and most successful approach. The polyol process uses alcohols with more than one hydroxyl groups as both the solvent and reductant (or a precursor to the reductant). The most extensively used polyols include ethylene glycol (EG) and diethylene glycol (DEG). After more than one decade of refinement, polyol reduction can now be applied to synthesize Ag nanocubes with edge lengths over a very broad range of 13-400 nm [2,4–8].

Despite its great success in the synthesis of Ag nanocrystals, polyol reduction also has a few drawbacks. For example, the synthesis is very sensitive to impurities (such as trace amounts of Cl^- and Fe^{2+}/Fe^{3+} ions), water content, and the amount of O_2, making the synthesis sometimes difficult to duplicate. At the same time, the Ag nanocubes synthesized using the polyol process tend to be rounded at corners and edges [2,15], which can be attributed to three major reasons: *i*) the relatively high diffusivity of Ag atoms at an elevated temperature (typically, in the range of 140-160 ºC) needed for activating the reduction power of a polyol; *ii*) the enhanced oxidative etching of corners and edges at an elevated temperature, and *iii*) the inadequacy of poly(vinylpyrrolidone) (PVP) in passivating and protecting the {100} side faces as a result of their long chains. In addition, the use of an organic solvent and the requirement of a relatively high temperature also make the protocol environmentally less friendly and economically unattractive. These drawbacks could be eliminated by developing a water-based route. In this case, an additional reducing agent has to be introduced because H_2O lacks the power to reduce Ag^+ ions into the elemental form. In principle, an aqueous synthesis can be carried out at a much lower temperature than the polyol process, facilitating the formation and preservation of the sharp edges and corners on Ag nanocubes. The exclusion of polyols also solves the irreproducibility problem associated with trace impurities [18]. Furthermore, a water-based synthesis is anticipated to be greener and environmentally more friendly, offering more flexibility and convenience for execution (*e.g.*, outside the fume hood).

Although aqueous protocols have been explored by a number of groups for the seed-mediated growth of Ag nanocrystals [11,19-24], there are very few reports on the synthesis of Ag single-crystal nanocubes using a one-pot, aqueous system. The conditions for seed

formation and the following growth step are often very different, making it more challenging to achieve precise control in one-pot synthesis than in seed-mediated growth. After extensive literature search, I was only able to find one report on the one-pot, aqueous method, in which Ag nanocubes with edge lengths of 55–72 nm were prepared [25,26]. This method, however, involved the use of hydrothermal conditions at 120 ^{o}C, and it is still a challenge to monitor and analyze the growth of nanocrystals, especially in the early stages of a synthesis, in such a closed system. In addition, this method used a hazardous precursor based on $Ag(NH_3)_2OH$, an unstable compound that might decompose to generate explosive silver azide when handled improperly [27].

Herein, I reported a facile method for the synthesis of Ag nanocubes in an aqueous system. The Ag nanocubes could be made with sharp corners and edges by employing Cl^- ions as a specific capping agent for the {100} facets and conducting the synthesis at a relatively low temperature of 60 ^{o}C. By mixing CF_3COOAg with cetyltrimethylammonium chloride (CTAC) in an aqueous solution, AgCl nanoscale octahedra were formed in the early stage, which then served as a source to elemental Ag. In the presence of both room light and a reducing agent such as ascorbic acid (AA), Ag_n nuclei were generated both on the surface and in the interior of the AgCl octahedra, followed by their evolution into single-crystal seeds and finally Ag nanocubes. The presence of $FeCl_3$ as an oxidative etchant to remove the twinned seeds further facilitated the formation of Ag nanocubes in a high morphology yield. The as-synthesized Ag nanocubes showed strong SERS activity due to the preserved sharp corners and edges.

2.2 Results and Discussion

2.2.1 Synthesis of Ag Nanocubes

Figure 2.1a shows the transmission electron microscopy (TEM) image of a sample obtained at t = 6 h into the synthesis. The nanocubes had an average edge length of 93±4 nm. It is worth noting that the corners and edges of these nanocubes were sharper than their counterparts prepared at a higher temperature (typically, 160 ^{o}C) through polyol reduction. Figure 2.1, b and c, shows scanning electron microscopy (SEM) images of the same sample at two different magnifications. For a standard synthesis, the typical morphology yield of Ag nanocubes was approximately 70%, with the presence of some right bipyramids, truncated right bipyramids, and nanorods as the side products.

The two-dimensional array of nanocubes showed an inter-particle separation of about 6.4 nm (Figure 2.2), twice that of the thickness of a CTAC bilayer (~3 nm). This result indicates that CTAC formed a bilayer structure on the side faces of each Ag nanocube in the aqueous solution, making the nanocubes hydrophilic and thus well-dispersed in water.

The red curve in Figure 2.1d shows the UV-vis spectrum recorded from an aqueous suspension of the as-obtained nanocubes. The four well-defined LSPR peaks are consistent with the previous experimental and calculation results for Ag nanocubes with a similar size [28,29]. The black curve shows the extinction spectrum obtained using discrete dipole approximation (DDA) calculation for a Ag nanocube with 2.3 nm truncation at the corners and 0.6 nm truncation at the edges, which is in good agreement with the experimental data.

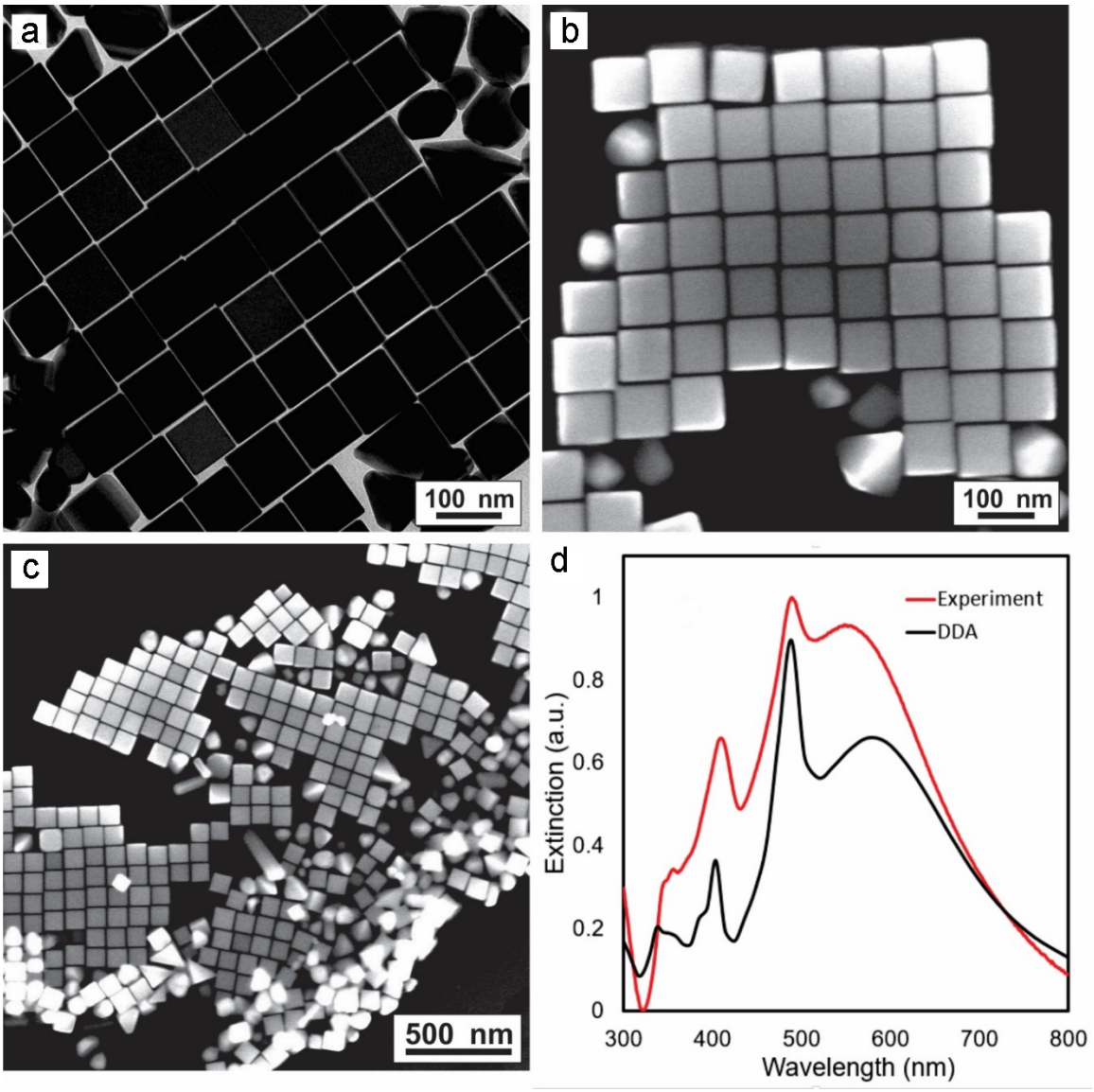

Figure 2.1. (a) TEM and (b) SEM images of the as-synthesized Ag nanocubes with an average edge length of 93±4 nm. (c) A low-magnification SEM image of the Ag nanocubes, showing the co-existence of Ag nanocrystals with other shapes. (d) UV-vis spectrum recorded from an aqueous suspension of the sample shown in (c) and the DDA calculation result for a 93-nm cube with 2.3 nm truncation at the corners and 0.6 nm truncation at the edges. (Reprinted with permission from [42]. Copyright 2016 American Chemical Society.)

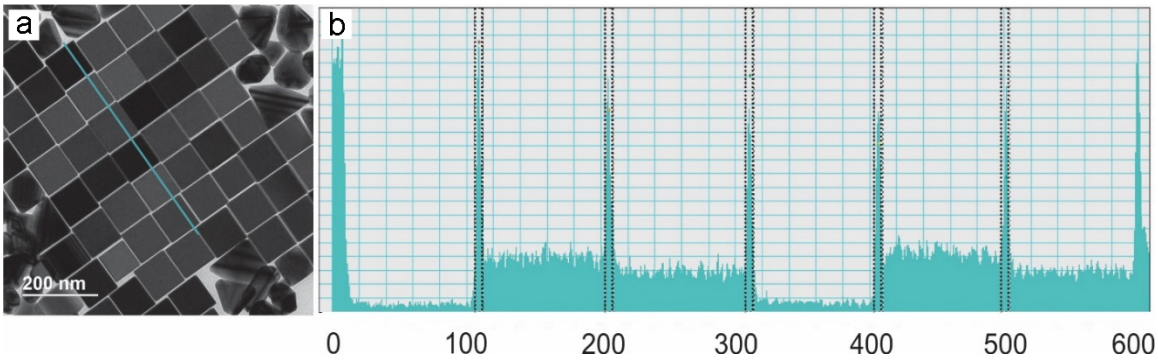

Figure 2.2. (a) Reproduction of the TEM image in Figure 2.1a. (b) A plot of the transmitted electron intensity along the blue line shown in (b). The dashed areas had an average width of 6.4 nm, corresponding to a thickness of two CTAC bilayers. (Reprinted with permission from [42]. Copyright 2016 American Chemical Society.)

2.2.2 Growth Mechanism

In an effort to decipher the growth mechanism, I examined the products obtained at different stages of a standard synthesis using both SEM (Figure 2.3) and TEM (Figure 2.4). When CF_3COOAg was added into an aqueous CTAC solution, AgCl nanoscale octahedra were formed immediately within the first several minutes. As shown in Figure 2.3a, well-defined AgCl octahedra with an average edge length of about 150 nm were formed at t = 5 min into the synthesis. These octahedra were highly sensitive to the electron beam, suggesting a composition of AgCl rather than Ag [30]. In fact, under the irradiation of electron beam, Ag nanocrystals (the bright dots) were formed at the corner and edge sites of a AgCl octahedron owing to the reduction of AgCl by the electron beam. This observation suggests the possible existence of Ag_n nuclei (*e.g.*, Ag_2, Ag_3^+, and Ag_4 among others) in the AgCl octahedra prior to SEM characterization.

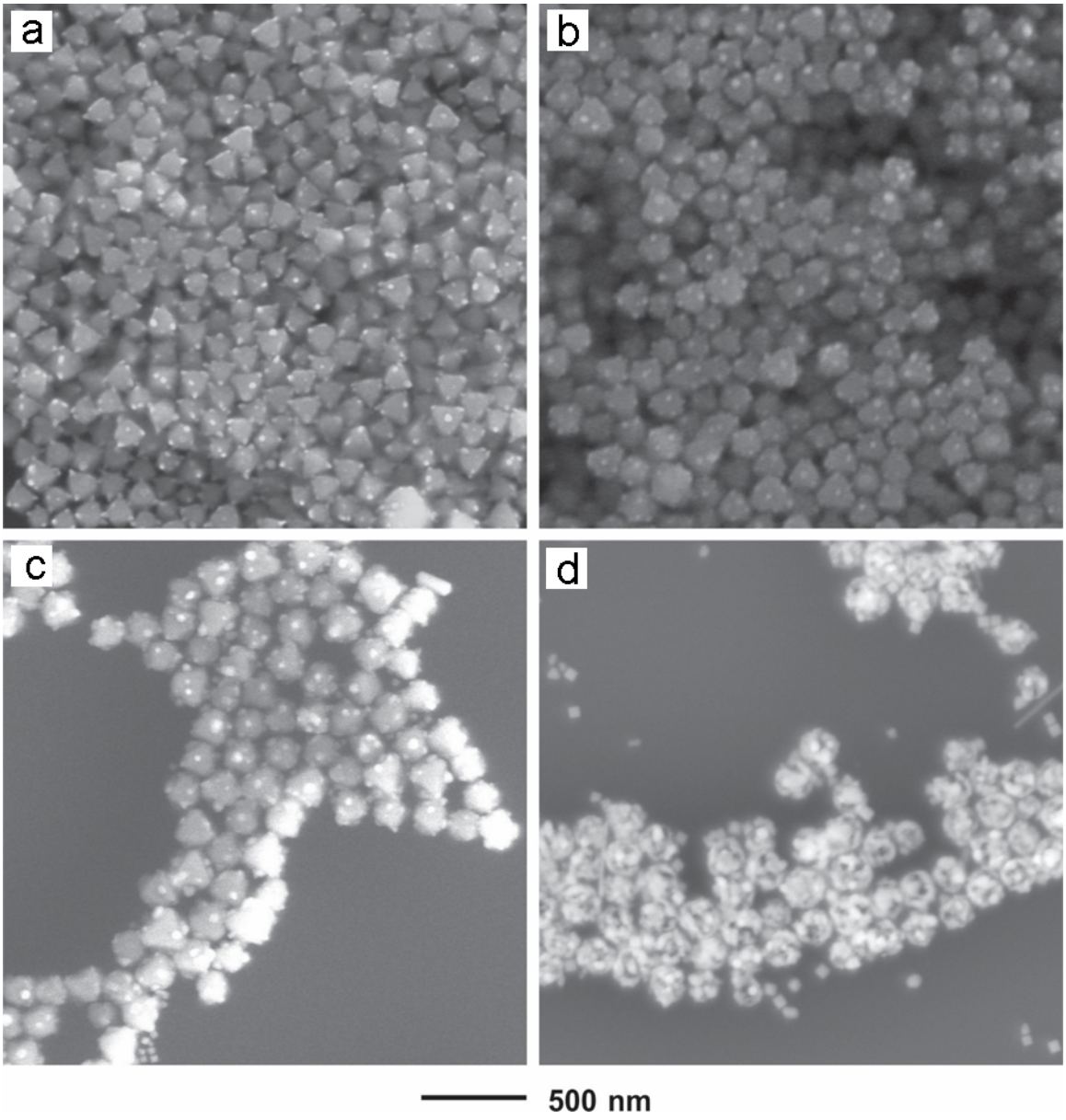

Figure 2.3. SEM images of samples obtained at different stages of a standard synthesis: (a) 5, (b) 30, (c) 90 and (d) 120 min. The octahedral nanocrystals shown in (a-d) were made of AgCl while the small, bright dots can be assigned to Ag nanocrystals formed from the decomposition of AgCl upon exposure to electron beam (typically within a few seconds). Silver nanocrystals with a cubic shape could be easily identified in (c-d). (Reprinted with permission from [42]. Copyright 2016 American Chemical Society.)

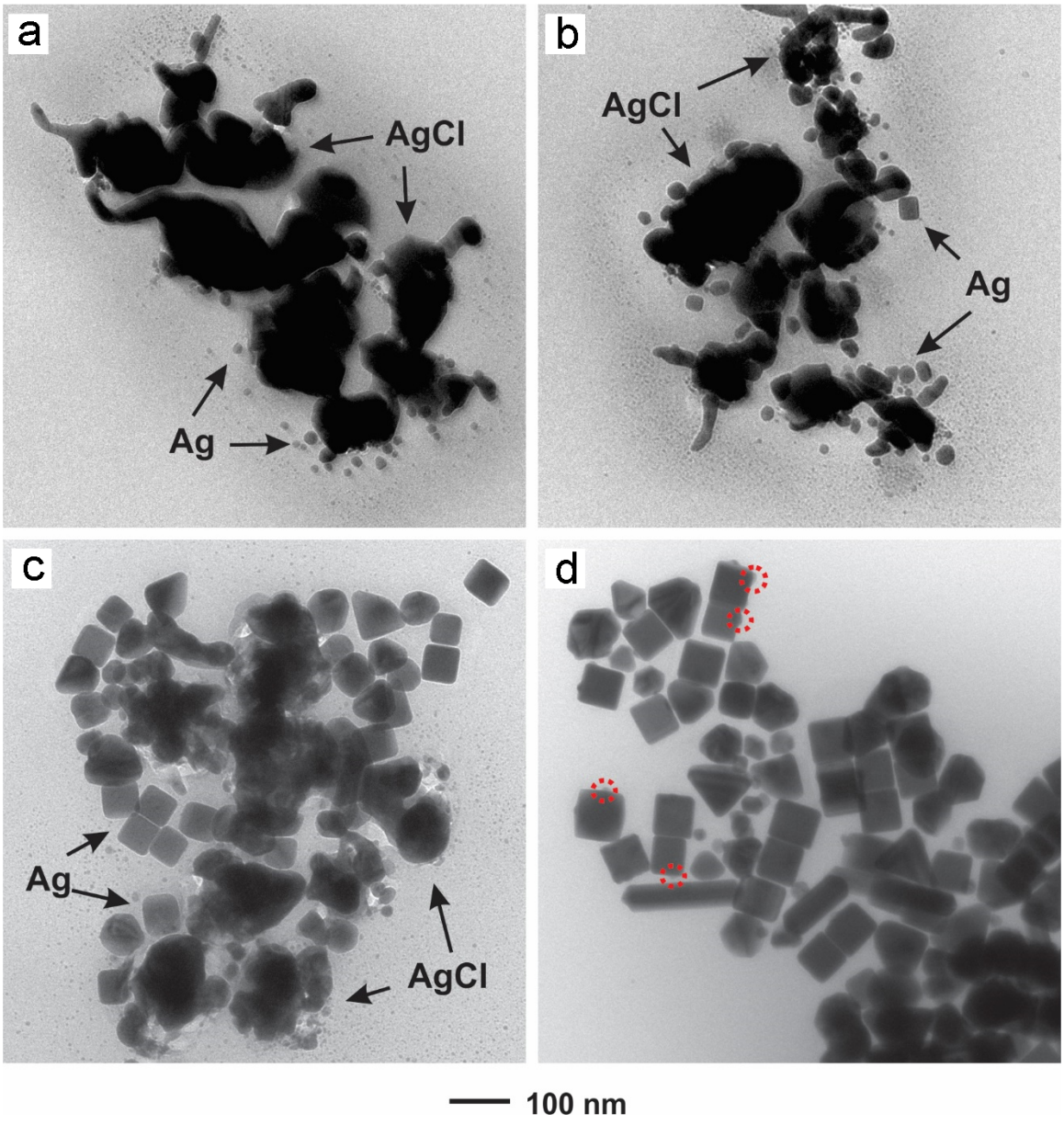

Figure 2.4. TEM images of samples obtained at different stages of a standard synthesis: (a) 30, (b) 90, (c) 120 and (d) 150 min. The big irregular AgCl particles and Ag nanocrystals were indicated by arrows in (a-c). A very small amount of AgCl can still be observed on the surface of some Ag nanocubes in (d), as marked by red dotted circles. (Reprinted with permission from [42]. Copyright 2016 American Chemical Society.)

A closer examination shows that the corners of the AgCl octahedra obtained at t = 30 min (Figure 2.3b) were rounded. Further extension of the reaction time to t = 90 min and 120 min led to more significant destruction to the structure, as shown in Figure 2.3, c and

d. These results indicate that AgCl was gradually reduced and dissolved as the synthesis was continued. The TEM images in Figure 2.4 clearly show the co-existence of AgCl and Ag nanocrystals throughout the synthesis. At t = 30 min, the number of Ag nanocrystals was relatively small and they were mainly spherical in shape. As the reaction proceeded, the number of AgCl particles would drop while more and larger Ag nanocubes could be identified. This observation implies that most of the Ag nanocubes might be embedded in the interior of the AgCl nanocrystals and were later exposed due to the reduction and dissolution of AgCl. It is worth pointing out that the AgCl nanocrystals could be readily dissolved by introducing additional CTAC solution. This offers us the opportunity to attain Ag nanocubes with average edge lengths of 36±3 nm and 56±5 nm (Figure 2.5), respectively, for the two samples obtained at t = 90 min at t = 120 min. At t = 150 min into the synthesis, I could still observe a small amount of AgCl mixed in the products (Figure 2.4d). The AgCl component completely disappeared after 3 h, as demonstrated by the sample shown in Figure 2.1. Taken together, it can be concluded that both Ag_n nuclei and AgCl nanocrystals were formed in the very early stage of a synthesis and the AgCl component then served as a precursor to elemental Ag during the evolution of the Ag_n nuclei into single-crystal seeds and then nanocubes.

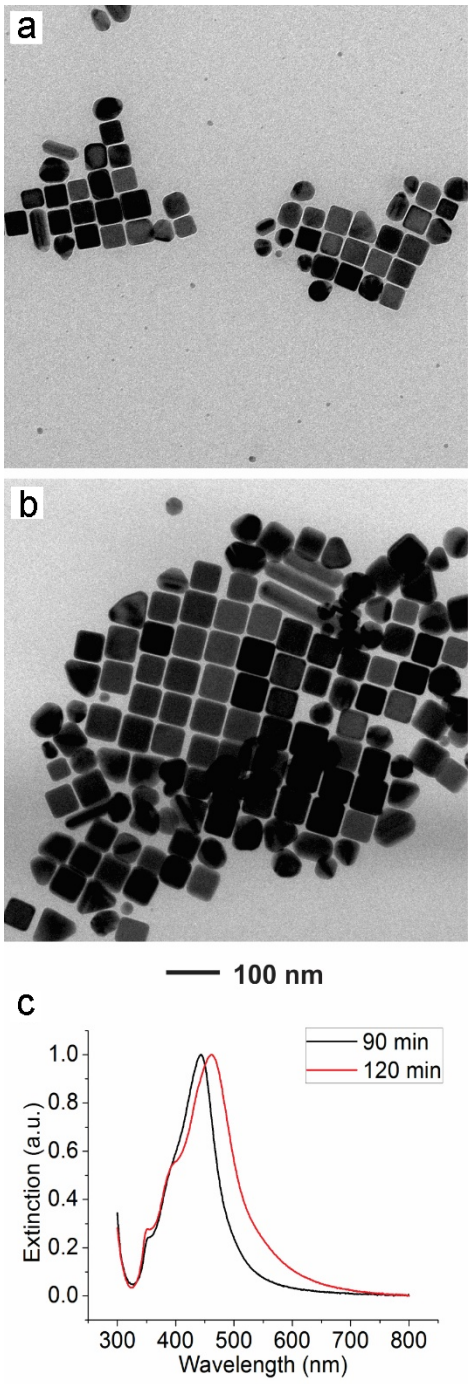

Figure 2.5. (a, b) TEM images of Ag nanocubes obtained at (a) 90 and (b) 120 min, respectively, in a standard synthesis. The samples were stirred with 1 mL of 200 mM CTAC solution at room temperature for 10 min to remove residual AgCl particles prior to collection. The Ag nanocubes presented had an average edge length of (a) 36±3 and (b) 56±5 nm, respectively. (c) UV spectra recorded from aqueous suspensions of the Ag nanocubes. (Reprinted with permission from [42]. Copyright 2016 American Chemical Society.)

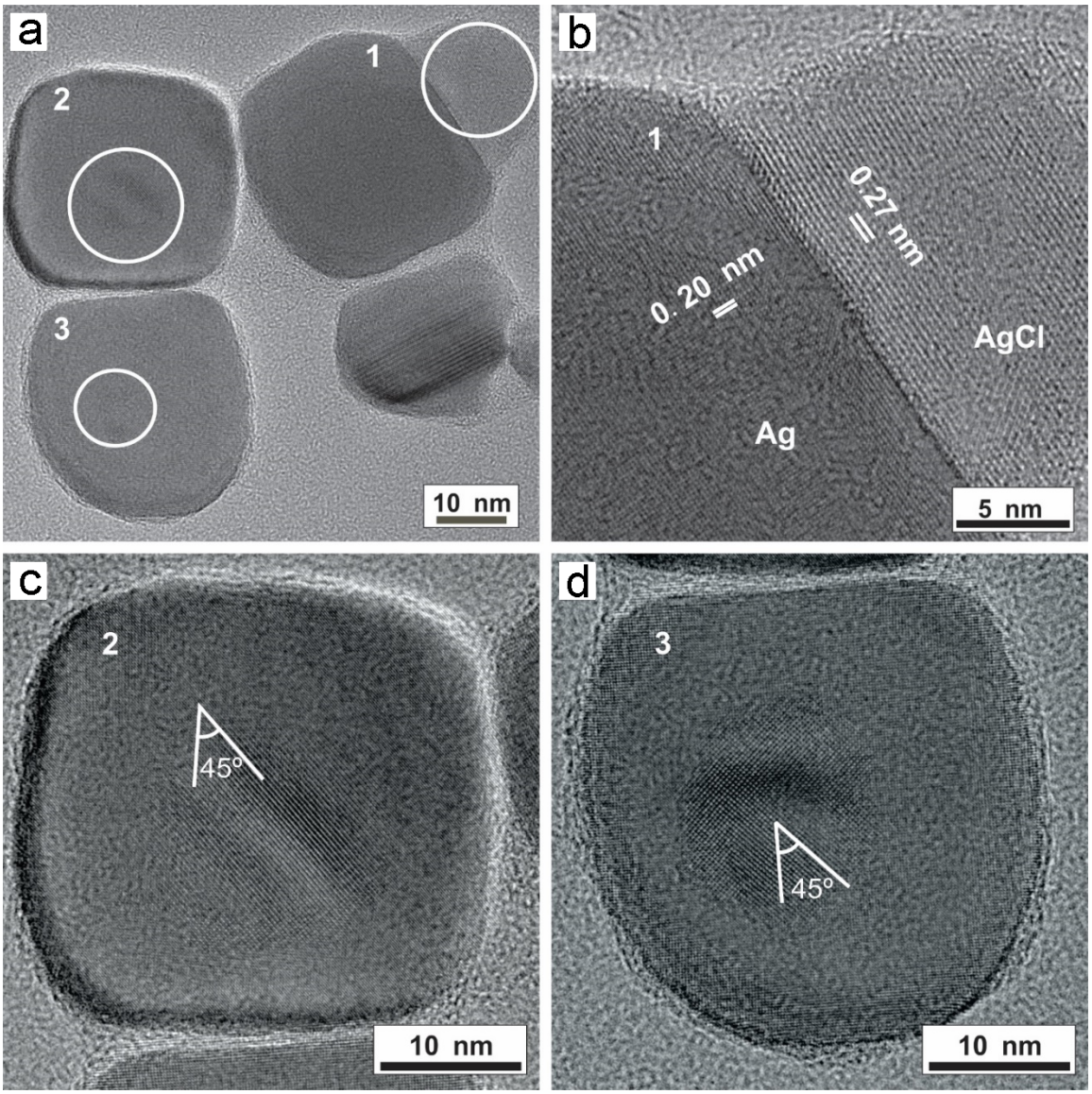

Figure 2.6. (a) HRTEM image of Ag nanocubes obtained at t = 60 min. The circles indicate the presence of AgCl on three Ag nanocubes (labelled with 1, 2, and 3). (b) Magnified HRTEM image taken from the interface region between Ag nanocube 1 and AgCl components. (c, d) HRTEM image of Ag nanocubes 2 and 3 with AgCl components on top of their {100} facets. There was a 45º angle between the <200> axes of Ag and AgCl lattices. (Reprinted with permission from [42]. Copyright 2016 American Chemical Society.)

The results of this time-dependent experiment indicate that the Ag nanocrystals might grow directly on the surface or inside the preformed AgCl octahedra at the expense of AgCl through continuous reduction. To validate this mechanism, I used high-resolution TEM to

characterize the samples obtained in the early stage of a synthesis. At t = 60 min, more than half of the particles were found to contain two components with different contrasts (Figure 2.6a). Under the electron beam, the lighter component gradually melted and became part of the darker component. The *d*-spacing values of these two components were also different: 0.20 nm and 0.27 nm for the darker and lighter components, respectively, which could be assigned to the *d*-spacing of {200} facets for face-centered-cubic (*fcc*) Ag and cubic AgCl phase (Figure 2.6b), respectively [31]. The HRTEM images in Figure 2.6, c and d, indicate that there was a rotation of 45º between the two <200> axes of these two single-crystal components. This observation can be understood by considering the fact that the length of face diagonal of the Ag unit cell is almost the same as the edge length of the AgCl unit cell. This correlation further explains why these two crystal phases adhere to each other despite their large difference in lattice constant. The epitaxial relationship between the Ag and AgCl components suggests that the Ag nanocube was formed by developing the Ag nucleus directly attached to the preformed AgCl nanocrystal.

It should be emphasized that all my experiments were carried out under the room light from fluorescent lamps. The solution typically showed a yellowish green color after 6 h into the standard synthesis (Figure 2.7, the left vial). When the glass vial was wrapped with aluminum foil throughout the synthesis, the solution took a pale white color after heating at 60 ºC for 6 h (Figure 2.7, the right vial). The products mainly contained AgCl particles, indicating the lack of reduction from AgCl to Ag. This observation indicates the important role of photolysis in the formation of Ag nuclei and photo-reduction in the following step of growth.

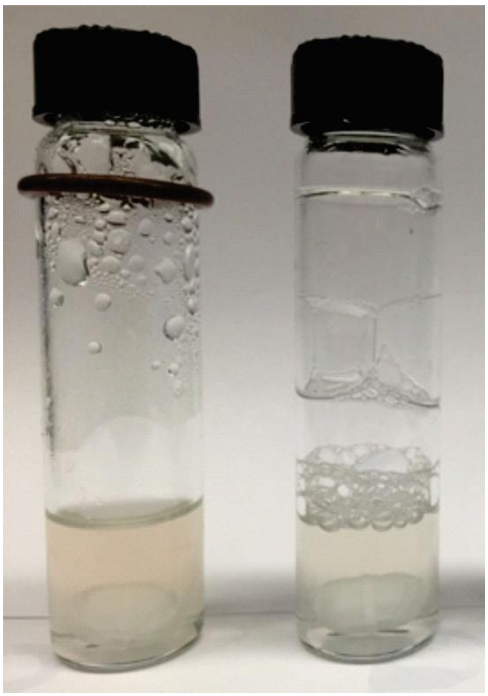

Figure 2.7. Photograph showing a comparison of two different reaction solutions: (left) a standard synthesis under room light (yellowish green) and (right) a synthesis under dark (pale white). (Reprinted with permission from [42]. Copyright 2016 American Chemical Society.)

Oxidative etching is important for the growth of metal nanocrystals with a specific internal structure because it can selectively dissolve the kinetically less favorable twinned seeds [32]. Iron(III) chloride has been used as an oxidative etchant for the removal of twinned seeds and particles to facilitate the formation of single-crystal Ag nanocubes [33]. In my synthesis, without the introduction of $FeCl_3$, the percent of twinned particles in the final products became much higher (Figure 2.8a). When the concentration of $FeCl_3$ was raised to 17.16 μM (four times as high as the concentration of $FeCl_3$ used in the standard synthesis), the Ag nanocubes started to show severe truncations at the corners and edges due to the enhancement in oxidative etching (Figure 2.8b) [34,35]. Taken together, a proper concentration of etchant should be used for eliminating the twinned seeds and particles during the synthesis and at the same time, keeping the corners and edges sharp.

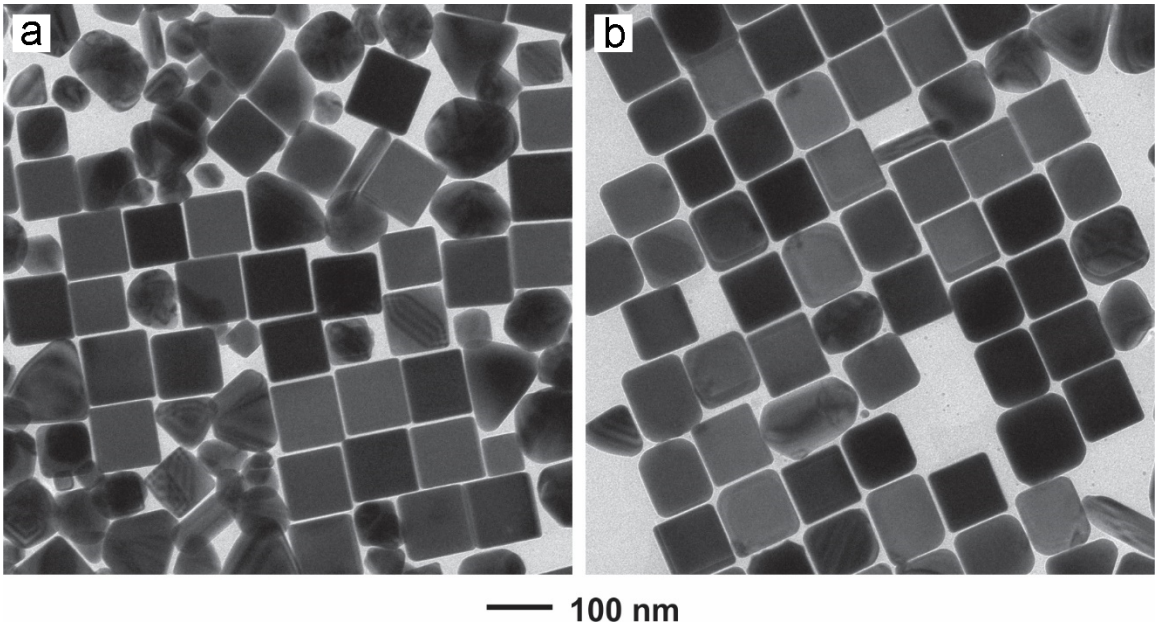

Figure 2.8. TEM images of samples obtained under the conditions of a standard synthesis, except for the variation of $FeCl_3$ amounts: (a) 0 and (b) 80 μl of 17.16 μM $FeCl_3$. (Reprinted with permission from [42]. Copyright 2016 American Chemical Society.)

In summary, the mechanism underlying the nucleation and growth of Ag nanocubes in this aqueous system shares a great deal in common with the photographic process [36]. The nucleation of Ag_n nuclei is similar to the formation of latent image centers and the further growth of these nuclei can be referred to as the development of the latent image centers. To be more specific, the synthesis starts with the formation of AgCl octahedra and small Ag_n nuclei (Figure 2.9). The nuclei could have been formed in the early stage of a synthesis due to the presence of room light and reducing agent, or even inherited from the Ag precursor [37,38]. Both light and reducing agent are well-known to have the ability to generate stable Ag_2 and Ag_4 on AgCl particles. The Ag_2 cluster is believed to be the smallest stable nuclei while the Ag_4 is the smallest active cluster to initiate the development of Ag nanocrystals [37]. Similar to the formation of latent image centers, these Ag_n nuclei can be formed both on the surface and in the interior of a AgCl nanocrystal through

photolysis by the room light and reduction by the ascorbic acid, preferably at the kink or defect sites of the AgCl nanocrystal. Compare to the Ag_n nuclei positioned on the surface, the internal nuclei would be ineffective in promoting growth until the outer layer of AgCl has been dissolved away or reduced [36]. This means the Ag_n nuclei on the surface should grow first with the reduction and dissolution of AgCl (Figure 2.9, step-i) and only after the solid structure of AgCl octahedra is shattered, the internal nuclei would be exposed to the reducing agent and start to grow (Figure 2.9, step-ii).

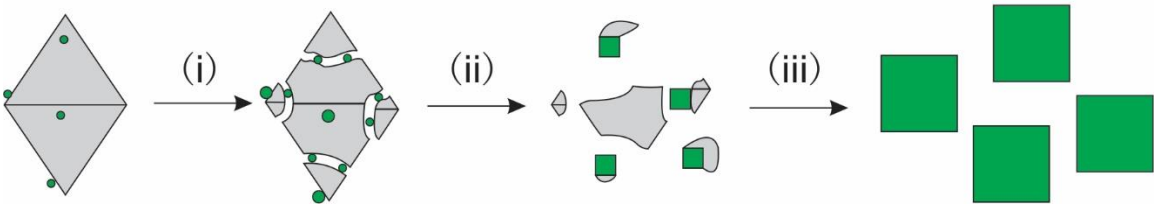

Figure 2.9. Schematic of the mechanism involved in the formation of Ag nanocubes in an aqueous system. The AgCl and Ag are shown in grey and green colors, respectively. The synthesis can be divided into three stages: (i) Formation of AgCl octahedra upon mixing CTAC with CF_3COOAg. Small Ag_n nuclei are formed both on the surface and in the interior of AgCl octahedra as a result of exposure to light and/or reducing agent. When the Ag_n nuclei on the surface start to grow, the underlying AgCl octahedron will start to disappear due to reduction and dissolution. (ii) Exposure of the internal Ag_n nuclei to the reducing environment. All the Ag_n nuclei quickly grow in size at the expense of remaining AgCl. In this stage, one can observe Ag nanocubes epitaxially connected with AgCl. (iii) Formation of Ag nanocubes with sharp corners and edges. (Reprinted with permission from [42]. Copyright 2016 American Chemical Society.)

Two types of Ag sources could be involved in the growth (development) of Ag_n nuclei: *i*) Ag^+ ions in the lattice of AgCl particles and *ii*) Ag^+ ions released due to the dissolution of AgCl [36]. The process involves the reduction of the first Ag source is known as chemical or direct development in photography, and these Ag^+ ions are reduced through a solid-state reaction at the Ag/AgCl interface. The Ag^+ ions include those already existing or those that will diffuse to the interface through the solid AgCl particles. The supply of

Ag^+ ions from this source is not adequate for attaining a cubic shape, and thus typically leads to the formation of spherical nanocrystals with a size of less than 20 nm and eventually Ag filaments with a diameter of 20 nm, as reported in early studies [37]. The reduction process involving the dissociated Ag^+ ions is known as solution physical development, which is believed to occur at the Ag/liquid interface. Considering the small surface area of Ag_n nuclei, this reduction process is very slow at the early stages, but becomes dominant as the size of the Ag nanocrystals increased [36]. Since this reduction occurs at the Ag/liquid interface, the shape of resultant Ag nanocrystals can be altered in the presence of a capping agent. In my system, the growth of Ag_n nuclei mainly started from the direct development, which is confirmed by the lack of a cubic shape for the small Ag nanocrystals in early stages of a synthesis. Once the surface area of the Ag nanocrystals had been enlarged to a certain level, the contribution from the solution physical process would become significant. As such, the Ag nanocrystals would keep growing by self-catalyzing the reduction of free Ag^+ in the solution with the {100} facets being capped by Cl^- ions. This growth leads to the formation of Ag nanocubes in the final product (Figure 2.9, step-iii). The use of $FeCl_3$ at an appropriate concentration is critical for selectively etching away twinned seeds and particles without influencing the sharp corners and edges. Oswald ripening might also happen throughout the synthesis, which could explain why I did not observe small nanocubes in the final products. This mechanism is completely different from what is involved in the polyol synthesis of Ag nanocubes. In a typical polyol process involving the introduction of NaCl or HCl to mediate the reduction kinetics, AgCl was precipitated out in the initial stage but quickly reduced to elemental Ag to facilitate the formation of seeds and then nanocubes [6]. In the aqueous system, the reduction of

AgCl and the evolution of Ag nanocubes seem to occur simultaneously throughout the synthesis.

Compared to the conventional polyol synthesis of Ag nanocubes, this protocol uses Cl^- ions instead of PVP as a capping agent for the Ag{100} facets. Chloride ion has a much smaller size than the long polymer chain of PVP, thus it can better cover the sides faces to make the edges and corners sharp. The use of a relatively low reaction temperature in the aqueous system also ensures that the diffusion of Ag atoms is slowed down and the oxidative etching on edges and corners are weakened. All these factors contribute to the formation of Ag nanocubes with sharp corners and edges.

2.2.3 Influence of Reduction Kinetics

The synthesis involves both the reduction of Ag^+ ions in the solid state and the reduction of dissociated Ag^+ ions on the surface of Ag_n nuclei. As such, any factor capable of altering the reduction rate (including, for example, temperature, pH value, and the nature of precursor/reducing agent) would affect the nucleation and growth of Ag nanocubes. I first investigated the influence of temperature on the products. At room temperature, I only observed AgCl nanocrystals. When the temperature was increased to 50 °C, the products were dominated by Ag nanocubes with an average edge length of 57±3 nm (Figure 2.10a), much smaller than the nanocubes obtained using the standard protocol at 60 °C (Figure 2.1a). There were also many smaller Ag nanocrystals and AgCl particles in the products. These results indicate that the weakened reducing power at a lower temperature was unable to reduce all the AgCl within 6 hours. When the temperature was increased to 70 °C, the Ag nanocubes had an average edge length of 86±4 nm (Figure 2.10b), slightly smaller than

what was obtained at 60 °C. The higher temperature triggered a faster reduction rate, leading to the formation of more Ag_n nuclei in the nucleation stage and thus smaller size for the final products. Nevertheless, the increase in reaction temperature did not noticeably improve the percentage yield of nanocubes (still around 70%). The as-obtained Ag nanocubes also became more truncated when the reaction temperature was increased. Taken together, a reaction temperature around 60 °C seems to be optimal for the formation of Ag nanocubes with sharp corners and edges.

The reducing power of AA is known to increase with increasing the pH value [39]. As such, I carried out a set of experiments to figure out the relationship between the final products and the pH value. By introducing HCl or NaOH, I could easily fine tune the pH value and thereby the reducing power of AA. The pH value of a standard synthesis was around 3.1 throughout the reaction. Figure 2.10, c and d, show TEM images of the products obtained at other pH values. When the pH was set to 2.7, the products were dominated by truncated right bipyramids. This can be ascribed to the reduced reduction rate, which favors the formation of twinned seeds. When the pH was increased to 7.4, the final products mainly contained irregular nanocrystals with a much smaller size than those obtained using a standard protocol. The faster reduction rate during the nucleation stage increased the number of seeds, leading to a smaller particle size when the amount of Ag precursor was fixed.

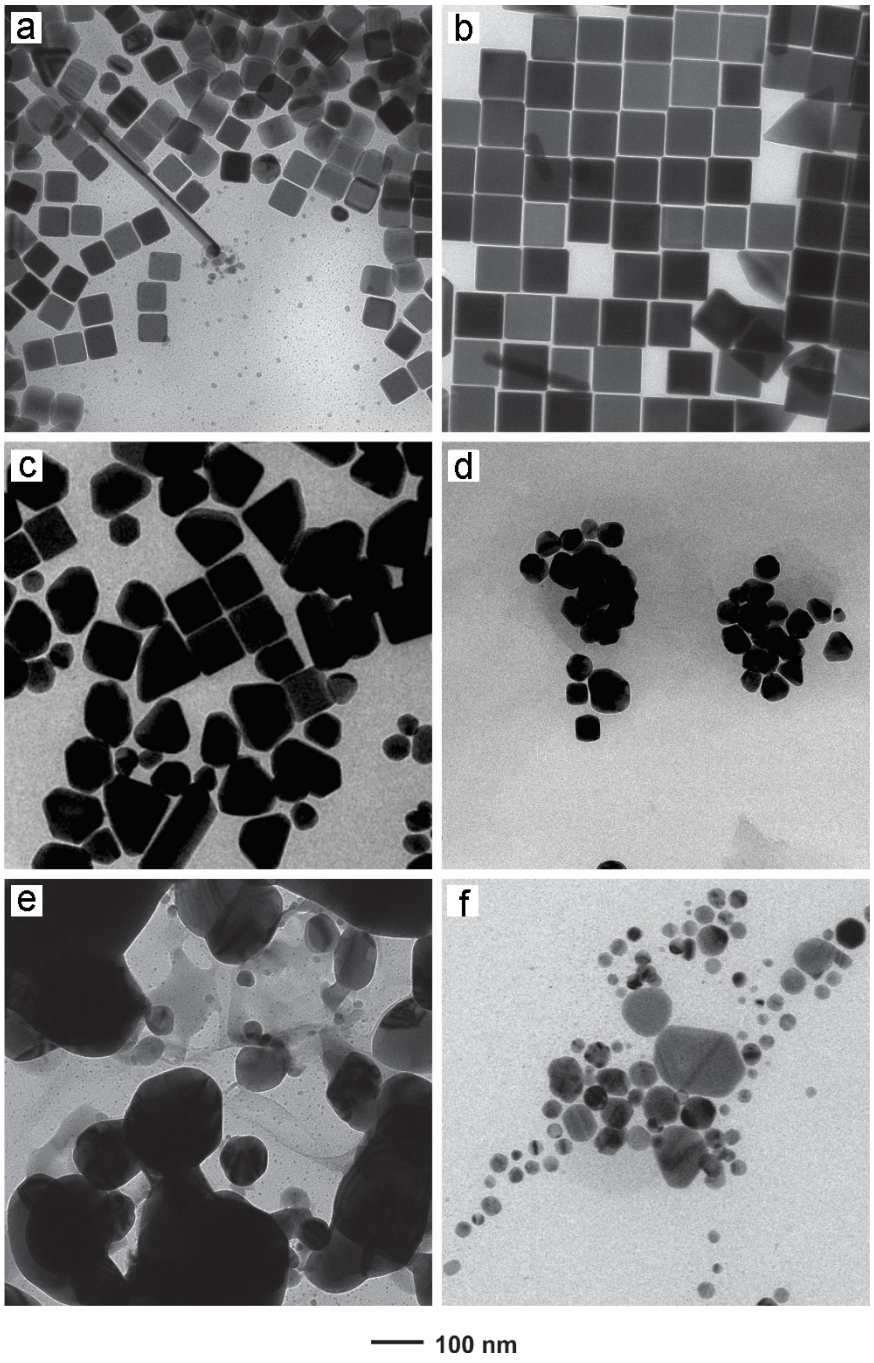

Figure 2.10. TEM images of samples obtained under different reduction kinetics achieved through variation of reaction temperature: (a) 50 °C and (b) 70 °C; variation of pH value: (c) 2.7 and (d) 7.4; or variation of reducing agent: (e) formic acid and (f) $NaBH_4$. All other conditions were kept the same as the standard protocol and the products were collected at t = 6 h into the synthesis. (Reprinted with permission from [42]. Copyright 2016 American Chemical Society.)

I also examined the impact of reducing agent on the final products by replacing the AA in the standard protocol with formic acid or $NaBH_4$. The products were made of AgCl in the absence of an externally added reductant. When formic acid instead of AA was used, the products were still mainly composed of AgCl (Figure 2.10e). Formic acid is known to have a weaker reducing power than AA, which might be inadequate to reduce most of the AgCl to Ag within 6 hours [40]. When switched to a much stronger reducing agent like $NaBH_4$, all the AgCl nanocrystals were gone by t = 6 h, but the final products mainly contained small particles with an irregular shape (Figure 2.10f). Taken together, the use AA at a pH value around 3.1 seems to be optimal for the synthesis of Ag nanocubes in a high morphological yield.

A proper concentration of Cl^- ions is also important for regulating the reduction kinetics. In the current protocol, the Cl^- ions were supplied by the CTAC. It is worth pointing out that the concentration of CTAC used in the standard synthesis was 20 mM, much higher than its critical micelle concentration (CMC), which is 1.62 mM at 60 ^oC [41]. As such, the concentration of free Cl^- ions in the reaction solution should be much lower than 20 mM. When replacing the CTAC with an equal molar amount of NaCl for the standard protocol, the solution was colorless after heating at 60 ^oC for 6 h (Figure 2.11) and no solid products could be obtained by centrifugation at a speed as high as 12,000 rpm. This phenomenon can be explained by considering the equilibrium between AgCl and $AgCl_2^-$:

$$Ag^+ + Cl^- \leftrightarrow AgCl \quad (1)$$

$$AgCl + Cl^- \leftrightarrow AgCl_2^- \quad (2)$$

In comparison with AgCl, it is much more difficult to reduce $AgCl_2^-$. In the case of NaCl, the concentration of Cl^- ions was much higher than that of Ag^+ so most of the Ag^+ ions were converted to the $AgCl_2^-$ form and thus no reduction could occur. That is the reason why the solution remained clear and no solid products could be obtained at a centrifugation speed of 12,000 rpm after 6 h. In the case of CTAC, however, the concentration of free Cl^- ions was significantly lower due to the formation of micelles, making the majority of Ag^+ ions stay in the AgCl form to allow reduction by AA. I also tested NaCl at lower concentrations to mimic the effect of CTAC. When the molar ratio of NaCl to CF_3COOAg was kept at 1:1, a mixture of large, irregular and cubic nanocrystals can be readily identified in the solution (Figure 2.12a), while no uniform Ag nanocubes were observed. Most of these nanocrystals were made of AgCl, which was confirmed by the energy-dispersive X-ray spectroscopy (EDX) mapping data in Figure 2.12b. This argument was also supported by the fact that most of these nanocrystals could be dissolved after soaking in 20 mM aqueous NaCl solution for 3 h. It is noteworthy that those AgCl nanocrystals were quite stable under the electron beam during the SEM characterization, which might be the result of different facets exposed at the surface as compared to the AgCl octahedra. This result indicates that, besides a proper amount of Cl^- ions, the octahedral shape of the AgCl nanocrystals is also a key factor to the formation of Ag nanocubes, making it difficult to replace the CTAC with NaCl.

Figure 2.11. Photograph of a reaction solution, which remained transparent and colorless after heating at 60 °C for 6 hours, when an equal molar amount (0.1 mmol) of NaCl instead of CTAC was used. This can be explained by the formation of $AgCl_2^-$, which is more difficult to reduce by ascorbic acid than AgCl. (Reprinted with permission from [42]. Copyright 2016 American Chemical Society.)

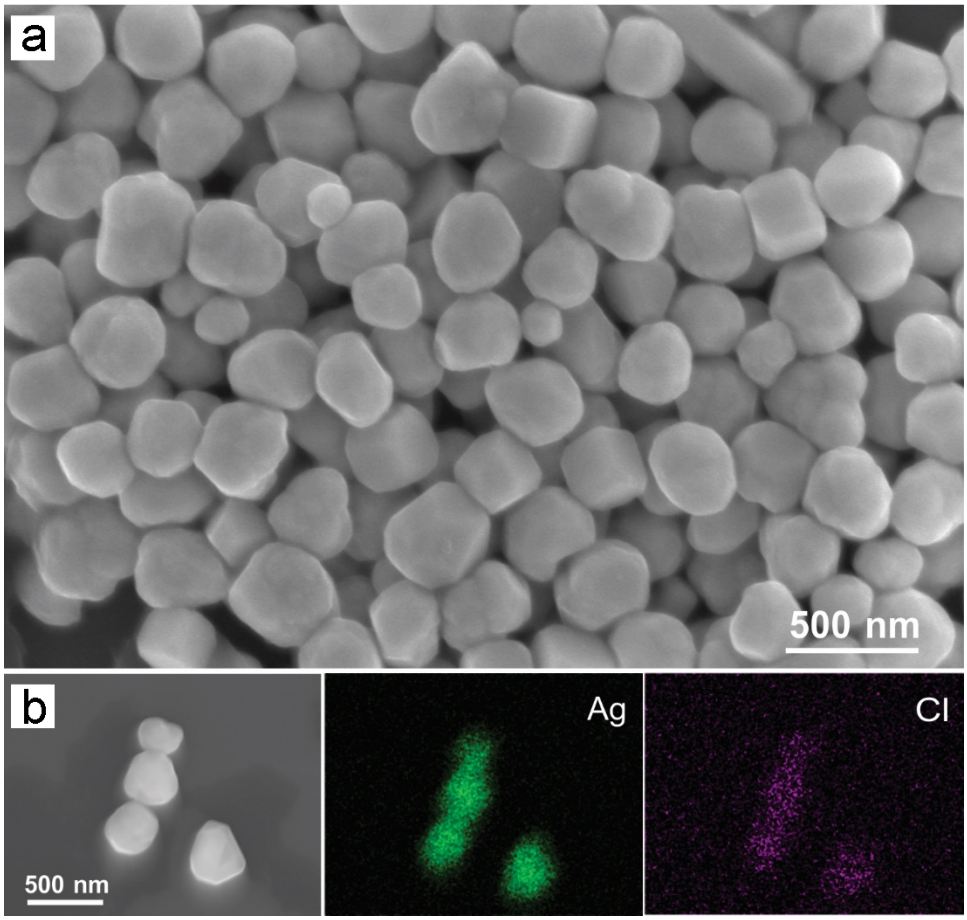

Figure 2.12. (a) SEM image of samples obtained under the conditions of a standard synthesis, except for the use of NaCl at the same molar amount as CF_3COOAg in the absence of CTAC. (b) SEM image of four AgCl nanocrystals and the corresponding EDX mapping of Ag and Cl. (Reprinted with permission from [42]. Copyright 2016 American Chemical Society.)

2.2.4 SERS Activity

The sharpness of my Ag nanocubes were further confirmed by their SERS activities (Figure 2.13). My colleague and I performed the measurements with 1,4-benzenedithiol (1,4-BDT) as the probe molecule and a 532 nm laser for excitation. The red curve shows the SERS spectrum recorded from a suspension of 93-nm Ag nanocubes, only with the introduction of 1,4-BDT adequate for the formation of a monolayer on the nanocubes. A reference solution with 0.05 M 1,4-BDT in aqueous NaOH was also measured to calculate

the surface enhancement factors (EFs) of the Ag nanocubes. The EF can be calculated by using expression (3):

$$\mathrm{EF} = \frac{I_{\mathrm{SERS}}}{I_{\mathrm{Bulk}}} \times \frac{N_{\mathrm{Bulk}}}{N_{\mathrm{SERS}}} \tag{3}$$

where I_{SERS} and I_{Bulk} are the intensities of the same band for the SERS and reference spectrum, N_{SERS} is the number of adsorbed molecules probed in the SERS spectrum, and N_{Bulk} is the number of molecules probed in the ordinary spectrum. I used the intensity of the peak at 1563 cm^{-1} to calculate the SERS enhancement factor, which gave a value of 1.34×10^5. Compared to the SERS enhancement factors of 100-nm nanocubes and 90-nm nanocubes with sharp corners and edges that were prepared in a polyol system with the assistance of Cl^- ions (*i.e.*, 1.25×10^5 and 1.26×10^5) [28], this value is compatible, confirming the presence of sharp corners and edges.

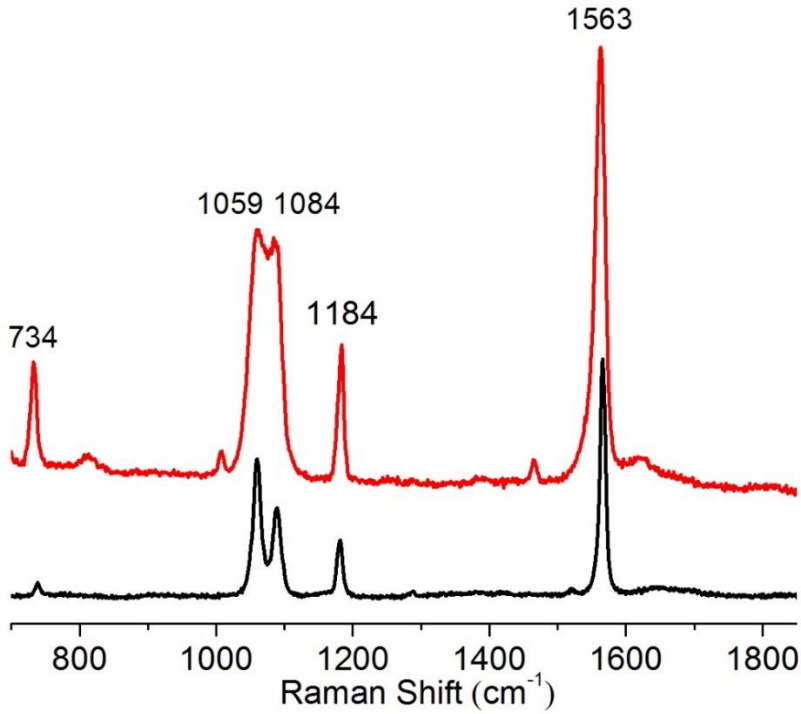

Figure 2.13. SERS spectrum (red curve) taken from an aqueous suspension of 93-nm Ag nanocubes whose surface had been covered with a monolayer of 1,4-BDT and ordinary spectrum (black curve) recorded from a 1,4-BDT solution (0.05 M) in 12 M aqueous NaOH. Both spectra were acquired with a 532 nm laser. (Reprinted with permission from [42]. Copyright 2016 American Chemical Society.)

2.3 Conclusion

In summary, I have successfully demonstrated an aqueous protocol for the synthesis of Ag nanocubes with an average edge length of 35-95 nm. Upon mixing CTAC with CF3COOAg, AgCl nanoscale octahedra are immediately formed. The presence of room light and a reducing agent such as ascorbic acid offers a proper reducing power to generate the Ag_n nuclei and to continuously provide elemental Ag for the evolution of Ag_n nuclei into Ag nanocubes. The capping of {100} facets by Cl^- ions and the use of relatively low

reaction temperature are both critical to retaining the sharp corners and edges on the Ag nanocubes. This synthetic method is appealing for bio-related applications, as well as plasmonic and SERS-based sensing, due to the involvement of aqueous solutions only. It also offers a more reproducible, environmentally friendly, and economical route to the synthesis of Ag nanocubes as compared to the widely used polyol process.

2.4 Experimental Section

Chemicals and materials. Cetyltrimethylammonium chloride (CTAC, 25 wt% in H_2O), ascorbic acid (AA, ≥99.0%), silver trifluoroacetate (CF_3COOAg, ≥99.99%), iron(III) chloride ($FeCl_3$, 97%), formic acid (≥95%), sodium borohydride ($NaBH_4$, ≥99%), sodium chloride (NaCl, ≥99.0%), and 1,4-benzenedithiol (1,4-BDT) were all purchased from Sigma-Aldrich and used as received. Deionized (DI) water with a resistivity of 18.2 MΩ·cm was used for all experiments.

Synthesis of Ag nanocubes. In a standard protocol, aqueous solutions of CTAC (5 mL, 20 mM) and AA (0.5 mL, 100 mM) were added into a 20 mL glass vial and heated at 60 ºC for 10 min. Aqueous solutions of CF_3COOAg (50 μL, 10 mM) and $FeCl_3$ (80 μL, 4.29 μM) were then added in one shot. The reaction solution had a pH value of about 3.1 during the entire synthesis. After 6 h, the products were collected by centrifugation at 8,000 rpm and re-dispersed in DI water. For the synthesis ended at an earlier stage, the speed of centrifugation was set to 17,500 rpm and the products were re-dispersed in ethanol. All the syntheses were carried out under room light (fluorescent lamp, Sylvania Fo25/835/Eco).

SERS measurements. The SERS spectra were measured using a protocol reported before [28]. To be specific, an aqueous solution of the as-obtained Ag nanocubes (0.063

mg/mL) and 1.2×10^{-3} mM 1,4-BDT were prepared one hour before SERS measurements. The 1,4-BDT was used at a concentration just enough to generate a monolayer on the Ag nanocubes by assuming a footprint of 0.54 nm^2. The reference solution was prepared by dissolving 1,4-BDT in cooled 12 M aqueous NaOH one hour prior to the measurement. The Raman spectra were recorded using a Renishaw inVia Raman spectrometer coupled with a Leica microscope using a 100× objective. The excitation wavelength was 532 nm, and the holographic notch filter has a grating of 2400 lines/mm. Data was collected from the solution phase with a collection time of 30 s at 50 mW for all the samples.

Characterization methods. The TEM images were taken using a Hitachi HT7700 microscope operated at 120 kV. The SEM images and EDX mapping were taken using a Hitachi SU8230 microscope. UV-vis extinction spectra were recorded on a Cary 60 spectrometer (Agilent Technologies, Santa Clara, CA). High-resolution TEM (HRTEM) images were acquired using JEOL 2100F microscope (JEOL, Tokyo, Japan) operated at 200 kV. The pH values were measured using a Fisher Scientific AB15 pH meter. SERS spectra were taken using a Renishaw inVia micro Raman system (Renishaw, Hoffman Estates, IL). Discrete dipole approximation (DDA) calculation was carried out using DDSCAT 7.3.

2.5 Notes to Chapter 2

Part of this chapter is adapted from the paper “Facile Synthesis of Silver Nanocubes with Sharp Corners and Edges in an Aqueous Solution” published in *ACS Nano* [42].

2.6 References

(1) Rycenga, M.; Cobley, C. M.; Zeng, J.; Li, W.; Moran, C. H.; Zhang, Q.; Qin, D.; Xia, Y. *Chem. Rev.* **2011**, *111*, 3669–3712.

(2) Zhang, Q.; Li, W.; Moran, C.; Zeng, J.; Chen, J.; Wen, L.-P.; Xia, Y. *J. Am. Chem. Soc.* **2010**, *132*, 11372–11378.

(3) Liang, H.; Wang, W.; Huang, Y.; Zhang, S.; Wei, H.; Xu, H. *J. Phys. Chem. C* **2010**, *114*, 7427–7431.

(4) Sun, Y.; Xia, Y. *Science* **2002**, *298*, 2176–2179.

(5) Siekkinen, A. R.; McLellan, J. M.; Chen, J.; Xia, Y. *Chem. Phys. Lett.* **2006**, *432*, 491–496.

(6) Im, S. H.; Lee, Y. T.; Wiley, B.; Xia, Y. *Angew. Chemie* **2005**, *44*, 2192–2195.

(7) Wang, Y.; Zheng, Y.; Huang, C. Z.; Xia, Y. *J. Am. Chem. Soc.* **2013**, *135*, 1941–1951.

(8) Ruditskiy, A.; Xia, Y. *J. Am. Chem. Soc.* **2016**, *138*, 3161–3167.

(9) Wiley, B. J.; Chen, Y.; McLellan, J. M.; Xiong, Y.; Li, Z.-Y.; Ginger, D.; Xia, Y. *Nano Lett.* **2007**, *7*, 1032–1036.

(10) Zhou, J.; An, J.; Tang, B.; Xu, S.; Cao, Y.; Zhao, B.; Xu, W.; Chang, J.; Lombardi, J. R. *Langmuir* **2008**, *24*, 10407–10413.

(11) Wang, Y.; Wan, D.; Xie, S.; Xia, X.; Huang, C. Z.; Xia, Y. *ACS Nano* **2013**, *7*, 4586–4594.

(12) Pietrobon, B.; Kitaev, V. *Chem. Mater.* **2008**, *20*, 5186–5190.

(13) Wiley, B. J.; Xiong, Y.; Li, Z.-Y.; Yin, Y.; Xia, Y. *Nano Lett.* **2006**, *6*, 765–768.

(14) Sun, Y.; Mayers, B.; Herricks, T.; Xia, Y. *Nano Lett.* **2003**, *3*, 955–960.

(15) Skrabalak, S. E.; Au, L.; Li, X.; Xia, Y. *Nat. Protoc.* **2007**, *2*, 2182–2190.

(16) Yang, X.; Yang, M.; Pang, B.; Vara, M.; Xia, Y. *Chem. Rev.* **2015**, *115*, 10410–10488.

(17) Cobley, C. M.; Skrabalak, S. E.; Campbell, D. J.; Xia, Y. *Plasmonics* **2009**, *4*, 171–179.

(18) Lim, B.; Jiang, M.; Tao, J.; Camargo, P. H. C.; Zhu, Y.; Xia, Y. *Adv. Funct. Mater.* **2009**, *19*, 189–200.

(19) Zeng, J.; Zheng, Y.; Rycenga, M.; Tao, J.; Li, Z.-Y.; Zhang, Q.; Zhu, Y.; Xia, Y. *J. Am. Chem. Soc.* **2010**, *132*, 8552–8553.

(20) Lin, Z.-W.; Tsao, Y.-C.; Yang, M.-Y.; Huang, M. H. *Chem. - Eur. J.* **2016**, *22*, 2326–2332.

(21) Ma, Y.; Li, W.; Cho, E. C.; Li, Z.-Y.; Yu, T.; Zeng, J.; Xie, Z.; Xia, Y. *ACS Nano* **2010**, *4*, 6725–6734.

(22) Samal, A. K.; Polavarapu, L.; Rodal-Cedeira, S.; Liz-Marzán, L. M.; Pérez-Juste, J.; Pastoriza-Santos, I. *Langmuir* **2013**, *29*, 15076–15082.

(23) Gong, J.; Zhou, F.; Li, Z.-Y.; Tang, Z. *Chem. Commun.* **2013**, *49*, 4379–4381.

(24) Zhu, C.; Zeng, J.; Tao, J.; Johnson, M. C.; Schmidt-Krey, I.; Blubaugh, L.; Zhu, Y.; Gu, Z.; Xia, Y. *J. Am. Chem. Soc.* **2012**, *134*, 15822–15831.

(25) Yu, D.; Yam, V. W.-W. *J. Am. Chem. Soc.* **2004**, *126*, 13200–13201.

(26) Yu, D.; Yam, V. W.-W. *J. Phys. Chem. B* **2005**, *109*, 5497–5503.

(27) Yin, Y.; Li, Z.-Y.; Zhong, Z.; Gates, B.; Xia, Y.; Venkateswaran, S. *J. Mater. Chem.* **2002**, *12*, 522–527.

(28) McLellan, J. M.; Siekkinen, A.; Chen, J.; Xia, Y. *Chem. Phys. Lett.* **2006**, *427*, 122–126.

(29) Hung, L.; Lee, S. Y.; McGovern, O.; Rabin, O.; Mayergoyz, I. *Phys. Rev. B* **2013**, *88*, 075424.

(30) Schuette, W. M.; Buhro, W. E. *ACS Nano* **2013**, *7*, 3844–3853.

(31) Zhu, Y.; Liu, H.; Yang, L.; Liu, J. *Mater. Res. Bull.* **2012**, *47*, 3452–3458.

(32) Long, R.; Zhou, S.; Wiley, B. J.; Xiong, Y. *Chem. Soc. Rev.* **2014**, *43*, 6288–6310.

(33) Ma, Y.; Li, W.; Zeng, J.; McKiernan, M.; Xie, Z.; Xia, Y. *J. Mater. Chem.* **2010**, *20*, 3586.

(34) Li, W.; Camargo, P. H. C.; Au, L.; Zhang, Q.; Rycenga, M.; Xia, Y. *Angew. Chemie* **2010**, *49*, 164–168.

(35) Cobley, C. M.; Rycenga, M.; Zhou, F.; Li, Z.-Y.; Xia, Y. *J. Phys. Chem. C* **2009**, *113*, 16975–16982.

(36) James, T. H. *The Theory of the Photographic Process*. New York Macmillan, **1977**.

(37) Tani, T. *Silver Nanocrystals: From Silver Halide Photography to Plasmons*; Oxford University Press, **2015**.

(38) Chang, S.; Chen, K.; Hua, Q.; Ma, Y.; Huang, W. *J. Phys. Chem. C* **2011**, *115*, 7979–7986.

(39) Yang, Y.; Liu, J.; Fu, Z.-W.; Qin, D. *J. Am. Chem. Soc.* **2014**, *136*, 8153–8156.

(40) Shi, L.; Wang, A.; Zhang, T.; Zhang, B.; Su, D.; Li, H.; Song, Y. *J. Phys. Chem. C* **2013**, *117*, 12526–12536.

(41) El Abdi, R.; Rujinski, A. D.; Poulain, M. *Eng. Sci. Technol. An Int. J.* **2015**, *18*, 52–58.

(42) Zhou, S.; Li, J.; Gilroy, K. D.; Tao, J.; Zhu, C.; Yang, X.; Sun, X.; Xia, Y. *ACS Nano* **2016**, *10* (11), 9861–9870.

CHAPTER 3

SITE-SELECTIVE GROWTH OF SILVER NANOCUBES, SHARPENING OF CORNERS AND EDGES, AND ELONGATION INTO NANOBARS THROUGH SYMMETRY REDUCTION

3.1 Introduction

Silver nanocrystals have received ever growing interest for their unique optical properties known as localized surface plasmon resonance (LSPR), as well as their niche applications in surface-enhanced Raman scattering (SERS), catalysis, and sensing [1-4]. Silver nanocubes with well-defined {100} side faces and sharp corners and edges, in particular, are instrumental to both catalysis and sensing. For example, the {100} facets on Ag nanocubes were reported to be more selective toward ethylene epoxidation relative to other types of surface structures [5]. On the other hand, compared to their truncated counterparts, Ag nanocubes with sharp corners and edges give much stronger SERS enhancement for a variety of thiol molecules, including aliphatic and aromatic compounds [6]. These and other examples demonstrate that there is a pressing need to produce Ag nanocubes with sharp corners and edges, maximizing the {100} facets to the greatest proportion.

Polyol reduction is the most commonly used method for the synthesis of Ag nanocubes. A one-pot protocol is often used, which involves the reduction of $AgNO_3$ or CF_3COOAg by ethylene glycol (EG) at an elevated temperature [2,7-9]. The elevation in temperature (typically in the range of 140-160 ºC) is needed to activate the reducing power of the polyol by generating glycol aldehyde through air-based oxidation [10]. In a recent

demonstration, Br^- ions were introduced as a strong capping agent to facilitate the formation of small Ag nanocubes with sizes (see Figure 3.1 for the definition) down to 13 nm [7]. However, due to the acceleration of surface diffusion and oxidative etching at elevated temperatures, the as-obtained Ag nanocubes showed notable truncations at the corners and edges. In contrast to the polyol synthesis, a room-temperature, water-based method should be more effective in generating and maintaining Ag nanocubes with sharp corners and edges. So far, the water-based protocol has only been applied in the one-pot setting, for the production of Ag nanocubes 35 nm in size [6]. It is not clear if the capability of such a one-pot synthesis can be further extended to generate Ag nanocubes smaller than 20 nm.

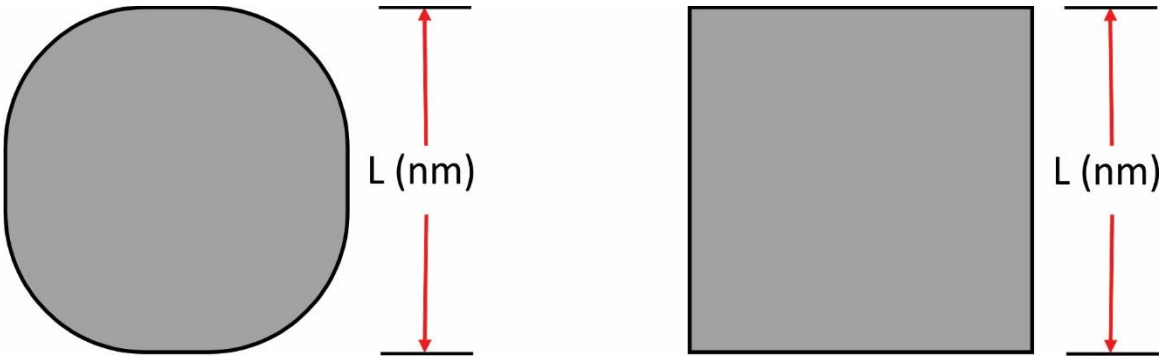

Figure 3.1. Illustration showing the definition of size (L) for a truncated nanocube and a nanocube with sharp corners and edges. (Reprinted with permission from [36]. Copyright 2018 Royal Society of Chemistry.)

Seed-mediated growth has been demonstrated as an alternative route to the synthesis of Ag nanocubes with small sizes. Single-crystal seeds made of different metals, such as Pd, Pt, Au and Ag, have all been explored for the generation of Ag nanocubes with variable sizes, albeit in a core-shell structure when different metals are involved [11-15]. For instance, a recent paper reported that Ag nanocubes with sizes in the range of 23-60 nm could be readily obtained from Ag-based seeds [13]. In this report, Ag seeds of 1-5 nm in

size were prepared through the rapid reduction of $AgNO_3$ by $NaBH_4$, while seed-mediated growth was conducted using ascorbic acid (AA) and CTAC in an aqueous medium. A considerable number of bipyramids could also be identified in the sample of 23-nm nanocubes (see Figure 3.2a), which might be caused by the variations in internal twin structure for the Ag seeds and/or the undesired self-nucleation during seed-mediated growth. Because the seed-mediated growth was conducted at 60 °C, both surface diffusion and oxidative etching could occur to a greater extent when compared with room-temperature synthesis. Figure 3.2 also shows three other examples of Ag nanocubes reported in literature [7,13,16]. All these samples of Ag nanocubes showed noticeable truncation at corners and edges.

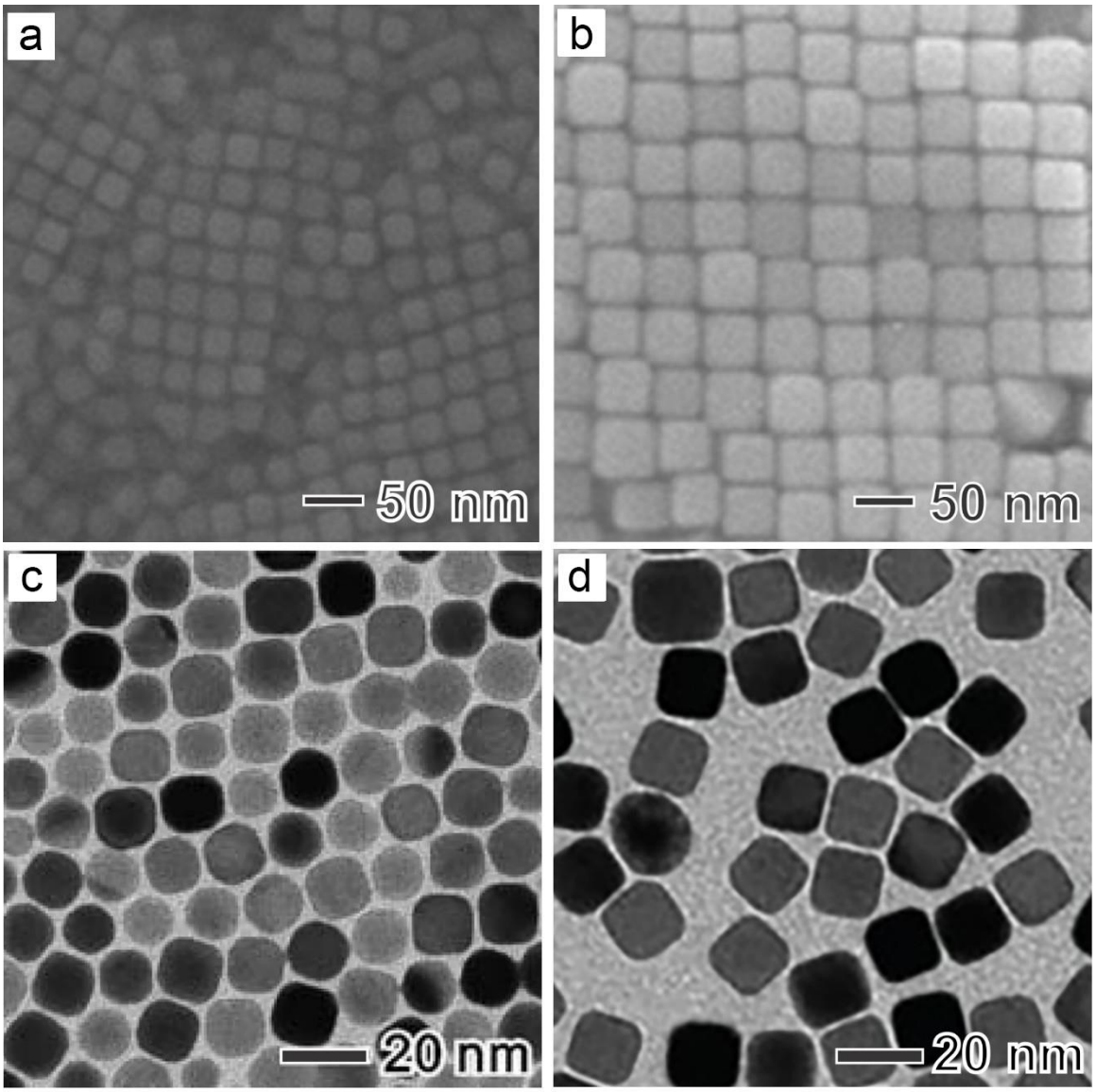

Figure 3.2. Comparison of Ag nanocubes reported in literature, which were synthesized using different protocols. (a and b) SEM image of the Ag nanocubes with edge lengths of (a) 23 nm and (b) 43 nm, respectively, obtained using seed-mediated growth in an aqueous system [13]. (c) TEM image of the Ag nanocubes with an edge length of 14 nm synthesized in isoamyl ether with Fe(III) as an oxidative etchant [16]. (d) TEM image of the Ag nanocubes with an edge length of 13 nm obtained using a Br^--mediated polyol method [7]. It is worth noting that all these Ag nanocubes suffer from severer truncation at corners and edges than the Ag nanocubes reported in the present work. (Reprinted with permission from [36]. Copyright 2018 Royal Society of Chemistry.)

To sharpen the corners and edges of Ag nanocubes while maintaining the compact size, it is necessary to only induce and maintain selective growth on the corners and edges

of truncated Ag nanocubes. Such site-selective growth has been extensively explored for the synthesis of bimetallic nanocrystals, and the exclusive deposition of atoms on the corners and edges of a seed are typically achieved through the use of a strong capping agent towards the side faces and the introduction of a very small amount of metal precursor to the growth solution, along with a relatively low reaction temperature to suppress the diffusion of adatoms to/across the side faces [17-19]. Although this method has been successfully applied to a few systems for the generation of core-frame nanocrystals, there is no report on its capability to mitigate the truncation of Ag nanocubes and thereby generate Ag nanocubes with sharp corners and edges.

Similar to Ag nanocubes, Ag nanobars are also enclosed by six {100} facets. Both of them should have similar performance in terms of catalytic application. In addition, nanobars display two resonance peaks because of the difference in dimension along the longitudinal and lateral directions [20]. Compared to Ag nanocubes, there are a significantly fewer number of reports on the synthesis of Ag nanobars [20,21]. In general, ionic bromide compounds were found to be effective in promoting the formation of Ag nanobars. However, all the protocols are exclusively based on polyol reduction at elevated temperatures, and a water-based protocol would be of great interest if sharp corners and edges are desired.

In this work, I demonstrate the use of seed-mediated growth in an aqueous medium and at room temperature for the facile synthesis of Ag nanocubes and nanobars with sharp corners and edges. The synthesis started from the site-selective growth of truncated Ag nanocubes, in which atomic deposition occurred selectively on the corners and edges in the presence of a strong capping agent towards {100} facets. I investigated different types of

capping agents, and CTAC was identified as the most effective one in sharpening the corners and edges of Ag nanocubes with sizes down to 18 nm. The CTA^+ ions were proven to be important for stabilizing the colloidal suspension. The Cl^- ions were shown to be less corrosive relative to Br^- ions, which could help preserve the sharpened corners and edges. Interestingly, the growth mode was switched from symmetric to asymmetric once Ag nanocubes with a perfect cubic shape were formed, and the atomic deposition favorably occurred on one of the six side faces of the sharpened Ag nanocubes. This symmetry breaking event allowed for the generation of Ag nanobars with aspect ratios up to 2. The as-synthesized Ag nanocubes were further explored for the fabrication of compact Au nanocages with absorption in the near-infrared region.

3.2 Results and Discussion

3.2.1 Seed-mediated Synthesis of Sharp Ag Nanocubes

The synthesis of Ag nanocubes with sharpened corners and edges involved two steps: preparation of Ag seeds with truncated corners and edges in EG and further growth of these seeds in an aqueous system. In the first step, I followed the Br^--mediated polyol method to generate 15-nm Ag seeds with truncated corners and edges [7]. As can be seen in Figure 3.3a, the as-synthesized Ag seeds had a slightly truncated, cubic shape, with an average size of 15.3 ± 0.7 nm. After washing and centrifugation, the particles were re-dispersed in water and used as seeds for site-selective growth.

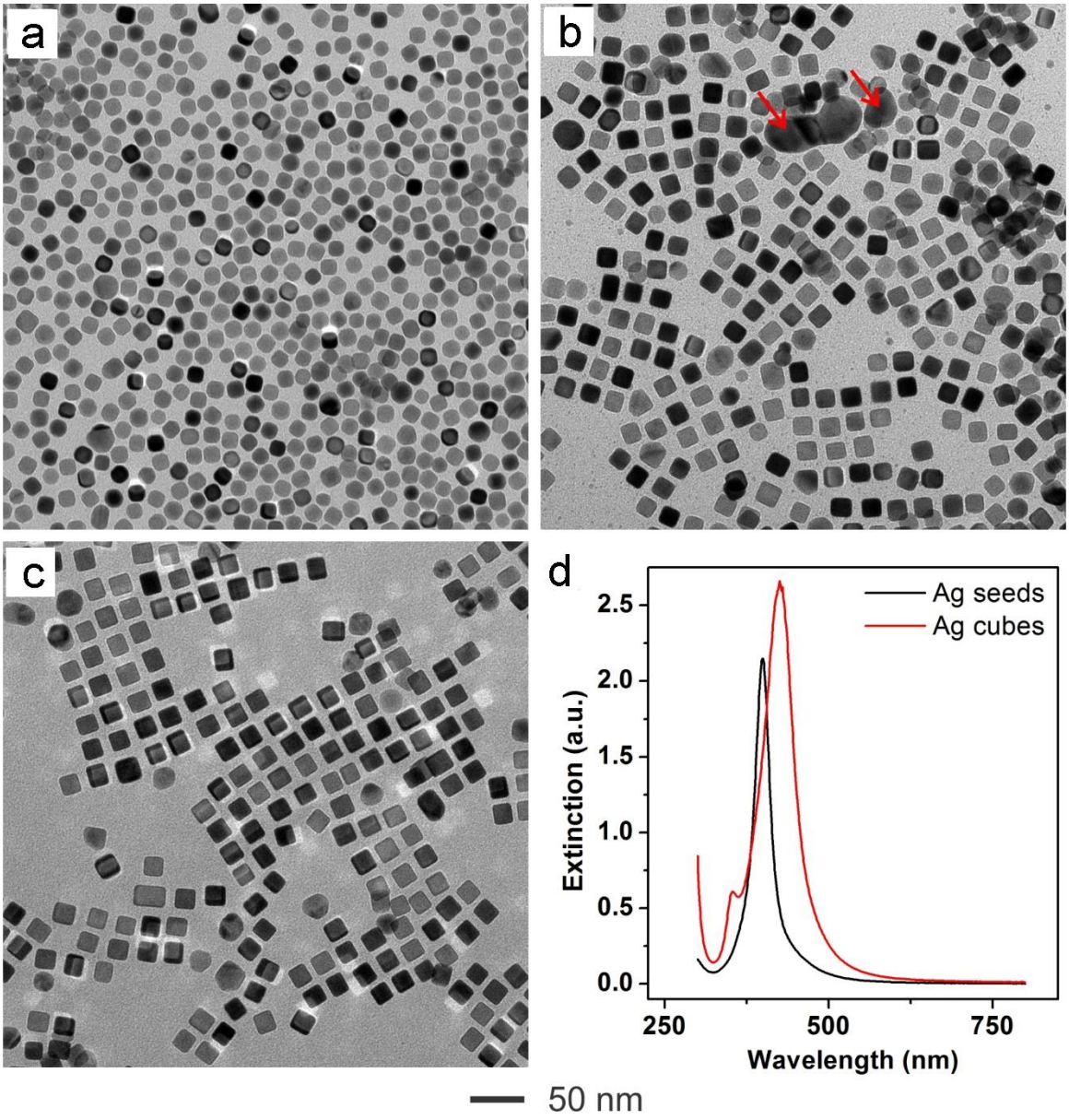

Figure 3.3. (a) TEM images of the Ag seeds obtained from a polyol synthesis. (b and c) TEM images of the Ag nanocubes synthesized using seed-mediated growth under the capping of CTAC at 12 h and 24 h, respectively. At t = 12 h, there was still a small amount of AgCl particles (indicated by arrows) in the final products, which disappeared at t = 24 h. (d) UV-vis spectra recorded from aqueous suspensions of the Ag seeds and Ag nanocubes with sharp corners and edges obtained at t = 24 h. (Reprinted with permission from [36]. Copyright 2018 Royal Society of Chemistry.)

I conducted seed-mediated growth with CTAC as a capping agent at room temperature for 24 h, with the use of CF_3COOAg and AA as the precursor and reducing agent,

respectively. I assumed that all the truncated nanocubes were spherical in shape to estimate the amount of CF_3COOAg needed to transform them into a perfectly cubic shape. Similar to the one-pot synthesis of Ag nanocubes in water, AgCl nanocrystals were immediately formed upon mixing CF_3COOAg with CTAC, which then served as the precursor to elemental Ag in the growth process [6]. At t = 12 h, there were still noticeable AgCl nanocrystals (Figure 3.3b) while the Ag nanocubes already started to show sharpened corners and edges relative to the initial Ag seeds. When the reaction was continued to 24 h, there was essentially no AgCl remaining, and all the Ag nanocrystals appeared to have a nearly perfect cubic shape, see Figure 3.3c. The final size of the as-obtained Ag nanocubes was measured to be 18.3 ± 1.2 nm. Further increasing the reaction time to 6 days would cause slight truncations at the corners and edges, but the overall sharpness of the corners and edges was better than that of the initial seeds (Figure 3.4).

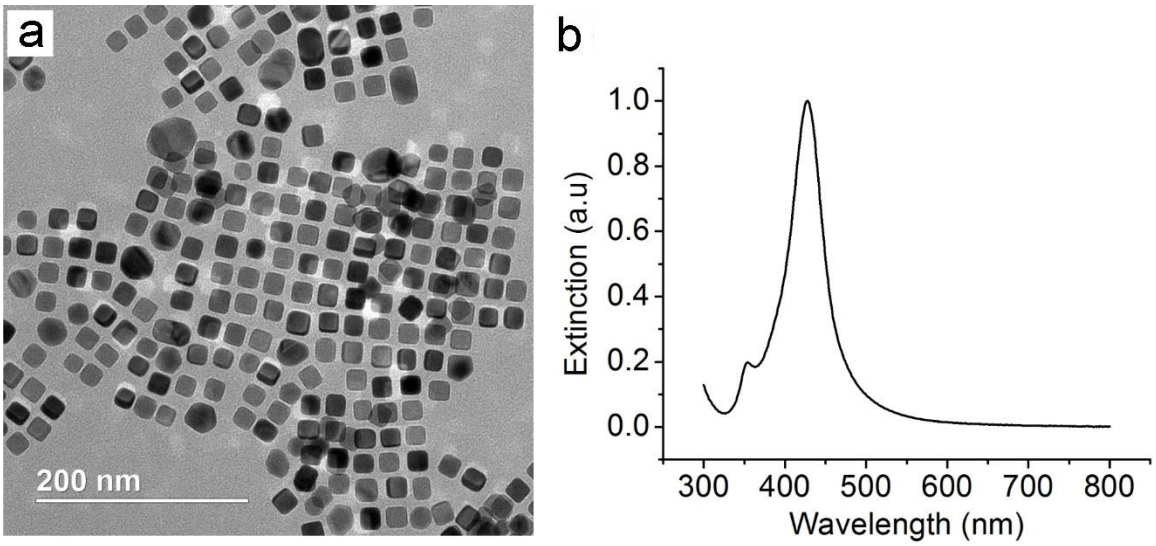

Figure 3.4. (a) TEM image of the Ag nanocubes synthesized with the introduction of 20 mM CTAC solution. The sample was collected at 6 days into the reaction. Most particles still maintained a cubic shape with slightly truncated corners and edges. The large, irregular AgCl particles were formed from the Ag^+ derived from oxidation. (b) UV-vis spectrum recorded from an aqueous suspension of the Ag nanocrystals. (Reprinted with permission from [36]. Copyright 2018 Royal Society of Chemistry.)

Compared to those Ag nanocubes reported in literature (Figure 3.2), the Ag nanocubes produced using my method were obviously truncated to a lesser extent at the corners and edges. It is worth mentioning that the synthesis was conducted in the absence of room light by wrapping the glass vial with aluminum foil. A control experiment indicated that if room light was allowed, more twinned nanocrystals (such as right bipyramids) could be identified in the final products (Figure 3.5), which could be assigned to the products of self-nucleation induced by the photo-reduction of the AgCl nanocrystals. It is also worth mentioning that replacing CF_3COOAg with $AgNO_3$ did not seem to change the quality of the Ag nanocubes, as shown in Figure 3.6.

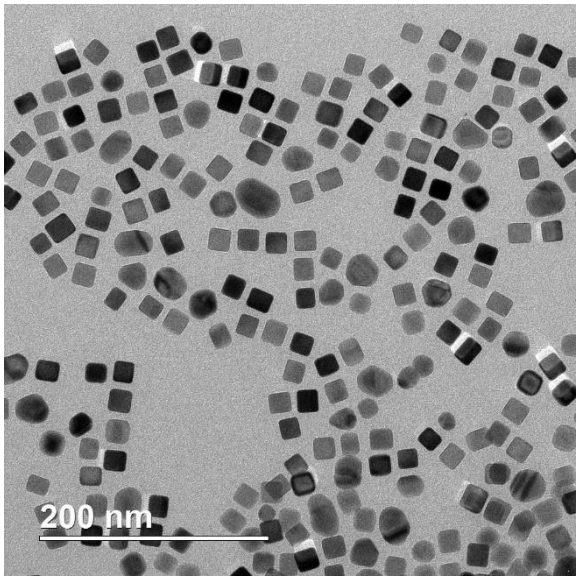

Figure 3.5. TEM image of the Ag nanocubes synthesized under room light. The sample was collected at 24 h into the reaction. The percentages of twinned particles and small single-crystal particles were higher than the sample presented in Figure 3.3c. (Reprinted with permission from [36]. Copyright 2018 Royal Society of Chemistry.)

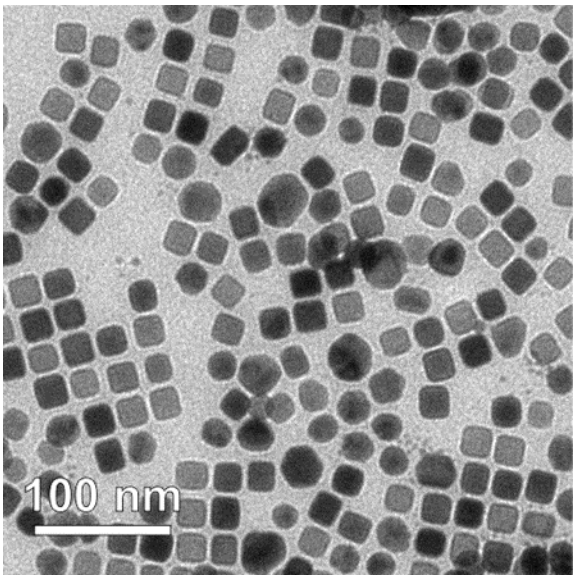

Figure 3.6. TEM image of the Ag nanocubes synthesized using $AgNO_3$ instead of CF_3COOAg. The sample was collected at 24 h into the reaction. (Reprinted with permission from [36]. Copyright 2018 Royal Society of Chemistry.)

The sharpening of the Ag nanocubes was further validated using UV-vis spectroscopy, Figure 3.3d. The Ag seeds only displayed one LSPR peak around 400 nm, indicating a more or less isotropic shape. After conducting the seed-mediated growth for 24 h, the intensity of the major LSPR peak increased, and the extinction spectrum also showed a shoulder peak around 354 nm, which can be assigned to the LSPR peak that only exists in sharp nanocubes as reported in previous work [23]. It is noteworthy that the main LSPR peak also shifted from 400 nm to 425 nm, suggesting the slight increase in size due to growth.

There are three possible roles for the Cl^- ions in this synthesis. First, Cl^- ions react with Ag^+ ions to generate AgCl nanocrystals at the very beginning of the synthesis, changing the source to elemental Ag. The amount of Cl^- ions plays an important role in determining the equilibrium between free Ag^+, AgCl, and $AgCl_2^-$ in the system and thereby altering the reduction kinetics and deposition pathway. Second, Cl^- ions can serve as a

relatively strong capping agent towards {100} facets, which is beneficial to preserving the sharp corners and edges on Ag nanocubes. Third, Cl^- ions can pair with O_2 to preferentially oxidize the Ag atoms at the corners and edges (eq. 1).

$$2Ag + 1/2O_2 + 2Cl^- + 2H^+ \rightarrow 2AgCl + H_2O \quad (1)$$

In order to figure out the optimal concentration of Cl^- to be used in a synthesis, I carried out a series of experiments with different amounts of CTAC. When there was no CTAC in the solution, big particles and aggregation of Ag nanocrystals were observed (Figure 3.7a), indicating the lack of stabilization for the colloidal suspension. When the concentration of CTAC was increased to 5 mM, the suspension of Ag nanocrystals was well stabilized against aggregation, see Figure 3.7b. However, the number of twinned particles seemed to be increased, and the nanocrystals tended to aggregate after centrifugation. Compared to the standard synthesis, the ratio of CTAC to Ag^+ in Figure 3.7b was lower (50:1 *vs.* 200:1), which lead to the formation of a larger amount of AgCl nanocrystals at the beginning of the synthesis. This means there was a higher possibility that twinned particles may be produced due to the in-particle reduction (*i.e.*, development) of AgCl by AA and thus undesired nucleation. When the amount of CTAC was further increased to 25 mM, the final products appeared to have slightly rounded corners (Figure 3.7c), which can be ascribed to the enhanced oxidative etching caused by Cl^-/O_2. Figure 3.7d shows the extinction spectrum of samples in Figure 3.7a-c. Taken together, it is clear that a proper concentration of CTAC should be chosen to prevent aggregation of Ag nanocrystals and development of AgCl nanocrystals, as well as to suppress oxidative etching power to preserve the sharp corners and edges.

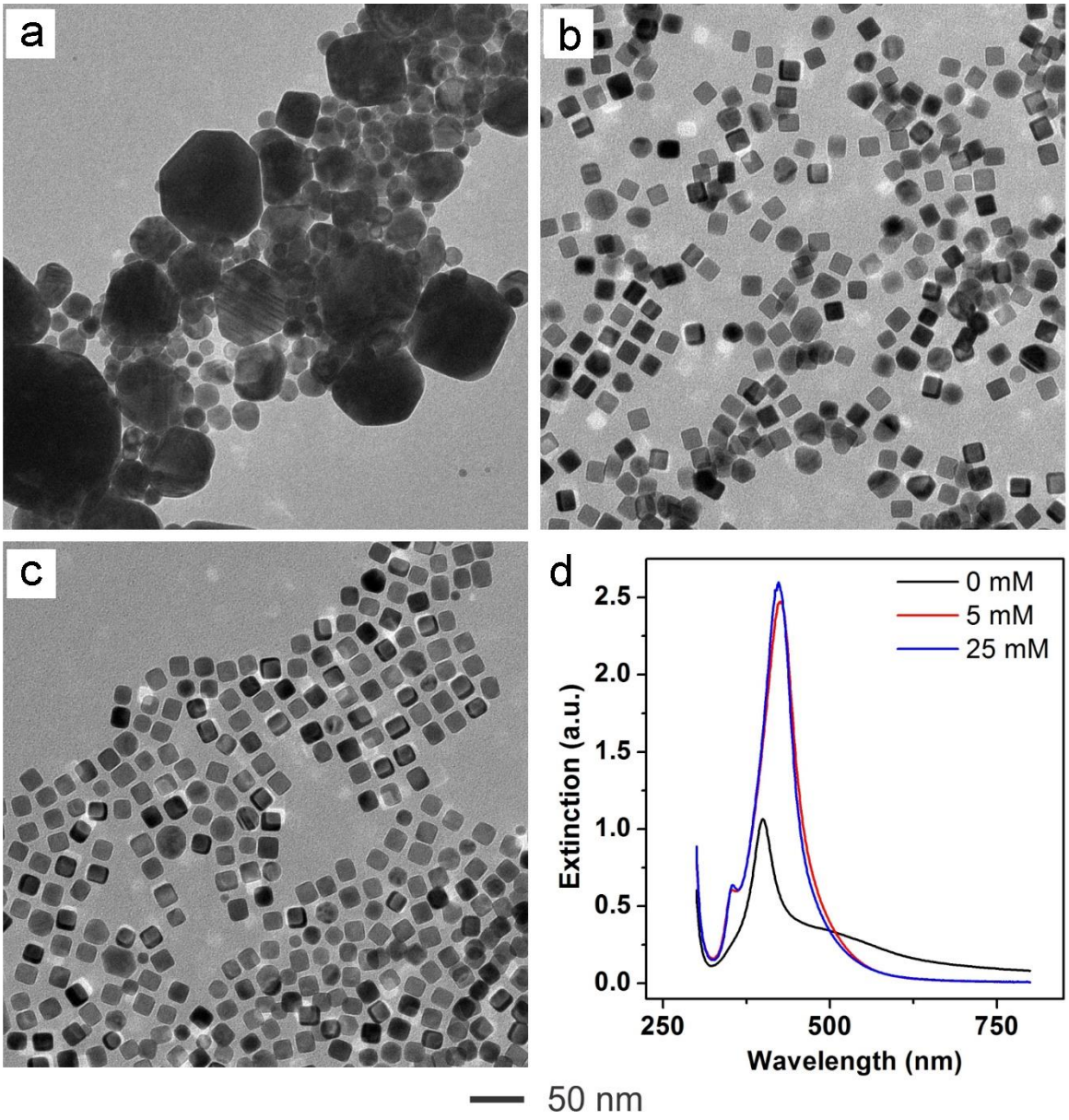

Figure 3.7. (a) TEM image of the Ag nanocrystals obtained without adding CTAC into the synthesis. (b and c) TEM images of the Ag nanocrystals obtained with the introduction of CTAC solutions with two different concentrations at (b) 5 mM and (c) 25 mM, respectively. (d) UV-vis spectra recorded from aqueous suspensions of the Ag nanocrystals shown in (a-c). (Reprinted with permission from [36]. Copyright 2018 Royal Society of Chemistry.)

In addition to the three roles played by Cl^- ions, CTA^+ is a critical component to the successful synthesis of sharp nanocubes. When CTAC was replaced by NaCl at the same molar concentration, all the particles appeared to be attached to the stir bar (Figure 3.8).

This indicates that besides the capping of Cl^- ions, the presence of CTA^+ is critical to the stabilization of the colloidal suspension in water. As shown in previous reports, CTA^+ ions could form a bilayer on the surface of the Ag nanocrystals, generating a hydrophilic surface to interact with water favorably [6]. The presence of the bilayer is necessary for dispersing Ag nanocubes in an aqueous medium without triggering aggregation.

Figure 3.8. Photograph showing a comparison of two different reaction solutions: (left) a standard synthesis and (right) a synthesis with the introduction of NaCl instead of CTAC. When replacing CTAC with NaCl, severe aggregations were observed in the reaction solution. (Reprinted with permission from [36]. Copyright 2018 Royal Society of Chemistry.)

3.2.2 Comparison of Different Capping Agents

To evaluate the influence of capping agent, I replaced CTAC with CTAB and PVP while all other experimental parameters were kept the same. Similar to CTAC, CTAB is also a quaternary ammonium surfactant and can form a bilayer on the surface of noble-metal nanocrystals [24,25]. The Br^- ions can also serve three same roles as Cl^- ions. First,

CTAB could form AgBr nanocrystals upon mixing with Ag^+ ions. However, the AgBr nanocrystals have a much lower reduction potential relative to that of AgCl (0.071 V *vs.* 0.22 V) [26], which will give a slower reduction rate, *i.e.*, a longer reaction time for the complete reduction of AgBr (more than 24 h). The Br^- ions can also serve as a strong capping agent towards the {100} facets of Ag nanocrystals, and induce oxidative etching with the assistance of O_2 [7,27,28].

When CTAB was used at a very low concentration of 1 mM, the products showed noticeable aggregation. Due to the low ratio of CTAB to Ag^+ (10:1), the amount of AgBr (rather than $AgBr_2^-$) formed in the synthesis was relatively large and could not be fully reduced within 24 h, resulting in big irregular particles shown in Figure 3.9a. The final products were not sharp at corners and edges, which might be due to the lack of effective capping as a result of inadequate Br^- ions. When the concentration of CTAB was increased to 5 mM, the final products showed sharpened corners and edges, and the amount of remaining AgBr was negligible, as shown in Figure 3.9c. The particle size was measured to be 15.7 ± 1.0 nm, which is very close to the initial size of the seed. This can be ascribed to the strong binding of Br^- ions to the Ag {100} facets. There were no major changes to the final products when the concentration of CTAB was in the range of 5-10 mM. However, when the concentration was further increased to 20 mM, the final products showed a large extent of truncation at corners and edges (Figure 3.9e), indicating the enhancement of oxidative etching. The enhanced oxidative etching was further confirmed by elongating the reaction time. At t = 48 h, most Ag nanocubes became rounded and AgBr nanocrystals started to appear again due to the release of free Ag^+ from the oxidative etching process.

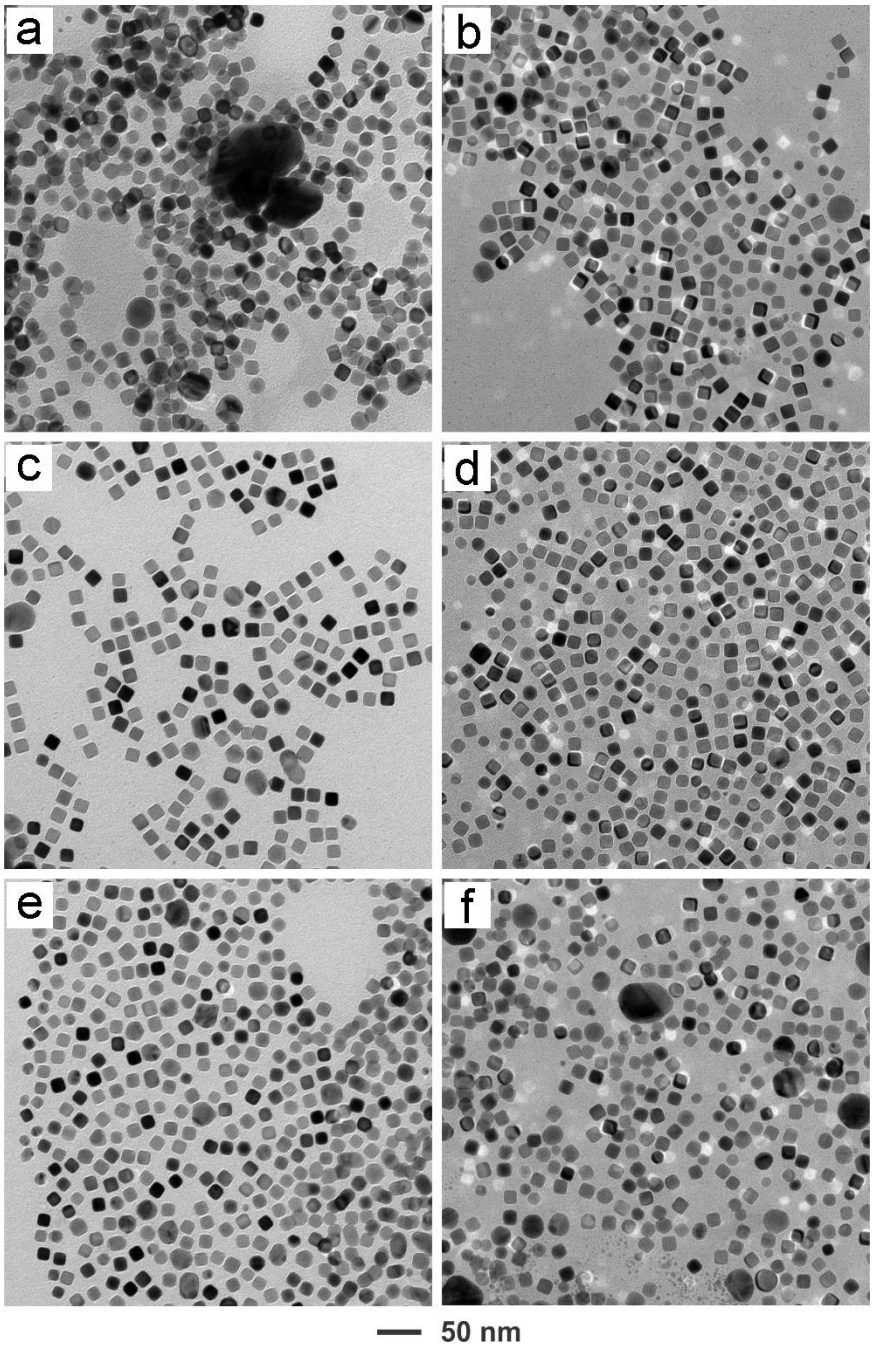

Figure 3.9. TEM images of the Ag nanocrystals synthesized with the introduction of CTAB solutions at three different concentrations of (a and b) 1 mM, (c and d) 5 mM, and (e and f) 20 mM. The samples in the left and right columns were collected at 24 h and 48 h, respectively. The average edge lengths of the Ag nanocubes in (c) and (e) were 15.7 ± 1.0, and 15.6 ± 0.9 nm, respectively. For the sample collected at 48 h, AgBr nanocrystals could be found in (f) as a result of severe oxidative etching. (Reprinted with permission from [36]. Copyright 2018 Royal Society of Chemistry.)

The UV-vis spectra of the as-synthesized Ag nanocubes did not show a distinct shoulder peak (Figure 3.10), again suggesting that Br^- is more corrosive and is detrimental in keeping the sharpened corners and edges at room temperature. Even though Br^- ions are better than Cl^- ions in terms of surfaced capping, CTAB is not ideal for sharpening Ag nanocubes.

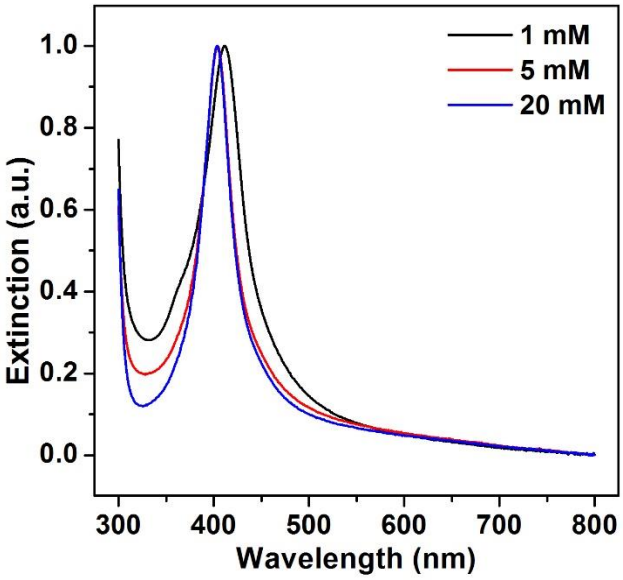

Figure 3.10. Normalized UV-vis spectra recorded from aqueous suspensions of the Ag nanocrystals synthesized with the introduction of CTAB solutions at different concentrations as shown in Figure 3.9a, c, and e. (Reprinted with permission from [36]. Copyright 2018 Royal Society of Chemistry.)

Unlike CTAC and CTAB, PVP is not a good capping agent for this water-based synthesis. When replacing CTAC with an equal molar concentration of PVP-55k, all the Ag nanocrystals showed a quasi-spherical shape, suggesting that PVP is not an effective capping agent toward the {100} facets in an aqueous system for Ag nanocrystals below 20 nm in size (Figure 3.11). When elongating the reaction time, the Ag nanocrystals tended to

aggregate, suggesting that PVP was not a good stabilizer either for Ag nanocrystals in an aqueous system.

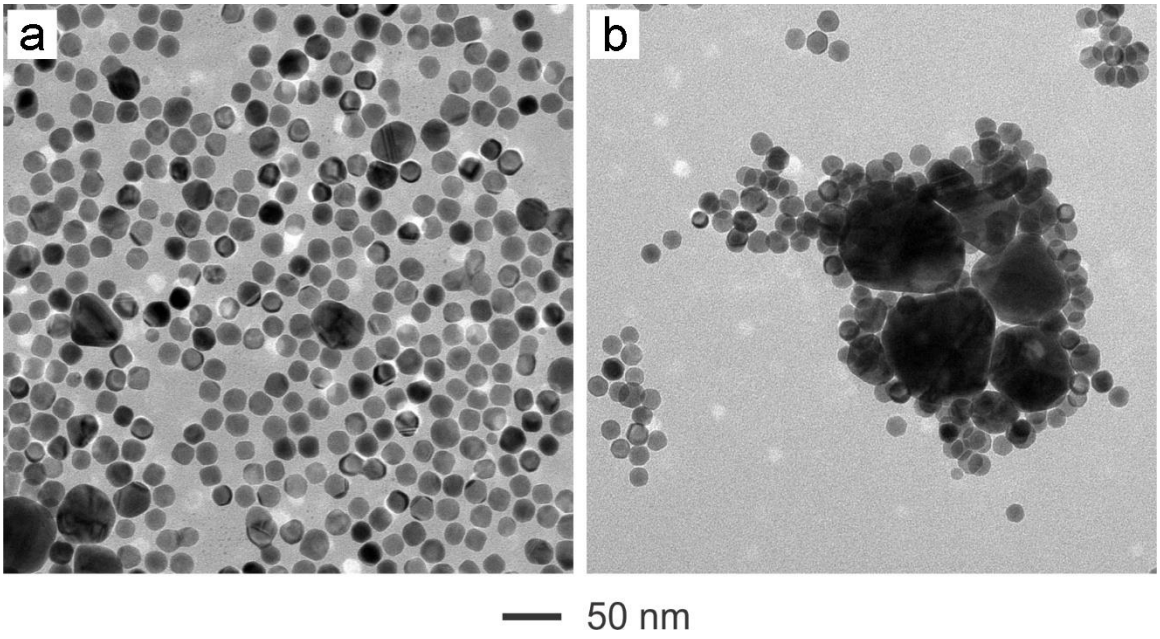

Figure 3.11. TEM images showing Ag nanocrystals synthesized using seed-mediated growth with the addition of 20 mM PVP-55k solution. The samples were collected at (a) 12 h and (b) 24 h, respectively, into the reaction. All the small Ag nanocrystals had a cuboctahedral shape. The aggregation of Ag nanocrystals became severer with the elongation of reaction time. The average sizes of the cuboctahedral Ag nanocrystals are (a) 18.5 ± 1.3 and (b) 18.9 ± 1.6 nm, respectively. (Reprinted with permission from [36]. Copyright 2018 Royal Society of Chemistry.)

For the seed-mediated growth of Ag nanocubes, the proper capping agent should be, in the first place, an effective colloidal stabilizer. The effectiveness of stabilization is determined by both the physical properties and the concentration of the capping agent. From the discussion above, both CTAC and CTAB were shown to be able to stabilize the Ag nanocrystals in water at a proper concentration. In order to sharpen the truncated Ag seeds, two other important properties of the capping agents need to be taken into consideration: the specific capping of {100} facets and the strength of oxidative etching. The binding strength of Br^- with Ag(100) appeared to be stronger than that of Cl^-, making

CTAB a better capping agent toward the {100} facets relative to Cl^- ions. In this case, Br^- ions were able to tightly limit the growth along <100> direction so the size of the final Ag nanocubes could be confined to a size similar to the original seed. On the other hand, Cl^- ions bound to Ag surface less strongly, slightly compromising the final size of the nanocubes from a sharpening process. With regard to the oxidative etching, however, Br^-/O_2 was more corrosive compared to Cl^-/O_2 in water at room temperature. The corners and edges of Ag nanocubes, which were more vulnerable to oxidative etching, would suffer from more truncation in the case of Br^- ions due to the enhancement in oxidative etching. In terms of sharpening the corners and edges of Ag nanocubes, CTAC tends to outperform CTAB.

3.2.3 Synthesis of Ag Nanobars Grown from Ag Nanocubes

It should be emphasized that the sharpening of Ag nanocubes in an aqueous medium relies on the slow reduction of AgCl nanocrystals and the strong capping of {100} facets by halide ions. Interestingly, once all the corners and edges have been sharpened, the nanocubes will evolve into nanobars through an asymmetric growth mode if more precursor is introduced.

Two different strategies have been adopted to obtain Ag nanobars. The first one involves the use of the sharpened Ag nanocubes as seeds for repeated rounds of seed-mediated growth. After each round of growth, the particles were collected and then re-dispersed in water and used as seeds for the next round of growth. Figure 3.12 shows TEM images of the nanobars obtained after different rounds of seed-mediated growth. After the first round, the length of the Ag nanobars was extended to 23.0 ± 2.6 nm, while the width only suffered a slight increase from 17.0 ± 1.0 to 17.5 ± 0.6 nm, see Figure 3.12a. After

another one and two rounds of growth, the length was increased to 27.5 ± 3.7 and 37.0 ± 7.2 nm, respectively, whereas the width slightly increased to 19.5 ± 1.7 and 23.2 ± 1.7 nm, as shown in Figure 3.12b and c. After the third round of growth, the products became Ag nanobars with an average aspect ratio of ~1.6. Figure 3.12d shows the corresponding UV-vis spectra of the three samples of Ag nanobars with different aspect ratios shown in Figure 3.12a-c. The presence of the shoulder peak at 520 nm indicates the longitudinal mode associated with the elongation of Ag nanocubes.

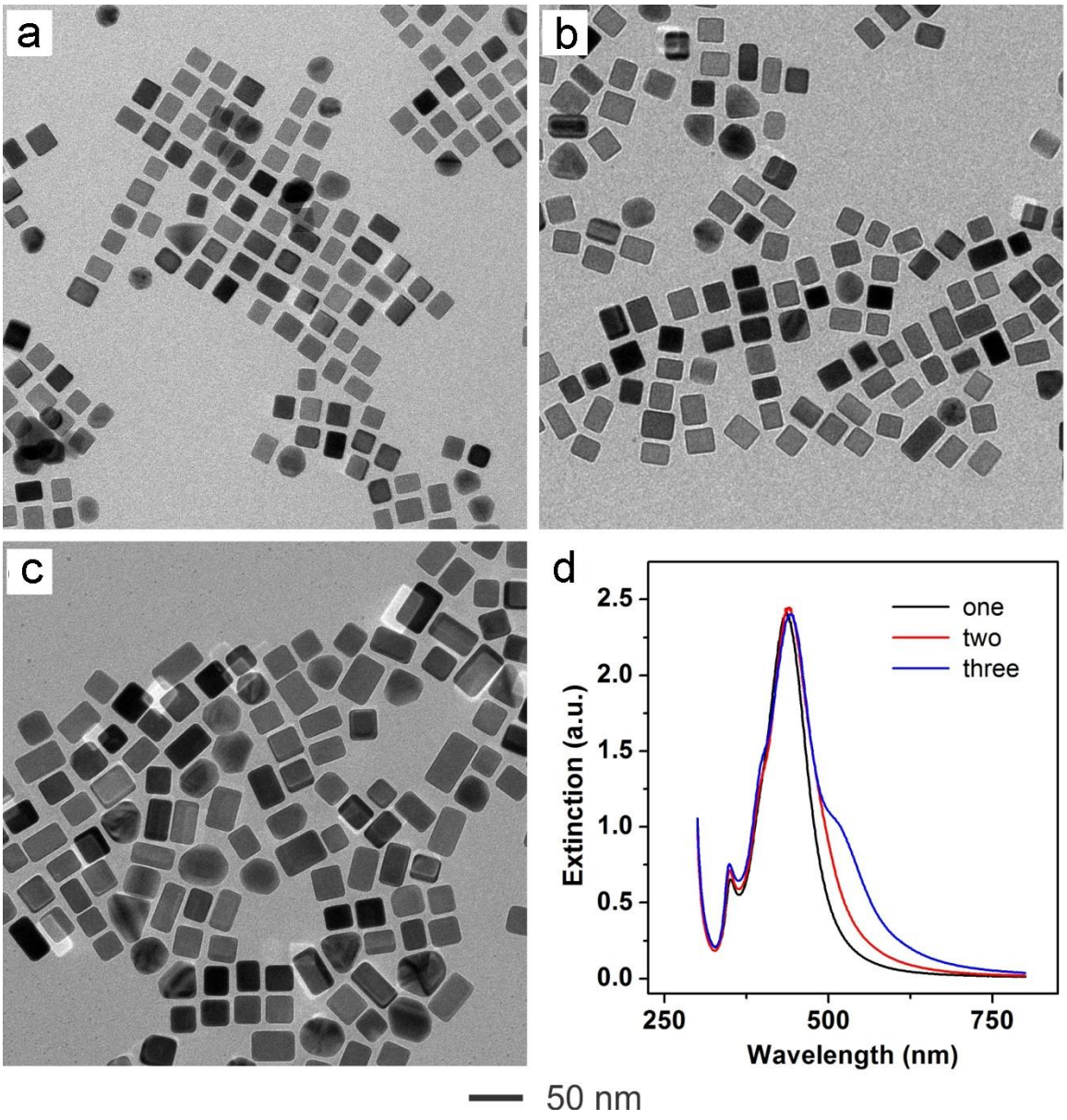

Figure 3.12. TEM images of the Ag nanobars synthesized after: (a) one, (b) two, and (c) three rounds of seed-mediated growth from the Ag nanocubes with sharp corners and edges shown in Figure 3.3c. In each step, the Ag particles from the previous synthesis were used as the seeds, and the products were collected, re-dispersed in 200 μl H_2O, and used for another round of seed-mediated growth. (d) UV-vis spectra recorded from aqueous suspensions of the corresponding nanocrystals shown in (a-c). (Reprinted with permission from [36]. Copyright 2018 Royal Society of Chemistry.)

Besides conducting multiple rounds of seed-mediated growth to obtain nanobars with various aspect ratios, a single round of growth could also be used by varying the amount

of seeds added. Figure 3.13a-c shows TEM images of Ag nanobars obtained by using different amounts of the sharpened Ag nanocubes as seeds. When 10 μL of Ag nanocubes was used for seed-mediated growth, the final products consisted of Ag nanobars with an aspect ratio of ~1.7, along with a small portion of right bipyramids. The formation of twinned particles can be attributed to the enhanced possibility of self-nucleation as a result of the insufficient amount of seeds for growth. When the amount of seeds was increased to 50 μL, the final products were mainly Ag nanobars with an aspect ratio of 2.0. The average length of the as-obtained nanobars was 41.5 ± 9.2 nm, while the width only increased to 21.1 ± 1.9 nm. The increased aspect ratio could be ascribed to the adequate amount of Ag seeds, which prevented the consumption of Ag precursor through the undesired self-nucleation. When the amount of seeds was further doubled, the as-obtained Ag nanobars had an aspect ratio of ~1.5, which can be attributed to the limited amount of precursor relative to the number of seeds in the reaction. Figure 3.13d shows the UV-vis spectra taken from these three samples. Compared to the extinction spectrum of the sharp Ag nanocubes, there was a broad shoulder peak at the region of 480-520 nm, which could be ascribed to the longitudinal LSPR peak of the Ag nanobars. There was also a shoulder peak at 395 nm for all three samples, which could potentially be the extinction of the by-products present in the final products.

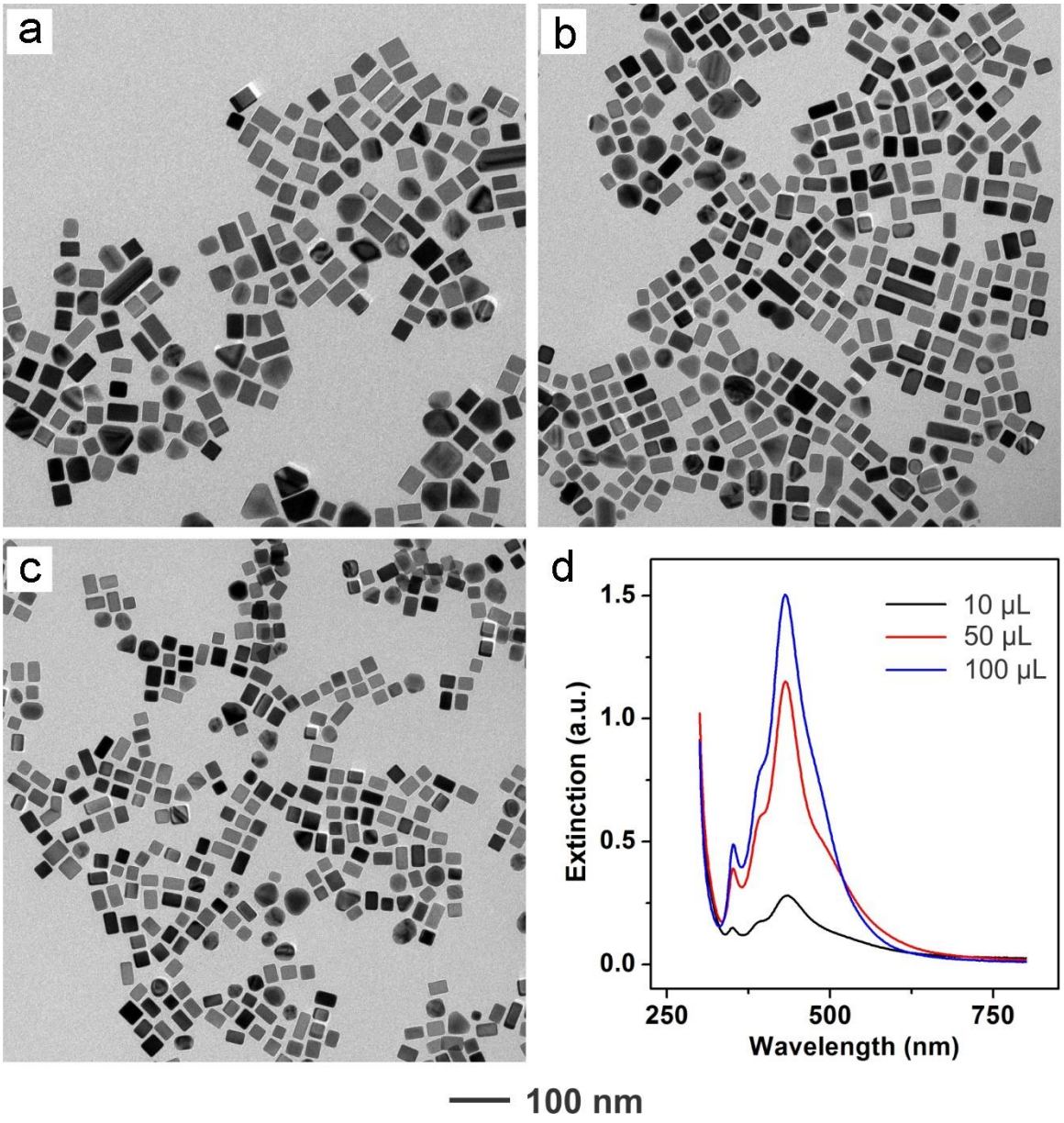

Figure 3.13. TEM images of the Ag nanobars obtained from one round of seed-mediated growth involving different amounts of Ag nanocubes with sharp corners and edges as the seeds: (a) 10, (b) 50, and (c) 100 μl of the aqueous suspension. (d) UV-vis spectra taken from aqueous suspensions of the corresponding nanocrystals shown in (a-c). (Reprinted with permission from [36]. Copyright 2018 Royal Society of Chemistry.)

3.2.4 Growth Mechanism

A plausible pathway is proposed based on the experimental results (Figure 3.14). The truncated Ag seed undergoes site-selective growth to evolve into a nanocube with

sharpened corners and edges. Once all the corners and edges are sharpened, a switch to the asymmetric growth mode occurs, leading to the formation of a Ag nanobar through symmetry breaking or reduction.

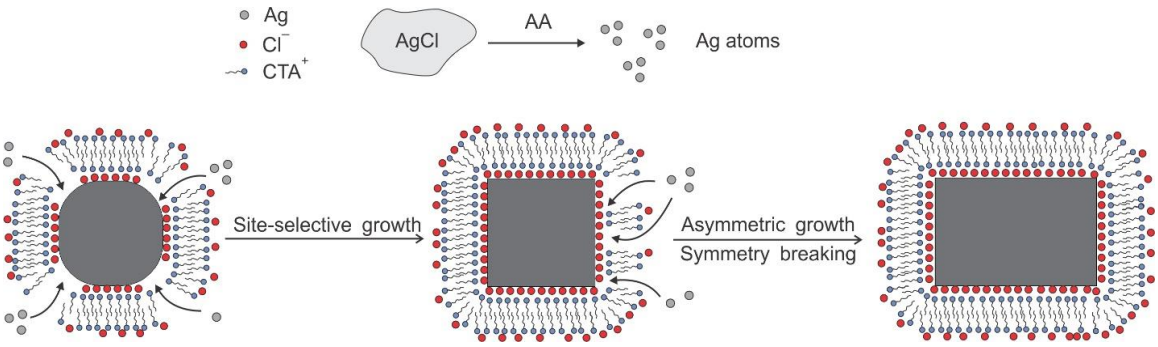

Figure 3.14. Schematic illustration showing the sequential formation of Ag nanocubes with sharp corners and edges and then nanobars through seed-mediated growth in an aqueous system in the presence of CTAC as a capping agent. (Reprinted with permission from [36]. Copyright 2018 Royal Society of Chemistry.)

The site-selective growth of the truncated Ag seed is accomplished by employing CTAC as a capping agent. During the mixing of CTAC with Ag seed, CTA^+ ions form a bilayer on the surface of the Ag nanocubes and the resultant particles can be well dispersed in water due to the hydrophilic nature of the outer layer. The Cl^- ions specifically bind to the {100} facets on the Ag seed, exposing the corners and edges for site-selective growth. Upon adding CF_3COOAg into the reaction solution, AgCl nanocrystals form immediately and then serve as the source to elemental Ag. The slow reduction of AgCl nanocrystals by AA supplies Ag atoms for the deposition onto all the corners and edges. The slow reduction kinetics prevents the formation of Ag nanocrystals through a homogeneous nucleation pathway. The absence of room light also greatly reduces the chances of forming Ag nuclei in AgCl nanocrystals (*i.e.*, the development of AgCl nanocrystals in the solid phase). The

site-selective deposition of Ag atoms eventually leads to the formation of a perfectly cubic shape for the Ag nanocubes.

After sharpening all the corners and edges, the growth mode changes from site-selective deposition to asymmetric growth to generate Ag nanobars. Previous reports have demonstrated the use of halide ions to promote the formation of nanobars [20,21,29]. It was suggested that the halide ions could induce localized oxidative etching and created active sites on one of the many facets on the seed for atom deposition, breaking the symmetry of the cubic structure and leading to the formation of nanobars [29]. Limiting the supply of atoms was also found to be an effective method for inducing symmetry breaking [30]. In accordance with the previous reports, the formation of Ag nanobars in my system can be ascribed to the use of CTAC as a capping agent. The formation of AgCl at the beginning of the synthesis greatly slows down the reduction kinetics and limits the supply of atoms. The strong capping by Cl^- towards the {100} facets also helps limiting the numbers of nucleation sites on the surface of seed. Once the first burst of atoms undergoes heterogeneous nucleation on one of the side faces of the sharpened Ag nanocubes, the following growth will preferentially occur on this facet, inducing the anisotropic growth of the Ag nanocubes to nanobars. The localized oxidative etching might also be involved in this process by selectively etching away Ag atoms from one of the side faces and thus activating it for subsequent atomic deposition.

3.2.5 Fabrication of Au-based Hollow Nanostructures

Gold-based hollow nanostructures have tunable optical absorption and scattering for applications in biomedicine [31-33]. Typically, Ag nanocubes are used as a sacrificial template to obtain the hollow nanostructures by leveraging the galvanic replacement

reaction with Au(III) or Au(I) [34,35]. Here, I demonstrate that Au-based hollow nanostructures with a better preserved cubic structure could be derived from the sharpened Ag nanocubes rather than truncated counterparts. Figure 3.15a-d shows TEM images of the Au-based hollow nanostructures derived from the truncated (Figure 3.15a and c) and sharpened nanocubes (Figure 3.15b and d). The hollow nanostructures derived from truncated Ag nanocubes had a cuboctahedral shape, indicating that the truncated corners were the preferred sites for galvanic replacement to occur. In contrast, the hollow nanostructures showed a cubic shape when the sharpened nanocubes were employed as a sacrificial template, with the center of facets slightly shrunken. Figure 3.15e and f shows the extinction spectra of Au-based hollow nanostructures when introducing different amounts of Au(III) precursor into the galvanic replacement reaction. It is clear that the main LSPR peak of the hollow nanostructures could be progressively shifted to 854 nm when using the sharp Ag nanocubes, whereas the peak was only red-shifted to 733 nm when employing the truncated nanocubes.

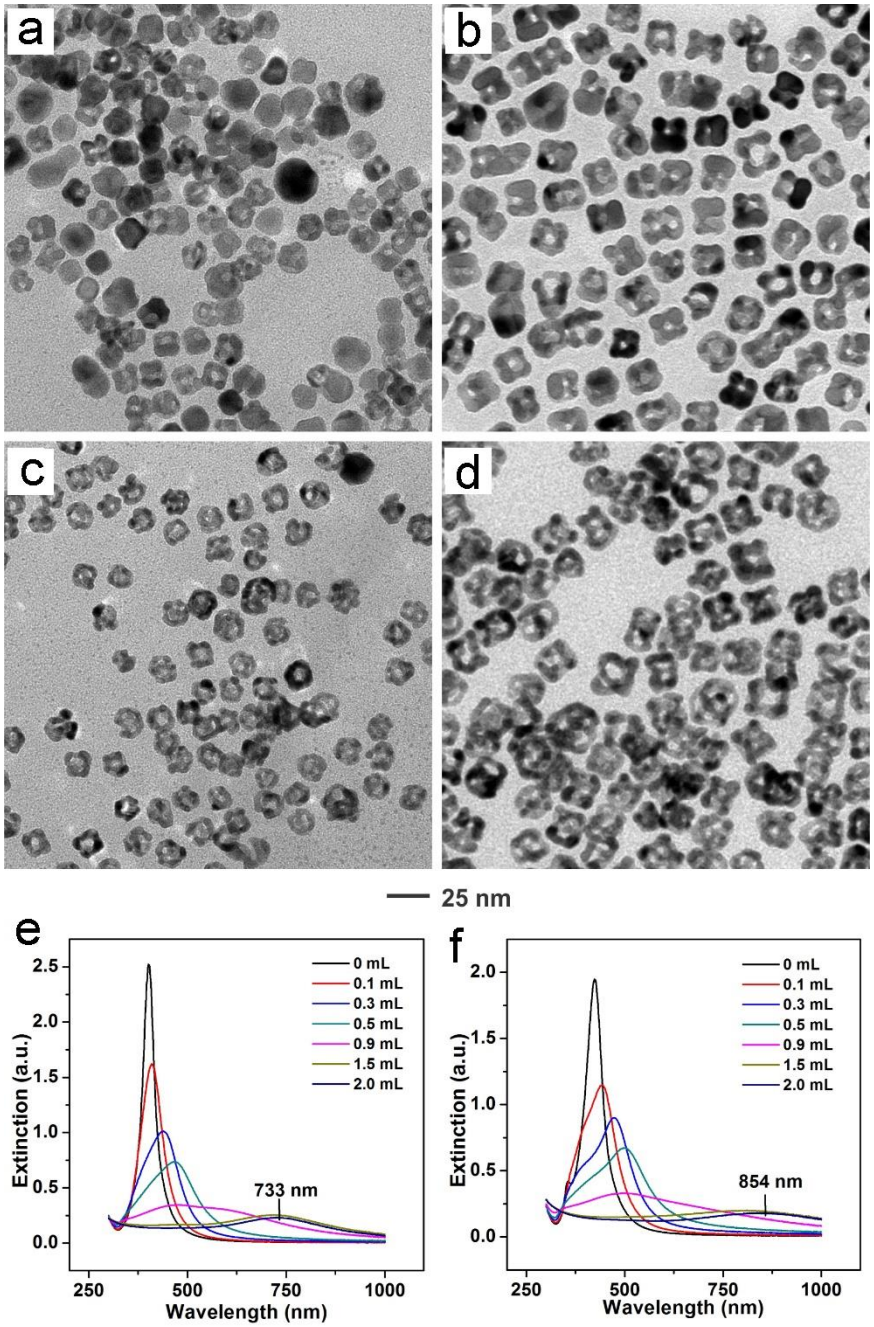

Figure 3.15. TEM images and UV-vis spectra of the Au hollow nanostructures prepared using a galvanic replacement reaction involving the use of Ag nanocubes with truncated (left column) and sharpened (right column) corners and edges as the sacrificial templates. (a and c) Samples obtained with the titration of 0.9 mL and 2.0 mL of 0.1 mM $HAuCl_4$, respectively. (b and d) Same as the samples shown in (a and c), except the use of Ag nanocubes with sharp corners and edges. (e and f) UV-vis spectra recorded from aqueous suspensions of the particles obtained with the titration of different volumes of $HAuCl_4$ solution. (Reprinted with permission from [36]. Copyright 2018 Royal Society of Chemistry.)

Qin *et al.* recently reported a new method for generating Au nanocages with ultrathin walls, in which a thin layer of Au was deposited onto the surface of Ag nanocubes, followed by selective removal of the Ag core by wet etching, generating Au nanocages with a well-defined thickness and morphology [22]. This protocol was also applied to both the sharpened and truncated Ag nanocubes, and the results indicated that most of the nanocages could maintain a cubic shape after the etching process when sharpened Ag nanocubes served as a sacrificial template. In comparison, more or less spherical Au nanocages were obtained for the truncated Ag nanocubes (Figure 3.16). Again, this result suggests that the sharpened Ag nanocubes are superior to their truncated counterparts when used as a sacrificial template for the fabrication of Au nanocages.

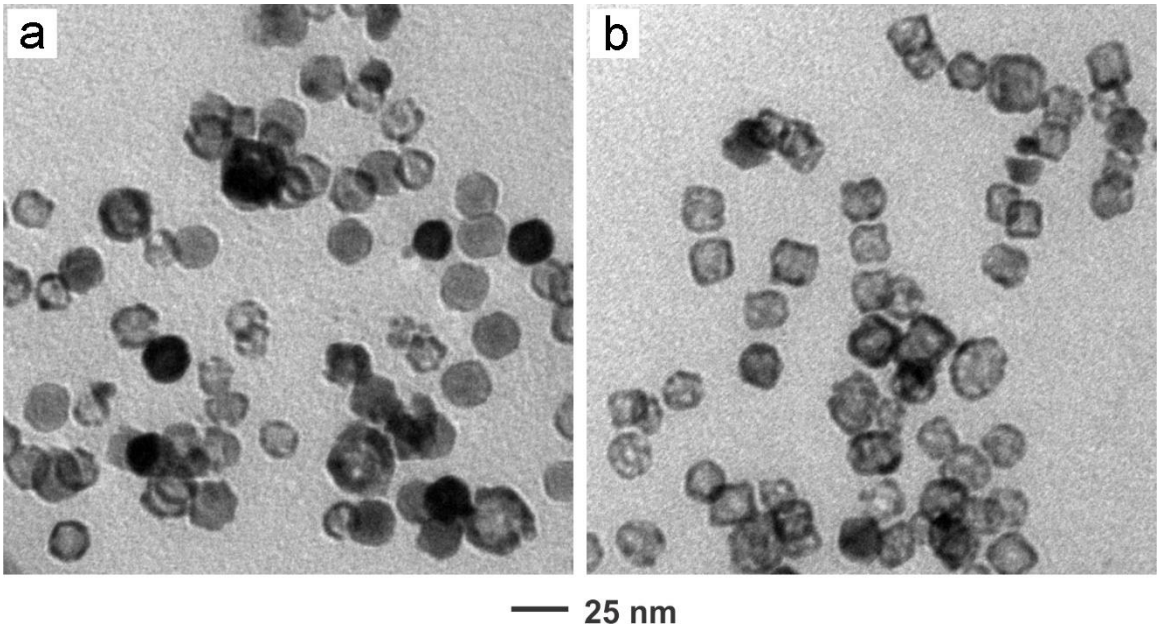

Figure 3.16. TEM images of the Au hollow nanostructures prepared through Au deposition and then selective removal of the Ag cores, using Ag nanocubes with (a) truncated and (b) sharp corners and edges as the substrates for Au deposition. (Reprinted with permission from [36]. Copyright 2018 Royal Society of Chemistry.)

3.3 Conclusion

In summary, I have demonstrated the facile synthesis of small Ag nanocubes with sharp corners and edges using a seed-mediated protocol in an aqueous system at room temperature. The colloidal stabilization capability, the specific binding towards {100} facets, and the strength of oxidative etching caused by the capping agent all play an essential role in sharpening the corners and edges of Ag cubic seeds in a site-selective fashion. Once the corners and edges are sharpened, the seed-mediated growth undergoes symmetry breaking or reduction, leading to the formation of Ag nanobars with aspect ratios up to 2. The sharpened Ag nanocubes can also serve as better sacrificial template for the fabrication of Au nanocages compared to the truncated counterpart. This research offers insights into the site-selective growth and symmetry breaking phenomena in nanocrystal growth. Compared to the more widely used polyol reduction, this synthetic method offers a milder and more environmentally friendly protocol.

3.4 Experimental Section

Chemicals and materials. Ethylene glycol (EG, ≥99.0%) was obtained from J. T. Baker. Silver trifluoroacetate (CF_3COOAg, ≥99.99%), sodium hydrosulfide hydrate ($NaHS \cdot xH_2O$), aqueous solution of hydrochloric acid (HCl, 37%), poly(vinylpyrrolidone) (PVP-55k, MW≈55,000; PVP-29k, MW≈29,000), sodium bromide (NaBr), sodium chloride (NaCl), cetyltrimethylammonium chloride (CTAC, 25 wt% in H_2O), ascorbic acid (AA, ≥99.0%), cetyltrimethylammonium bromide (CTAB, ≥99.0%), gold(III) chloride trihydrate ($HAuCl_4 \cdot 3H_2O$, ≥99.9%), and hydrogen peroxide (H_2O_2, 30 wt % in H_2O) were all ordered from Sigma-Aldrich. All chemicals were used as received. Deionized (DI) water with a resistivity of 18.2 MΩ·cm at room temperature was used throughout the experiments.

Synthesis of the Ag seeds. I closely followed the polyol method reported in literature without modification [7]. The synthesis was quenched by immersing the flask in an ice-water bath 4 min after the introduction of NaBr solution. After precipitation in acetone, the products were centrifuged three times at a relatively low speed of 4,000 rpm to separate the AgBr precipitates from the suspension of Ag seeds. The Ag seeds were further washed with water once and re-dispersed in water at a concentration of 0.296 mg/mL for further use.

Seed-mediated synthesis of Ag nanocubes. In a standard synthesis involving the use of CTAC as a capping agent, 5 mL of aqueous CTAC (20 mM), 0.5 mL of aqueous AA (100 mM), and 200 μL of the suspension of Ag seeds were added into a 20-mL glass vial and mixed at room temperature. The vial was wrapped with aluminum foil to minimize the influence of room light. About 10 min later, 50 μL of aqueous CF_3COOAg (10 mM) was injected into the vial in one shot. After 24 h, the products were collected by centrifugation at 12,000 rpm. The particles were re-dispersed in 200 μL of water for further use. For the syntheses involving other capping agents, the aqueous CTAC was replaced with an equal volume of aqueous CTAB or PVP with appropriate concentrations (1, 5, or 20 mM) while all other parameters were kept the same.

Seed-mediated synthesis of Ag nanobars. Two different methods have been developed for the synthesis of Ag nanobars. In the first method, 200 μL of the sharpened Ag nanocubes were used as seeds for the seed-mediated synthesis using the same conditions as for the growth of sharpened Ag nanocubes. After 24 h, the products were collected by centrifugation at 12,000 rpm and then re-dispersed in 200 μL of water to be used as seeds for another round of growth. This process was repeated multiple times to

obtain Ag nanobars with different aspect ratios. The second method used different volumes (10, 50, or 100 μL) of the sharpened Ag nanocubes as the seeds for one-round of growth using the same conditions as used for sharpening the Ag nanocubes. After 24 h, the nanocrystals were collected and re-dispersed in water for further characterization.

Synthesis of Au hollow nanostructures through galvanic replacement. In a standard synthesis, an aqueous suspension of Ag nanocubes with sharpened or truncated corners (0.1 mg in terms of Ag) were mixed with 4 mL of 1 mM aqueous CTAC at room temperature. After 5 min, 2.0 mL of 0.1 mM $HAuCl_4$ was added using a syringe pump at a rate of 0.04 mL/min. Aliquots were taken from the reaction solution at different time points for UV-vis measurements. The final products were collected by centrifugation at 16,000 rpm for 10 min.

Synthesis of Au hollow nanostructures *via* conformal deposition of Au and etching of Ag. I followed the protocols reported by Qin and co-workers with minor modifications [22]. An aqueous suspension of the Ag nanocrystals (0.02 mg in terms of Ag) was mixed with 2 mL of PVP-29k (29 mg/mL), 0.5 mL of NaOH (200 mM), 0.5 mL of AA (100 mM), and 15 μL of CTAC (200 mM) at room temperature. Afterwards, 0.5 mL of 0.1 mM $HAuCl_4$ was injected using a syringe pump at a rate of 0.02 mL/min. The reaction solution was stirred for another 5 min and then transferred into a centrifuge tube and centrifuged at 13,200 rpm for 15 min. The precipitates were incubated with 0.7 mL of 29 mg/mL PVP-29k, 0.3 mL of 100 mM AA, and 5 μL of 200 mM CTAC solution for 30 min. The particles were collected by centrifugation at 13,200 rpm for 15 min and then etched with 1 mL of 3% aqueous H_2O_2 at room temperature for 3 h. The final products

were collected *via* centrifugation at 16,000 rpm for 15 min and re-dispersed in H_2O for further characterization.

Characterization methods. Transmission electron microscope (TEM) images were taken on a Hitachi HT7700 microscope operated at 120 kV. The concentration of Ag seeds was determined using an inductively coupled plasma mass spectrometer (ICP-MS, NexION 300Q, PerkinElmer, Waltham, MA). All UV-vis spectra were recorded on a Cary 60 spectrometer (Agilent Technologies, Santa Clara, CA).

3.5 Notes to Chapter 3

Part of this chapter is adapted from the paper "Site-selective Growth of Ag Nanocubes for Sharpening Their Corners and Edges, Followed by Elongation into Nanobars Through Symmetry Reduction" published in the *Journal of Materials Chemistry C* [36].

3.6 References

(1) Rycenga, M.; Cobley, C. M.; Zeng, J.; Li, W.; Moran, C. H.; Zhang, Q.; Qin, D.; Xia, Y. *Chem. Rev.* **2011**, *111*, 3669–3712.

(2) Zhang, Q.; Li, W.; Moran, C.; Zeng, J.; Chen, J.; Wen, L.-P.; Xia, Y. *J. Am. Chem. Soc.* **2010**, *132*, 11372–11378.

(3) Cobley, C. M.; Skrabalak, S. E.; Campbell, D. J.; Xia, Y. *Plasmonics* **2009**, *4*, 171–179.

(4) McLellan, J. M.; Siekkinen, A.; Chen, J.; Xia, Y. *Chem. Phys. Lett.* **2006**, *427*, 122–126.

(5) Christopher, P.; Linic, S. *ChemCatChem* **2010**, *2*, 78–83.

(6) Zhou, S.; Li, J.; Gilroy, K. D.; Tao, J.; Zhu, C.; Yang, X.; Sun, X.; Xia, Y. *ACS Nano* **2016**, *10*, 9861–9870.

(7) Ruditskiy, A.; Xia, Y. *J. Am. Chem. Soc.* **2016**, *138*, 3161–3167.

(8) Siekkinen, A. R.; McLellan, J. M.; Chen, J.; Xia, Y. *Chem. Phys. Lett.* **2006**, *432*, 491–496.

(9) Im, S. H.; Lee, Y. T.; Wiley, B.; Xia, Y. *Angew. Chem. Int. Ed.* **2005**, *44*, 2192–2195.

(10) Skrabalak, S. E.; Wiley, B. J.; Kim, M.; Formo, E. V; Xia, Y. *Nano Lett.* **2008**, *8*, 2077–2081.

(11) Yang, M.; Gilroy, K. D.; Xia, Y. *Part. Part. Syst. Charact.* **2016**, DOI: 10.1002/ppsc.201600279.

(12) Ma, Y.; Li, W.; Cho, E. C.; Li, Z.; Yu, T.; Zeng, J.; Xie, Z.; Xia, Y. *ACS Nano* **2010**, *4*, 6725–6734.

(13) Lin, Z.-W.; Tsao, Y.-C.; Yang, M.-Y.; Huang, M. H. *Chem. - Eur. J.* **2016**, *22*, 2326–2332.

(14) Gong, J.; Zhou, F.; Li, Z.; Tang, Z. *Chem. Commun.* **2013**, *49*, 4379–4381.

(15) Zhu, C.; Zeng, J.; Tao, J.; Johnson, M. C.; Schmidt-Krey, I.; Blubaugh, L.; Zhu, Y.; Gu, Z.; Xia, Y. *J. Am. Chem. Soc.* **2012**, *134*, 15822–15831.

(16) Ma, Y.; Li, W.; Zeng, J.; McKiernan, M.; Xie, Z.; Xia, Y. *J. Mater. Chem.* **2010**, *20*, 3586–3589.

(17) Xie, S.; Peng, H.-C.; Lu, N.; Wang, J.; Kim, M. J.; Xie, Z.; Xia, Y. *J. Am. Chem. Soc.* **2013**, *135*, 16658–16667.

(18) Park, J.; Wang, H.; Vara, M.; Xia, Y. *ChemSusChem* **2016**, *9*, 2855–2861.

(19) Xie, S.; Lu, N.; Xie, Z.; Wang, J.; Kim, M. J.; Xia, Y. *Angew. Chem. Int. Ed.* **2012**, *51*, 10266–10270.

(20) Wiley, B. J.; Chen, Y.; McLellan, J. M.; Xiong, Y.; Li, Z.-Y.; Ginger, D.; Xia, Y. *Nano Lett.* **2007**, *7*, 1032–1036.

(21) Zhang, Q.; Moran, C. H.; Xia, X.; Rycenga, M.; Li, N.; Xia, Y. *Langmuir* **2012**, *28*, 9047–9054.

(22) Sun, X.; Kim, J.; Gilroy, K. D.; Liu, J.; König, T. A. F.; Qin, D. *ACS Nano* **2016**, *10*, 8019–8025.

(23) Wang, Y.; Zheng, Y.; Huang, C. Z.; Xia, Y. *J. Am. Chem. Soc.* **2013**, *135*, 1941–1951.

(24) Nikoobakht, B.; El-Sayed, M. A. *Langmuir* **2001**, *17*, 6368–6374.

(25) Smith, D. K.; Korgel, B. A. *Langmuir* **2008**, *24*, 644–649.

(26) Vansek, P. *"Electrochemical series." Handbook of Chemistry and Physics*. **1998**.

(27) Wu, F.; Wang, W.; Xu, Z.; Li, F. *Sci. Rep.* **2015**, *5*, 10772.

(28) Long, R.; Zhou, S.; Wiley, B. J.; Xiong, Y. *Chem. Soc. Rev.* **2014**, *43*, 6288–6310.

(29) Xiong, Y.; Cai, H.; Wiley, B. J.; Wang, J.; Kim, M. J.; Xia, Y. *J. Am. Chem. Soc.* **2007**, *129*, 3665–3675.

(30) Gilroy, K. D.; Peng, H.-C.; Yang, X.; Ruditskiy, A.; Xia, Y. *Chem. Commun.* **2017**, *53*, 4530-4541

(31) Xia, Y.; Li, W.; Cobley, C. M.; Chen, J.; Xia, X.; Zhang, Q.; Yang, M.; Cho, E. C.; Brown, P. K. *Acc. Chem. Res.* **2011**, *44*, 914–924.

(32) Yang, X.; Yang, M.; Pang, B.; Vara, M.; Xia, Y. *Chem. Rev.* **2015**, *115*, 10410–10488.

(33) Skrabalak, S. E.; Chen, J.; Sun, Y.; Lu, X.; Au, L.; Cobley, C. M.; Xia, Y. *Acc. Chem. Res.* **2008**, *41*, 1587–1595.

(34) Skrabalak, S. E.; Au, L.; Li, X.; Xia, Y. *Nat. Protoc.* **2007**, *2*, 2182–2190.

(35) Sun, Y.; Xia, Y. *Science.* **2002**, *298*, 2176–2179.

(36) Zhou, S.; Mesina, D. S.; Organt, M. A.; Yang, T.-H.; Yang, X.; Huo, D.; Zhao, M.; Xia, Y. *J. Mater. Chem. C* **2018**, *6*, 1384–1392.

CHAPTER 4

ENABLING COMPLETE LIGAND EXCHANGE ON THE SURFACE OF GOLD NANOCRYSTALS THROUGH THE DEPOSITION AND THEN ETCHING OF SILVER

4.1 Introduction

The surface properties of nanocrystals play a pivotal role in determining their performance in a wide variety of applications, including those related to catalysis, sensing, biomedicine, and self-assembly [1-6]. For the nanocrystals synthesized using a wet chemical approach, their surface is inevitably covered by capping agents and/or colloidal stabilizers, known as ligands, to help direct particle growth and prevent aggregation, respectively [7-9]. The ligands are, however, not necessarily benign or beneficial to the targeted applications. As a result, post-synthesis ligand exchange is often needed in order to put the desirable functional groups on the surface of nanocrystals and thus meet the requirements of various applications [2,4,10-18].

Direct ligand exchange has been the most commonly used method for replacing the chemical species on the surface of nanocrystals [2,17]. In this process, the nanocrystals covered by the original ligand are collected and washed through centrifugation and then dispersed in a solution containing the desired ligand. The solution is then shaken and incubated for a relatively long period of time to ensure a complete exchange of ligands. While this method is straightforward to conduct, its effectiveness is often questionable. The driving force for direct ligand exchange is mainly based on the binding competition

between the two ligands. Unless the second ligand binds more strongly than the first ligand toward the surface of the nanocrystals and is used in excess, it will be difficult to achieve complete replacement [19]. The direct exchange method also tends to fail when the two ligands involved carry opposite charges, which can cause the nanocrystals to aggregate during the exchange process.

Two-step protocols have also been reported as an alternative to direct ligand exchange [20,21]. For example, Wang *et al.* reported the use of acid treatment and sonication to remove the original ligand, followed by the deposition of the second ligand and thermal treatment, to tailor the surface chemistry of up-conversion nanocrystals [20]. This method has not been extended to other types of nanocrystals and it is not clear if sonication will cause changes to the nanocrystals. In another demonstration, Nann *et al.* used solvent extraction to remove the original ligand in the first step, but they were only able to partially remove the ligand to avoid aggregation for the nanocrystals [21]. As a result, the second step still relies on the direct exchange between the two ligands, facing the same challenges as the direct method.

Herein, I report an indirect ligand exchange method for effectively replacing various types of ligands on Au nanocrystals with sodium citrate (Na_3CA). We started with Au nanospheres capped by cetyltrimethylammonium chloride (CTAC), see Figure 4.1a, because cationic surfactants such as CTAC and cetyltrimethylammonium bromide (CTAB) have strong binding toward Au and they are commonly used in the shape-controlled synthesis of Au nanocrystals. [13]. Since CTAC binds more strongly toward Au relative to citrate and these two ligands carry opposite charges, the conventional one-step method simply does not work. My indirect ligand exchange method involves the deposition of a

thin layer of Ag to help desorb CTAC, followed by the selective etching of the Ag layer while introducing citrate ions to the surface of the nanopsheres. Using multiple characterization techniques, I confirmed that the surface of the Au nanocrystals is covered by citrate ions after the indirect ligand exchange process, and there is essentially no aggregation during the entire process. This method can be extended to Au nanocrystals with other morphologies and/or capped by different surface ligands. My colleague and I also demonstrated that this method was effective in suppressing the toxicity of Au nanospheres by completely replacing the initially used CTAC with citrate.

4.2 Results and Discussion

The scheme of this indirect ligand exchange process is shown in Figure 4.1a. The CTAC-capped Au nanospheres were prepared using seed-mediated growth as reported before [22]. Figure 4.1b shows a typical transmission electron microscopy (TEM) image of the as-prepared Au nanospheres with an average diameter of 50 nm. These Au nanospheres supported localized surface plasmon resonance (LSPR), with a peak around 530 nm (Figure 4.2). It is generally accepted that the cationic surfactant such as CTAC or CTAB takes a bilayer structure on the surface of Au nanocrystals, together with the adsorption of a counterion such as Cl^- or Br^- [2,23]. The CTAC-capped Au nanospheres had a zeta potential of 37.8 mV, indicating a strongly positive surface charge.

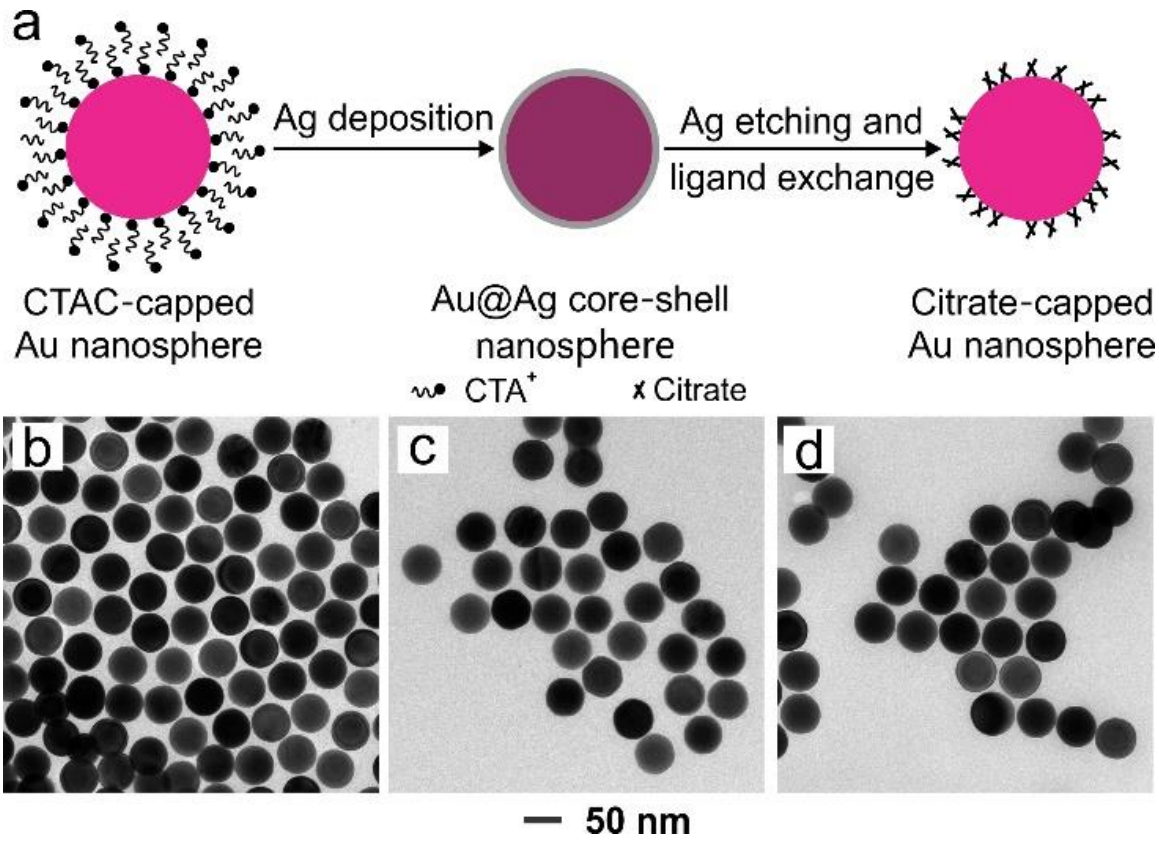

Figure 4.1. (a) Schematic illustration of ligand exchange on Au nanospheres as assisted by Ag deposition and etching. (b-d) TEM images of the CTAC-capped Au nanospheres, Au@Ag nanospheres, and citrate-capped Au nanospheres, respectively.

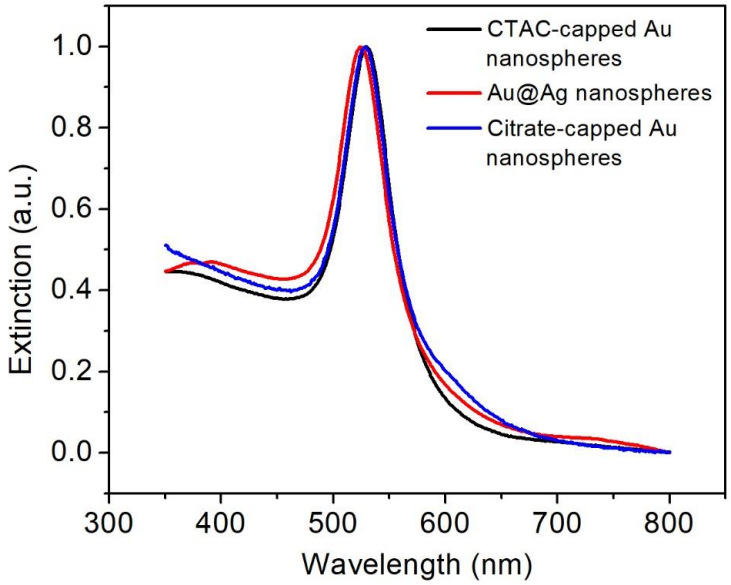

Figure 4.2. UV-vis spectra of Au nanospheres before and after the indirect ligand exchange process. Before the ligand exchange process, the CTAC-capped Au nanospheres showed a single LSPR peak at 530 nm. After Ag deposition, the main LSPR peak was blue-shifted to 525 nm. After ligand exchange with citrate, the position of the main LSPR peak was shifted to 529 nm.

In my initial attempt, I used direct ligand exchange to replace the CTAC with citrate. The color of the suspension turned from pink to purple within seconds (Figure 4.3a), and changed to colorless in about 10 min. Black aggregates were found in the solution and on the surface of the stirring bar at the end of the process. The aggregation was likely caused by the attenuation in electrostatic repulsion between the positively charged nanospheres when negatively charged citrate ions were introduced into the suspension.

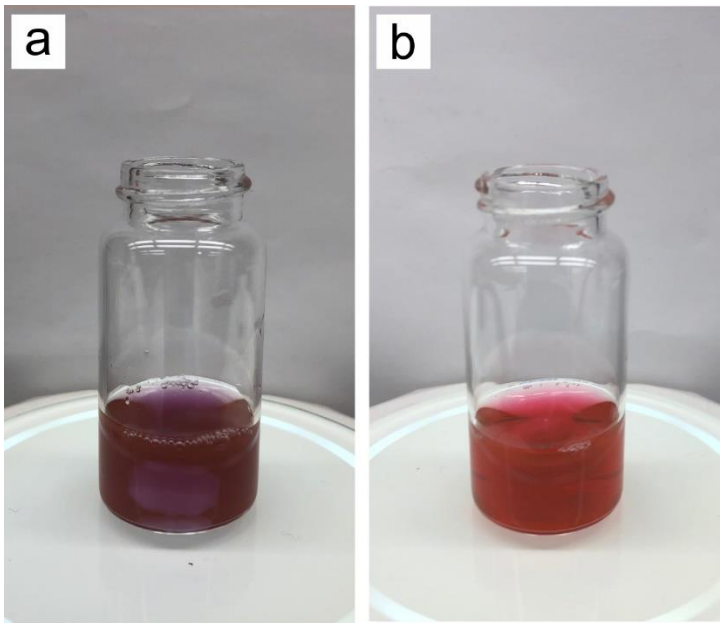

Figure 4.3. Photographs of the Au colloidal suspension obtained (a) by mixing the CTAC-capped Au nanospheres with Na_3CA for direct ligand exchange and (b) by depositing Ag on Au nanospheres using the indirect ligand exchange process. The color of Au colloidal suspension immediately changed from pink to purple when Au nanospheres were mixed with Na_3CA in the direct ligand exchange process. After 10 min, the solution turned to colorless with big black aggregates being observed in the solution and on the side of stirring bar. In contrast, the solution of Au nanospheres remained pink during Ag deposition and etching, suggesting that no major aggregation was involved in the Ag-mediated, indirect ligand exchange process.

To address the aggregation issue, I switched to indirect ligand exchange that involved the deposition of Ag in the presence of poly(vinylpyrrolidone) (PVP) and then selectively removal of the Ag by chemical etching in the presence of the second ligand (Figure 4.1a). In a typical process, an ultrathin layer of Ag was deposited on the CTAC-capped Au nanospheres in the presence of PVP at a relatively high concentration. The deposition relies on the fast reduction of $AgNO_3$ by a strong reducing agent such as ascorbic acid (AA) at room temperature. Most of the Au@Ag core-shell nanocrystals still maintained a spherical shape, with a very small portion appearing to have dimerized. The average thickness of the Ag layer was around 1.5 nm based on an inductively-coupled plasma mass spectrometry

(ICP-MS) analysis. It is worth mentioning that I chose PVP as a colloidal stabilizer because PVP is a neutral polymer that can prevent the nanocrystals from aggregation through the steric effect [24]. A blue-shift from 530 nm to 525 nm for the major LSPR peak confirms the deposition of Ag layer on the surface of the Au nanospheres (Figure 4.2).

After the deposition of Ag layer, Au@Ag nanospheres were collected using centrifugation, and then re-dispersed in aqueous H_2O_2 in the presence of Na_3CA to selectively remove the Ag layer. The solution was left undisturbed for 3 h and then the nanocrystals were collected by centrifugation and re-dispersed in aqueous Na_3CA solution for another 12 h. The resultant Au nanocrystals still displayed a spherical shape, with essentially no change to the morphology (Figure 4.1d). The main LSPR peak of the nanocrystals was located at 529 nm (Figure 4.2). Compared to the initial CTAC-capped Au nanospheres, the LSPR peak was blue-shifted by 1 nm, which can be attributed to the change in dielectric constant around the surface of the Au nanospheres. The ICP-MS measurement further confirmed that no detectable Ag was left behind in the final solid products.

After solving the aggregation problem, the surface chemistry of the Au nanospheres was further studied using various characterization techniques to confirm the completeness of ligand exchange. Since CTA^+, PVP, and citrate carry different charges, it is straightforward to use zeta potential measurement to qualitatively analyze changes to the surface charges on nanocrystals during the ligand exchange process (Table 4.1). As mentioned before, the CTAC-capped Au nanospheres had a zeta potential of 37.8 mV. After the deposition of Ag, the Au@Ag core-shell nanospheres showed a zeta potential of -12.7 mV. The slightly negative charge might originate from the adsorption of AA onto the

particle surface. Prior studies also suggested that PVP could exist with a slightly negative charge in water due to its resonance structure, contributing to a negative potential, despite that PVP is a neutral molecule [25]. After the selective etching and ligand exchange with citrate, the nanocrystals acquired a strongly negative charge of -33.3 mV. This value is comparable to what people have observed for Au nanocrystals directly synthesized with citrate as a stabilizer, albeit with no shape control [26]. In contrast, the direct ligand exchange method only gave Au nanospheres with a negative zeta potential of -6.8 mV in the presence of citrate (Table 4.2). I also tested a modified indirect ligand exchange method that involves no Ag deposition. This method also failed in achieving a large negative zeta potential (Table 4.2), indicating incomplete replacement of CTA^+ by citrate.

Table 4.1. Zeta potentials of the nanocrystals obtained during ligand exchange through Ag deposition and etching for the CTAC-capped Au nanospheres.

Nanocrystal	Zeta potential (mV)
CTAC-capped Au nanospheres	37.8
PVP-capped Au@Ag nanocrystals	-12.7
Citrate-capped Au nanospheres after Ag etching in H_2O_2 and re-dispersed in Na_3CA	-33.3

Table 4.2. Zeta potentials of nanocrystals obtained using the direct ligand exchange method and a modified, indirect ligand exchange method with no Ag deposition, respectively.

Nanocrystal	Zeta potential (mV)
Direct ligand exchange for the CTAC-capped Au nanospheres with Na_3CA	-6.8
Direct ligand exchange for the CTAC-capped Au nanospheres with PVP	8.2
Indirect ligand exchange with no Ag deposition	-30.9

The structural differences between the three stabilizers involved in the ligand exchange process offered an opportunity to use infrared (IR) spectroscopy to accurately analyze the surface species (Figure 4.4). I first recorded the reference spectra from pure CTAC, PVP, and Na_3CA. Because of the relatively long hydrocarbon chain, I observed strong double peaks from the symmetric and asymmetric stretching modes of the CH_2 group in the region of 2850-2950 cm^{-1} [27]. The characteristic peaks of PVP include the strong stretching modes of C=O (1650 cm^{-1}), C-N (1291 cm^{-1}), and the bending mode of CH_2 (1424 cm^{-1}) [24]. The stretching modes of the CH_2 group were also observed at low intensities, with no well-defined double peak feature. Citrate showed strong, doublet peaks in the region of 1400-1600 cm^{-1} due to the stretching modes of the carboxylic group [28,29]. After obtaining the reference spectra, I recoded IR spectra from all the nanocrystals collected during the ligand exchange process. As expected, the CTAC-capped Au nanospheres showed strong, doublet peaks from the stretching modes of CH_2 group in the region of 2850-2950 cm^{-1}. For the spectrum of the Au@Ag nanospheres, a peak with a much lower intensity was observed around 2900 cm^{-1} relative to the intensity of peaks in

the 1336-1700 cm^{-1}. This result suggests that most of the CTAC had been removed from the surface of Au nanocrystals during the deposition of Ag. Multiple peaks could be clearly identified in the region of 1336-1700 cm^{-1} with only slight shifts in peak positions relative to the reference spectra, which might be a result of the binding between PVP and Au nanocrystals. A new peak was also observed in this region at 1700 cm^{-1}. This peak might originate from the AA or dehydroascorbic acid adsorbed during the synthesis [30]. After the removal of Ag, the final Au nanospheres showed no peak at ~3000 cm^{-1}, with strong doublet peaks at 1580 cm^{-1} and 1396 cm^{-1} that corresponded to the asymmetric and symmetric stretching vibrations of the carboxylic group [29]. The lack of strong stretching vibrations of CH_2 suggests the absence of CTA^+ on the surface of the Au nanospheres after the Ag-assisted ligand exchange process. It is worth mentioning that the doublet peaks due to the stretching modes of CH_2 group in CTAC were still observed in the IR spectrum (Figure 4.5) when using the modified indirect method that involved no Ag deposition, suggesting the importance of Ag deposition in replacing the CTAC completely.

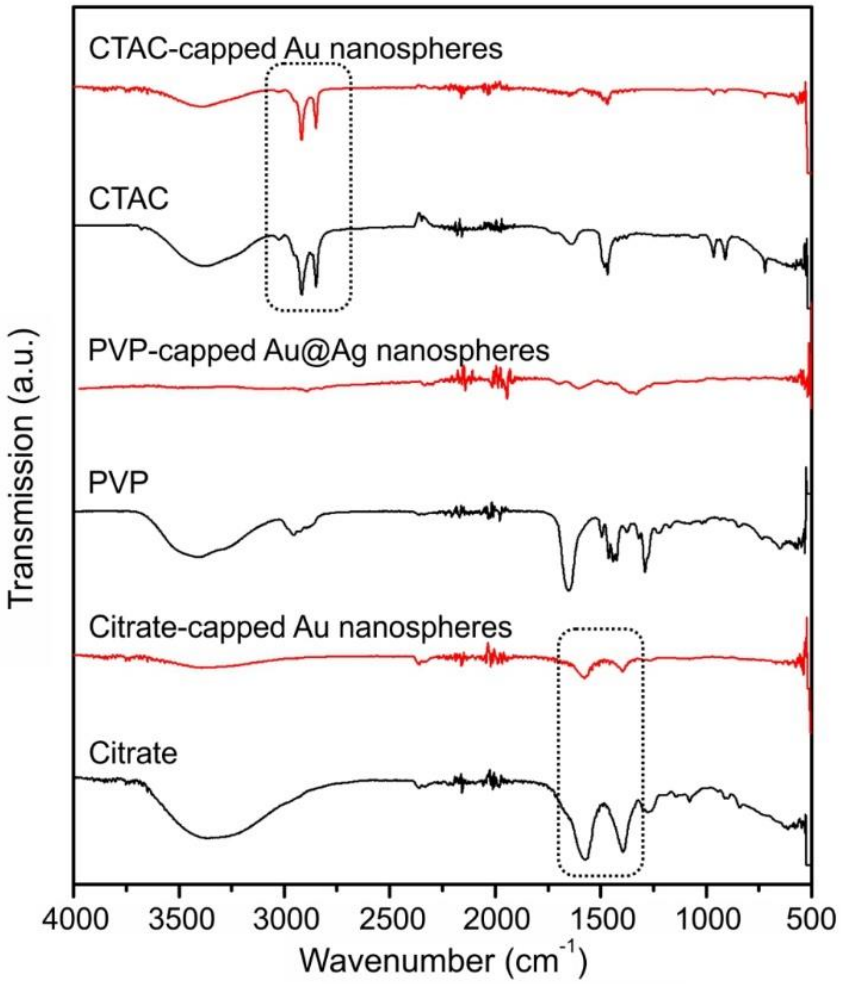

Figure 4.4. Fourier transform IR spectra of the Au nanospheres capped with different ligands and the reference spectra of the pure ligands. The stretching modes of the CH_2 group in CTAC and the carboxylic group in citrate are highlight by the boxes.

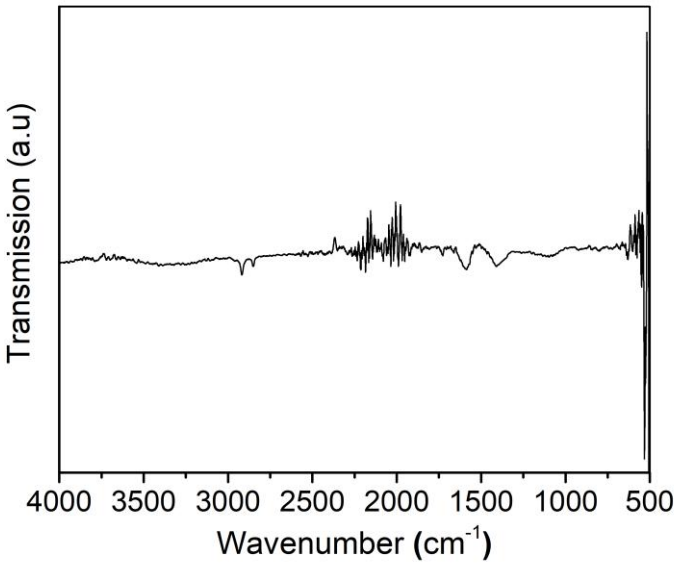

Figure 4.5. Fourier transform IR spectrum of Au nanospheres after the modified indirect ligand exchange process involving no Ag deposition. The Au nanospheres showed two strong peaks in the region of 2850-2950 cm^{-1}, which correspond to the asymmetric stretching mode (2918 cm^{-1}) and symmetric stretching mode (2850 cm^{-1}) of CH_2 group, respectively. This result shows the presence of CTAC after the modified indirect ligand exchange process and suggests that Ag deposition is necessary to completely remove CTAC from the surface of Au nanospheres.

Since both the PVP- and citrate-capped nanocrystals showed similar IR peaks close to 1600 cm^{-1} and negative surface charges, it was unclear if any PVP was left behind on the surface of the Au nanospheres solely based on the zeta potential and IR measurements. In this regard, I used X-ray photoelectron spectroscopy (XPS) to measure the relative intensities of Au, Ag, N, and Cl for each type of nanocrystals to further verify that the final Au nanospheres were essentially capped by citrate. As can be seen from Figure 4.6, strong Au(0) peaks were observed for the CTAC-capped Au nanospheres, along with clear N and Cl peaks. The presence of N and Cl^- proves the presence of CTAC, which has the $[(C_{16}H_{33})N(CH_3)_3]^+$ moiety and the Cl^- counter ion. For the Au@Ag core-shell nanocrystals, the intensity of Au(0) decreased while the intensity of Ag(0) increased. The

N peak still existed, but the peak position shifted to a lower binding energy due to the fact that the N atoms are neutral in PVP instead of being positively charged as in CTAC. The intensity of Cl^- also decreased significantly, suggesting the reduced presence of CTAC. After etching and ligand exchange with citrate ions, no N or Cl^- peaks were observed, indicating the absence of both CTAC and PVP from the surface of the final Au nanospheres. The absence of Ag peak also indicates the complete removal of the Ag layer and rules out the possibility of forming a Ag-Au alloy on the Au nanocrystals.

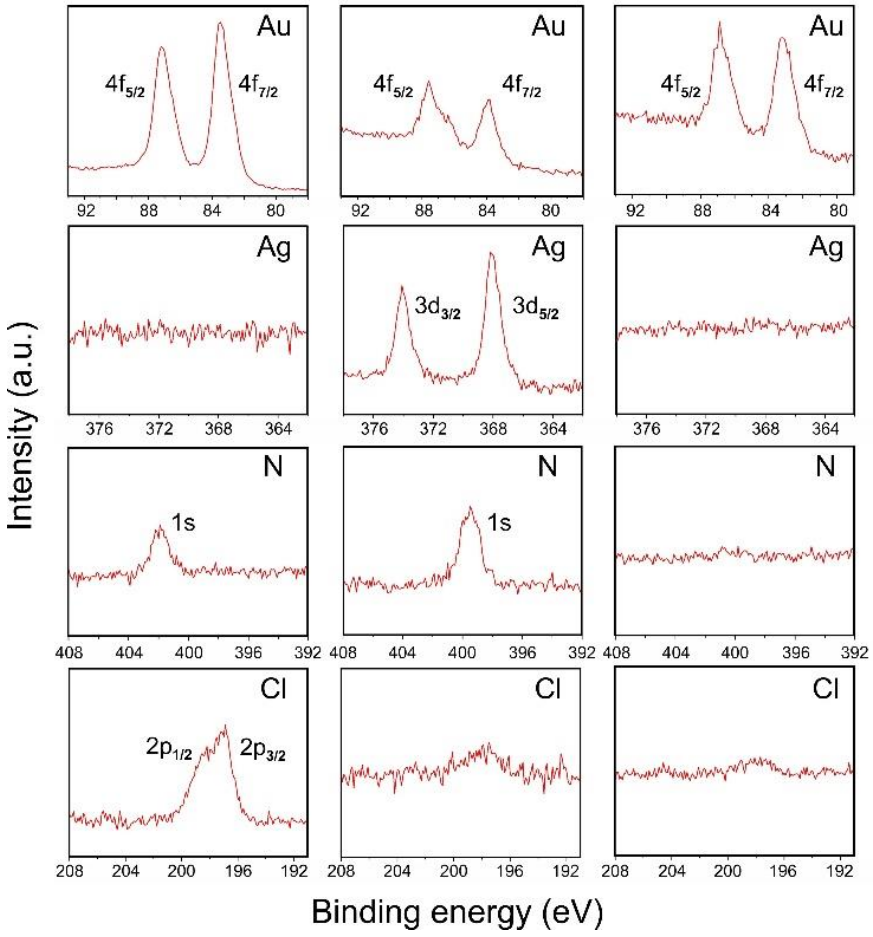

Figure 4.6. XPS characterizations of the CTAC-capped Au nanospheres (left panel), PVP-capped Au@Ag nanospheres (middle panel), and citrate-capped Au nanospheres (right panel).

I also demonstrated that the indirect ligand exchange method was effective in achieving complete ligand exchange on Au nanocrystals with other morphologies, including rhombic dodecahedrons capped by PVP, trisoctahedrons capped by CTAC, and nanorods capped by CTAB (Figure 4.7-4.10). Before the ligand exchange process, the zeta potentials of the rhombic dodecahedrons, trisoctahedrons and nanorods were -11.6, 50.3, and 60.8 mV, respectively. Their zeta potentials changed to -36.4, -38.4, and -29.3 mV, respectively, after introducing citrate ions to the surface using the indirect ligand exchange method. The slightly smaller negative value on nanorods might be due to the fact that Ag was present in the Au nanorods, and citrate ions bind to Ag weaker than Au [34,35]. After the ligand exchange, no peaks were observed for the CH_2 group in the region of 2850-2950 cm^{-1}, indicating the absence of PVP or CTAC on the surface of Au nanocrystals. The ICP-MS measurements showed that no Ag was detected after the ligand exchange process for Au rhombic dodecahedrons and trisoctahedrons. The CTAB-capped Au nanorods had a Ag content (~7.3 %) from the synthesis, and the percentage did not increase after the ligand exchange process (~6.1 %). As the control group, we carried out modified indirect ligand exchange method that involves no Ag deposition for these three types of Au nanocrystals. The zeta potentials for Au rhombic dodecahedrons, trisoctahedrons and nanorods after ligand exchange were -29.6, -21.6, and -19.2 mV, respectively, showing that Ag deposition was necessary to achieve a complete replacement of surface ligands. All these results prove that the indirect ligand exchange method can be extended to Au nanocrystals with various morphologies capped by different capping agents.

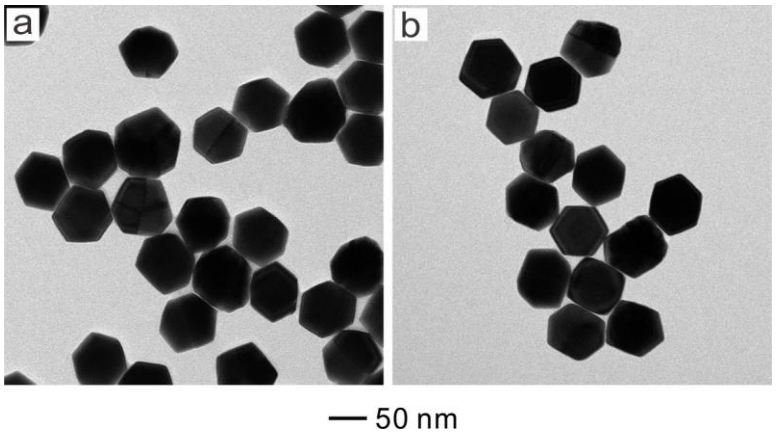

Figure 4.7. TEM images of Au rhombic dodecahedrons (a) before and (b) after the indirect ligand exchange process to replace the original PVP ligands with citrate ions.

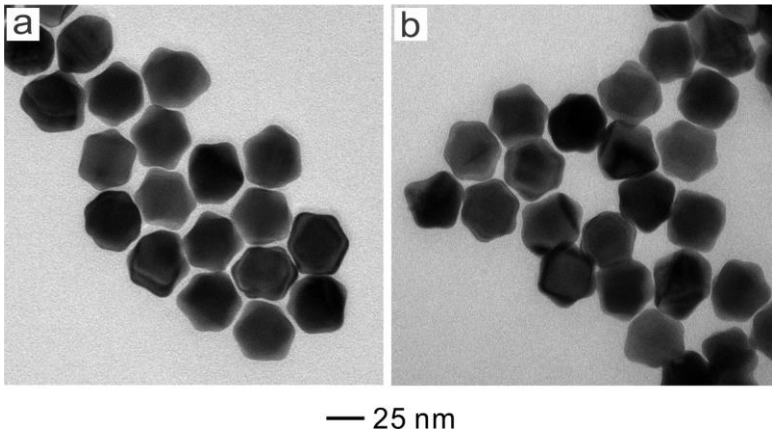

Figure 4.8. TEM images of Au trisoctahedrons (a) before and (b) after the indirect ligand exchange process to replace the original CTAC ligand with citrate ions.

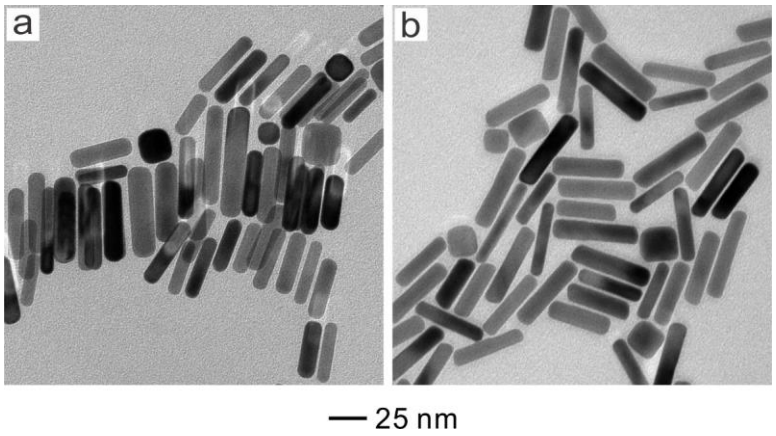

Figure 4.9. TEM images of Au nanorods (a) before and (b) after the indirect ligand exchange process to replace the original CTAB ligand with citrate ions.

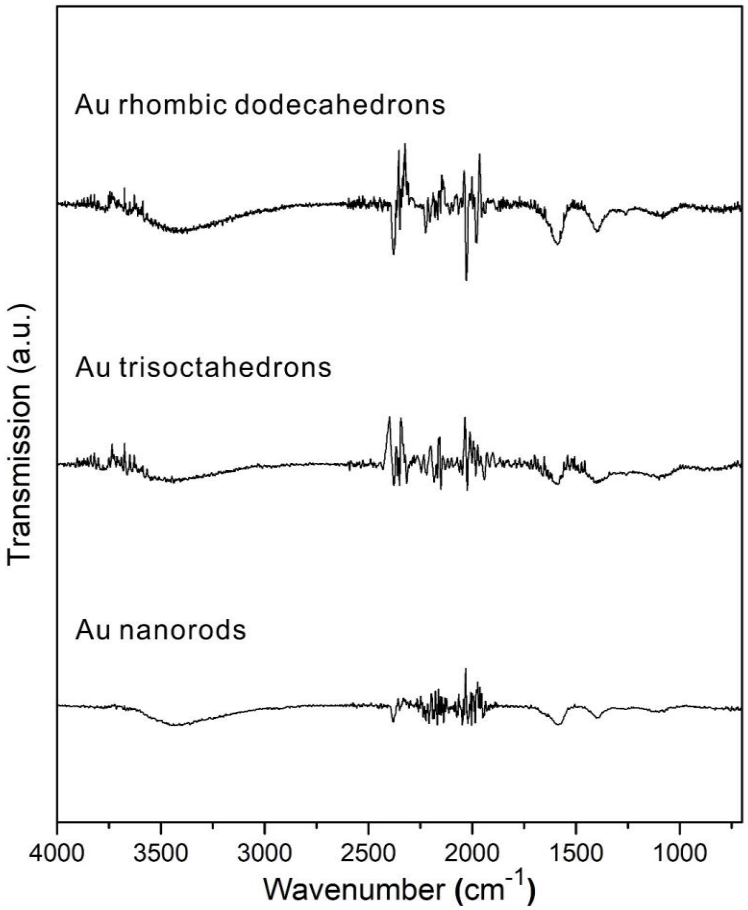

Figure 4.10. Fourier transform IR spectra of Au rhombic dodecahedrons, trisoctahedrons and nanorods after the indirect ligand exchange process to replace the original surface ligands with citrate ions. No peaks were observed for the CH_2 group in the region of 2850-2950 cm^{-1}, indicating the absence of PVP or CTAC on the surface of Au nanocrystals.

In addition to Ag, I also tested the feasibility of using Cu and Au deposition for the indirect ligand exchange process (Figure 4.11). No deposition of Cu could be identified from the TEM image (Figure 4.11a), indicating the inadequate reducing power of AA to reduce $CuCl_2$ in this system. The result was also confirmed by the ICP-MS measurement. Small Au nanocrystals were formed on the surface of the original Au nanospheres (Figure 4.11b). The newly reduced Au atoms did not form a uniform layer on the surface of the Au nanospheres, thus failed in maintaining the original shape of the nanospheres. The different behaviors in the deposition of Au and Cu as compared to that of Ag could be attributed to the different reduction potentials of their salt precursors. These results show that Ag deposition is irreplaceable in the indirect ligand exchange process.

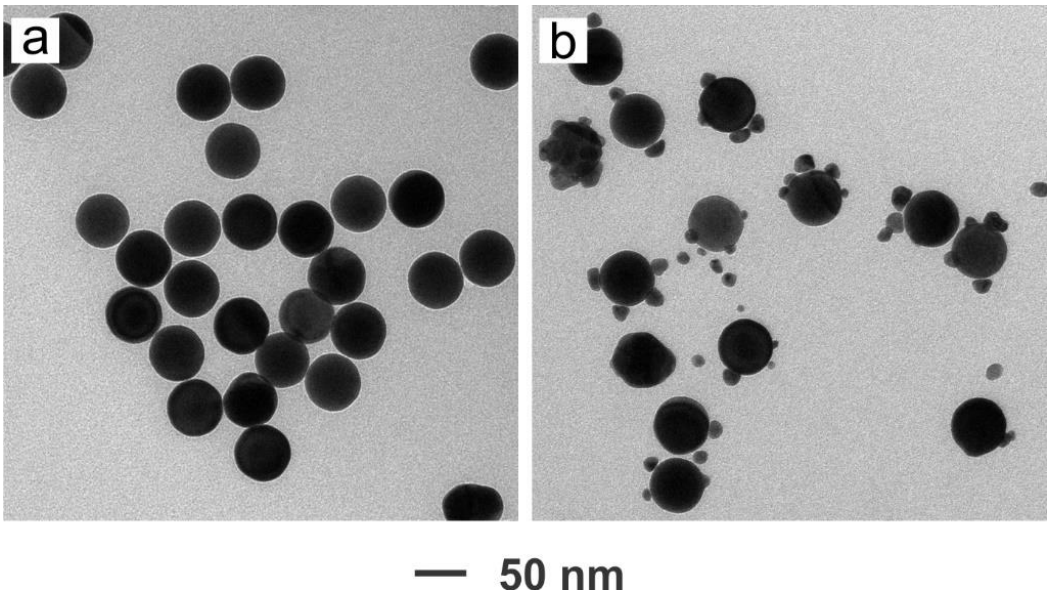

Figure 4.11. TEM images of nanocrystals obtained from metal deposition using (a) $CuCl_2$, and (b) $HAuCl_4$ instead of $AgNO_3$ as the metal precursor. All the other parameters were kept the same as the Ag deposition process.

My colleague and I further investigated how the surface ligands on Au nanospheres influence their toxicity toward both normal mouse fibroblast cell line (NIH-3T3) and

cancerous human cervical cell line (HeLa) through flow-cytometry analysis. The toxicity of CTAC-capped Au nanospheres was concentration-dependent regardless of cell line (Figure 4.12a). When the concentration of Au was increased from 20 to 250 μg/mL, the viability of NIH-3T3 cells decreased from 92.3% to 34.7%, and the viability of HeLa cells showed a similar trend from 94.5% to 42.1%. In contrast, when the capping agent was switched to citrate, I noticed that the toxicity of Au nanospheres was largely mitigated (Figure 4.12b). Even in the presence of 250 μg/mL citrate-capped Au nanospheres, the viability of NIH-3T3 and HeLa cells only slightly decreased to 88.7% and 91.9%, respectively. These data validated that the indirect ligand exchange method could effectively suppress the toxicity of Au nanospheres by completely replacing the toxic ligand on the surface, which is appealing for potential biomedical applications.

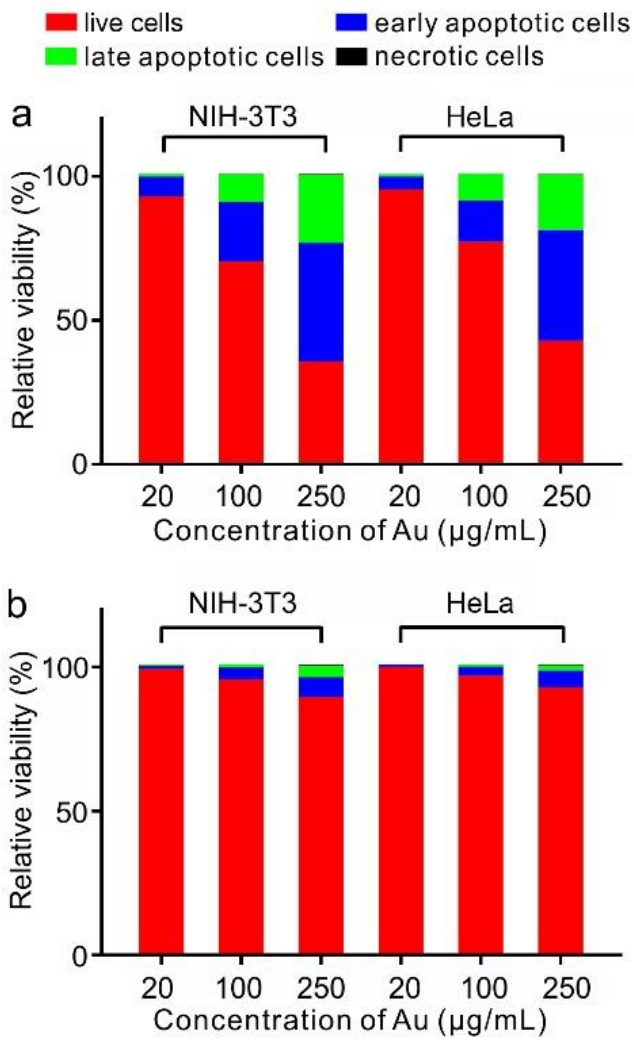

Figure 4.12. Flow-cytometry analysis of NIH-3T3 and HeLa cells co-stained with fluorescein isothiocyanate-labeled annexin V (Annexin V-FITC) and propidium iodide (PI). The cells were incubated with the (a) CTAC-capped and (b) citrate-capped Au nanospheres, respectively, at different concentrations (20-250 μg/mL). It should be pointed out that the proportion of necrotic cells was too low to be displayed in the plots (< 0.4%).

4.3 Conclusion

In summary, I have demonstrated an indirect ligand exchange method for replacing the ligands on Au nanocrystals. The method involves the deposition of an ultrathin layer of Ag to help deport a strong capping agent such as CTAC from the surface of the Au nanocrystals. Subsequently, selective etching of the Ag layer allows me to introduce citrate

ions onto the surface of the nanocrystals. The complete ligand replacement was confirmed by multiple characterization techniques. Different from the conventional direct ligand exchange, this indirect method offers a facile and quick means to completely replace a strong ligand with an oppositely charged, weak ligand, and provides opportunities to modify nanoparticles with bio-benign surface groups for various applications.

4.4 Experimental Section

Chemicals and materials. Silver nitrate ($AgNO_3$, ≥99.0%), poly(vinylpyrrolidone) (PVP, MW≈55,000), cetyltrimethylammonium chloride (CTAC, 25 wt% in H_2O), ascorbic acid (AA, ≥99.0%), cetyltrimethylammonium bromide (CTAB, ≥99.0%), gold(III) chloride trihydrate ($HAuCl_4 \cdot 3H_2O$, ≥99.9%), sodium borohydride ($NaBH_4$, 98%), copper(II) chloride dihydrate ($CuCl_2 \cdot 2H_2O$, ≥99.0%), ethylenediaminetetraacetic acid disodium salt dehydrate (EDTA-2Na, 98%), aqueous solution of hydrochloric acid (HCl, 37%), Dimethylformamide (DMF, 99.8%), and hydrogen peroxide (H_2O_2, 30 wt % in H_2O) were all obtained from Sigma-Aldrich. Dulbecco's Modified Eagle Medium (DMEM), RPMI-1640 (1640), phosphate buffered saline (PBS, pH~7.2), penicillin/streptomycin, and fetal bovine serum (FBS) were obtained from Invitrogen (Thermo Fisher Scientific). All chemicals were used as received. Deionized (DI) water with a resistivity of 18.2 MΩ·cm at room temperature was used throughout the experiments.

Synthesis of CTAC-capped Au nanospheres. The synthesis was based on my previously reported seed-mediated growth [22]. The Au clusters were synthesized in the presence of CTAB, and then used as seeds to obtain 10-nm Au nanospheres in the presence of CTAC. The final CTAC-capped Au nanospheres with an average size of 50 nm were

synthesized using the 10-nm Au nanospheres as seeds. The products were collected by centrifugation at a speed of 9000 rpm for 5 min, washed with H_2O one time, and then re-dispersed in H_2O (0.59 mg/mL in terms of Au) for further use.

Synthesis of PVP-capped Au rhombic dodecahedrons. The synthesis was based on a previously reported seed-mediated growth [31]. A solution of 10-nm Au nanospheres were mixed with sodium citrate, $HAuCl_4$, and PVP in a water/DMF mixture, and heated at 70 ^oC for 3 h. The products were collected by centrifugation at a speed of 12000 rpm for 5 min, washed with H_2O one time, and then re-dispersed in H_2O (0.59 mg/mL in terms of Au) for further use.

Synthesis of CTAC-capped Au trisoctahedrons. The synthesis was based on our previously reported seed-mediated growth [32]. A EDTA-chelated Au(III) precursor was freshly made by chelating HAuCl4 with equal molar amount of EDTA-2Na, and then added into an aqueous solution of CTAC and AA. The 10-nm Au nanospheres were then injected into the mixture, and the reaction was allowed to proceed on the orbital shaker for 20 min at room temperature. The products were collected by centrifugation at a speed of 12000 rpm for 5 min, washed with H_2O one time, and then re-dispersed in H_2O (0.59 mg/mL in terms of Au) for further use.

Synthesis of CTAB-capped Au nanorods. The synthesis was based on a previously reported seed-mediated growth [33]. The Au clusters were synthesized in the presence of CTAB, and added into a mixture of $HAuCl_4$, $AgNO_3$, CTAB, HCl and AA to grow the Au nanorods. The reaction was allowed at room temperature for 6 h. The products were collected by centrifugation at a speed of 12000 rpm for 5 min, washed with H_2O one time,

washed with 112 mM PVP solution one time, and then re-dispersed in water (0.59 mg/mL in terms of Au) for further use.

Direct ligand exchange on CTAC-capped Au nanospheres. For the direct ligand exchange on CTAC-capped Au nanospheres, 1 mL of the as-synthesized CTAC-capped Au nanospheres were added into an aqueous solution of Na_3CA (4.2 mM, 4.8 mL). The solution was then stirred for 10 min at room temperature.

Synthesis of Au@Ag core-shell nanospheres. In a standard synthesis, 4.8 mL of aqueous PVP (47 mM), 1.0 mL of the CTAC-capped Au nanospheres, and 0.1 mL of aqueous AA (40 mM) were added into a 20-mL glass vial and mixed at room temperature. Then 1.0 mL of aqueous $AgNO_3$ (0.3mM) was injected in one shot using a pipette. The reaction solution was stirred for another 10 min to make sure the complete reduction of Ag precursor. Acetone was added into the reaction solution at a 2:1 ratio and the particles were collected using centrifugation at 9,000 rpm for 5 min and then re-dispersed in 200 μL of 10 mM Na_3CA solution. The freshly made suspension was used immediately for etching.

Synthesis of citrate-capped Au nanospheres. In a standard synthesis, 200 μL of Au@Ag nanospheres were etched with 0.9 mL of 3% H_2O_2 at room temperature for 3h. The particles were collected by centrifugation at 12,000 rpm for 10 min, and then re-dispersed in 100 μL of Na_3CA solution (10 mM). The particles were kept at room temperature for 12 h, then 900 μL of H_2O was added, followed by the centrifugation at 9,000 rpm for 5 min and re-dispersed in 1 mL of H_2O.

Cell culture. Human cervical carcinoma cell line (HeLa) and mouse fibroblast cell line (NIH-3T3) were obtained from American Type Culture Collection (ATCC). They

were both cultured and maintained in the growth medium of DMEM supplemented with 10% FBS and 1% penicillin/streptomycin. Cultures were maintained in an incubator at 37 ^{o}C in a humidified atmosphere of 5% CO_2. The medium was replaced every other day until a ca. 90% confluency has been reached.

Flow-cytometry analysis. Both HeLa and NIH-3T3 cells were seeded in 6-well plates in a density of 2×10^5 cells per well, and cultured until a ca. 85% confluency were reached. Afterwards, the culture medium was discarded, and 1 mL fresh DMEM medium (no serum) containing either CTAC-capped or CA-capped Au nanocrystals were added into each well. The cells were washed thoroughly with warm PBS at 24 h post incubation with Au nanocrystals, followed by co-staining with Annexin V-FITC and PI (Apoptosis Detection Kit, BD Bioscience) according to manufacturer's instructions to label live (Annexin V-FITC (-)/PI (-)), early apoptotic (Annexin V-FITC (+)/PI (-)), late apoptotic (Annexin V-FITC (+)/PI (+)), and necrotic ((Annexin V-FITC (-)/PI (+)) cells. The profiles of apoptosis were analyzed by flow-cytometry (LSR II, BD Bioscience), and the raw FACS data were processed by FlowJo (version 7.6.1.).

Characterization methods. Transmission electron microscope (TEM) images were taken on a Hitachi HT7700 microscope operated at 120 kV. Zeta potential measurements were determined using a Zetasizer Nano ZS (Malvern Instruments, Worcestershire, UK). The concentrations of Au and Ag were determined using an inductively coupled plasma mass spectrometer (ICP-MS, NexION 300Q, PerkinElmer, Waltham, MA). All UV-vis spectra were recorded on a Cary 60 spectrometer (Agilent Technologies, Santa Clara, CA). All IR spectra were recorded on a Varian 640 IR spectrometer (Agilent Technologies,

Santa Clara, CA). The XPS data was recorded using a Thermo K-Alpha spectrometer with an Al Kα source (eV).

4.5 Notes to Chapter 4

Part of this chapter is adapted from the paper "Enabling Complete Ligand Exchange on the Surface of Gold Nanocrystals through the Deposition and then Etching of Silver", recently submitted for publication.

4.6 References

(1) Krause, M. M.; Kambhampati, P. *Phys. Chem. Chem. Phys.* **2015**, *17*, 18882–18894.

(2) Burrows, N. D.; Lin, W.; Hinman, J. G.; Dennison, J. M.; Vartanian, A. M.; Abadeer, N. S.; Grzincic, E. M.; Jacob, L. M.; Li, J.; Murphy, C. J. *Langmuir* **2016**, *32*, 9905–9921.

(3) Taguchi, T.; Isozaki, K.; Miki, K. *Adv. Mater.* **2012**, *24*, 6462–6467.

(4) Hu, P.; Chen, L.; Kang, X.; Chen, S. *Acc. Chem. Res.* **2016**, *49*, 2251–2260.

(5) Mout, R.; Moyano, D. F.; Rana, S.; Rotello, V. M. *Chem. Soc. Rev.* **2012**, *41*, 2539-2544.

(6) Merg, A. D.; Zhou, Y.; Smith, A. M.; Millstone, J. E.; Rosi, N. L. *ChemNanoMat* **2017**, *3*, 745–749.

(7) Niu, Z.; Li, Y. *Chem. Mater.* **2014**, *26*, 72–83.

(8) Ortiz, N.; Skrabalak, S. E. *Langmuir* **2014**, *30*, 6649–6659.

(9) Xia, Y.; Xiong, Y.; Lim, B.; Skrabalak, S. E. *Angew. Chem. Int. Ed.* **2009**, *48*, 60–103.

(10) Abdelhameed, M.; Martir, D. R.; Chen, S.; Xu, W. Z.; Oyeneye, O. O.; Chakrabarti, S.; Zysman-Colman, E.; Charpentier, P. A. *Sci. Rep.* **2018**, *8*, 3050.

(11) Gao, J.; Gu, H.; Xu, B. *Acc. Chem. Res.* **2009**, *42*, 1097–1107.

(12) Zhou, J.; Ralston, J.; Sedev, R.; Beattie, D. J. *Colloid Interface Sci.* **2009**, *331*, 251–262.

(13) Yang, X.; Yang, M.; Pang, B.; Vara, M.; Xia, Y. *Chem. Rev.* **2015**, *115*, 10410-10488.

(14) Oh, N.; Park, J.-H. *ACS Nano* **2014**, *8*, 6232–6241.

(15) Tan, S. J.; Jana, N. R.; Gao, S.; Patra, P. K.; Ying, J. Y. *Chem. Mater.* **2010**, *22*, 2239–2247.

(16) Pelaz, B.; del Pino, P.; Maffre, P.; Hartmann, R.; Gallego, M.; Rivera-Fernández, S.; de la Fuente, J. M.; Nienhaus, G. U.; Parak, W. J. *ACS Nano* **2015**, *9*, 6996–7008.

(17) Xia, X.; Yang, M.; Wang, Y.; Zheng, Y.; Li, Q.; Chen, J.; Xia, Y. *ACS Nano* **2012**, *6*, 512–522.

(18) Sekiguchi, S.; Niikura, K.; Matsuo, Y.; Ijiro, K. *Langmuir* **2012**, *28*, 5503–5507.

(19) Zhang, S.; Kim, S.; Tsukruk, V. V. *Langmuir* **2017**, *33*, 3576–3587.

(20) Kong, W.; Sun, T.; Chen, B.; Chen, X.; Ai, F.; Zhu, X.; Li, M.; Zhang, W.; Zhu, G.; Wang, F. *Inorg. Chem.* **2017**, *56*, 872–877.

(21) Dewi, M. R.; Laufersky, G.; Nann, T. *RSC Adv.* **2014**, *4*, 34217–34220.

(22) Zheng, Y.; Zhong, X.; Li, Z.; Xia, Y. *Part. Part. Syst. Charact.* **2014**, *31*, 266–273.

(23) Angelomé, P. C.; Mezerji, H. H.; Goris, B.; Pastoriza-Santos, I.; Pérez-Juste, J.; Bals, S.; Liz-Marzán, L. M. *Chem. Mater.* **2012**, *24*, 1393–1399.

(24) Koczkur, K. M.; Mourdikoudis, S.; Polavarapu, L.; Skra-balak, S. E. *Dalt. Trans.* **2015**, *44*, 17883–17905.

(25) Badoga, S.; Pattanayek, S. K.; Kumar, A.; Pandey, L. M. *Asia-Pacific J. Chem. Eng.* **2011**, *6*, 78–84.

(26) Alkilany, A. M.; Abulateefeh, S. R.; Mills, K. K.; Bani Yaseen, A. I.; Hamaly, M. A.; Alkhatib, H. S.; Aiedeh, K. M.; Stone, J. W. *Langmuir* **2014**, *30*, 13799–13808.

(27) Cao, Q.; Zhao, H.; He, Y.; Li, X.; Zeng, L.; Ding, N.; Wang, J.; Yang, J.; Wang, G. *Biosens. Bioelectron.* **2010**, *25*, 2680–2685.

(28) Wulandari, P.; Nagahiro, T.; Fukada, N.; Kimura, Y.; Ni-wano, M.; Tamada, K. *J. Colloid Interface Sci.* **2015**, *438*, 244–248.

(29) Ranoszek-Soliwoda, K.; Tomaszewska, E.; Socha, E.; Krzyczmonik, P.; Ignaczak, A.; Orlowski, P.; Krzyzowska, M.; Celi-chowski, G.; Grobelny, J. *J. Nanocrystal Res.* **2017**, *19*, 273.

(30) Xiong, J.; Wang, Y.; Xue, Q.; Wu, X. *Green Chem.* **2011**, *13*, 900-904.

(31) Choi, K. W.; Kim, D. Y.; Zhong, X.-L.; Li, Z.-Y.; Im, S. H.; Park, O. O. *CrystEngComm.* **2013**, *15*, 252–258.

(32) Huo, D.; Ding, H.; Zhou, S.; Li, J.; Tao, J.; Ma, Y.; Xia, Y. *Nanoscale* **2018**, *10*, 11034–11042.

(33) Nikkobakht, B.; El-Sayed, M. A. *Chem. Mater.* **2003**, *15*, 1957-1962.

(34) Al-Johani, H.; Abou-Hamad, E.; Jedidi, A.; Widdifield, C. M.; Viger-Gravel, J.; Sangaru, S. S.; Gajan, D.; Anjum, D. H.; Ould-Chikh, S.; Hedhili, M. N.; Gurinov, A.; Kelly, M. J.; Eter, M. E.; Cavallo, L.; Emsley, L.; Basset, J.-M. *Nat. Chem.* **2017**, *9*, 890–895.

(35) Kilin, D. S.; Prezhdo, O. V.; Xia, Y. *Chem. Phys. Lett.* **2008**, *458*, 113–116.

CHAPTER 5

QUANTITATIVE ANALYSIS OF THE REDUCTION KINETICS INVOLVED IN THE SYNTHESIS OF PLATINUM NANOCRYSTALS

5.1 Introduction

Noble-metal nanocrystals have received ever increasing interests owing to their applications in catalysis, photonics, electronics, sensing, and medicine [1-3]. Platinum (Pt) nanocrystals, in particular, are among the best choice of catalytic materials toward a number of reactions, including oxygen reduction and (de)hydrogenation [4-7]. Many research efforts have been devoted to improving the catalytic performance of Pt nanocrystals by controlling their surface structure or morphology [8-10]. Thanks to the progress over the last two decades, it is now possible to design and rationally produce Pt nanocrystals with diversified shapes using either one-pot synthesis or seed-mediated growth [8,9]. However, my current understanding of the nucleation and growth of Pt nanocrystals is mainly derived from qualitative observations and it remains unsolved how the Pt(II) or Pt(IV) precursor is reduced in a typical synthesis [11]. To achieve a better control over the synthesis, it is of critical importance to elucidate the correlation between the outcome of a synthesis and the reduction kinetics involved [11].

Herein, I report a quantitative analysis of how a Pt(II) precursor is reduced to atoms at different temperatures for the formation of Pt nanocrystals with different morphologies and sizes. My results suggest that in the early stage of a synthesis, the Pt(II) precursor is reduced to atoms exclusively in the solution phase, followed by homogeneous nucleation

to generate nuclei and then seeds. At a relatively low reaction temperature such as 22 ^{o}C, the growth of the seeds is dominated by autocatalytic, surface reduction that involves the adsorption and then reduction of the Pt(II) precursor on the surface of the just-formed seeds. This particular growth pathway results in relatively large assemblies of Pt nanocrystals. When the reaction temperature is increased to 100 ^{o}C, the dominant reduction pathway will be switched from surface to solution phase, producing much smaller assemblies of Pt nanocrystals. My results also demonstrate that a similar trend applies to the seed-mediated growth of Pt nanocrystals in the presence of Pd nanocubes.

5.2 Results and Discussion

The synthesis of Pt nanocrystals in my study involves the mixing of $PtCl_4^{2-}$ with ascorbic acid (AA, reducing agent) and poly(vinylpyrrolidone) (PVP, colloidal stabilizer) in an aqueous solution held at a temperature in the range of 22−100 °C. Figure 5.1a, b shows transmission electron microscopy (TEM) images of the products obtained at 22 and 100 °C, respectively, in the absence of pre-formed seeds. The products obtained at 22 °C consisted of assemblies (with an average size of 31.8 nm) of small Pt nanocrystals that had an average size of about 2.5 nm. In contrast, the small Pt nanocrystals (also about 2.5 nm in size) formed at 100 °C tended to form assemblies with a smaller size of 17.4 nm. When pre-formed Pd nanocubes were introduced into the reaction system to serve as seeds, the small Pt nanocrystals were formed exclusively on the surface of the seeds at 22 °C (Figure 5.1c). The Pd-Pt nanocrystals had an average size of 33.9 nm, which is similar to the size of the assemblies of Pt nanocrystals obtained in the absence of pre-formed seeds. This is reasonable considering the relatively high amount of Pt(II) precursor (0.0102 mmol) used for seed-mediated growth compared to the amount of Pd seeds (0.0034 mmol). As such,

the volume occupied by the Pd seeds can be more or less neglected. When the reaction temperature was raised to 100 °C, however, the small Pt nanocrystals were observed to assemble both in the solution phase and on the surface of the seeds (Figure 5.1d). The assemblies of Pt nanocrystals in the solution phase had a much smaller size compared to the assemblies obtained in the absence of pre-formed seeds (Figure 5.1b). This can be attributed to the fact that some Pt atoms were deposited on the surface of the Pd nanocubes when pre-formed seeds were introduced, resulting in a smaller number of Pt for the formation of assemblies.

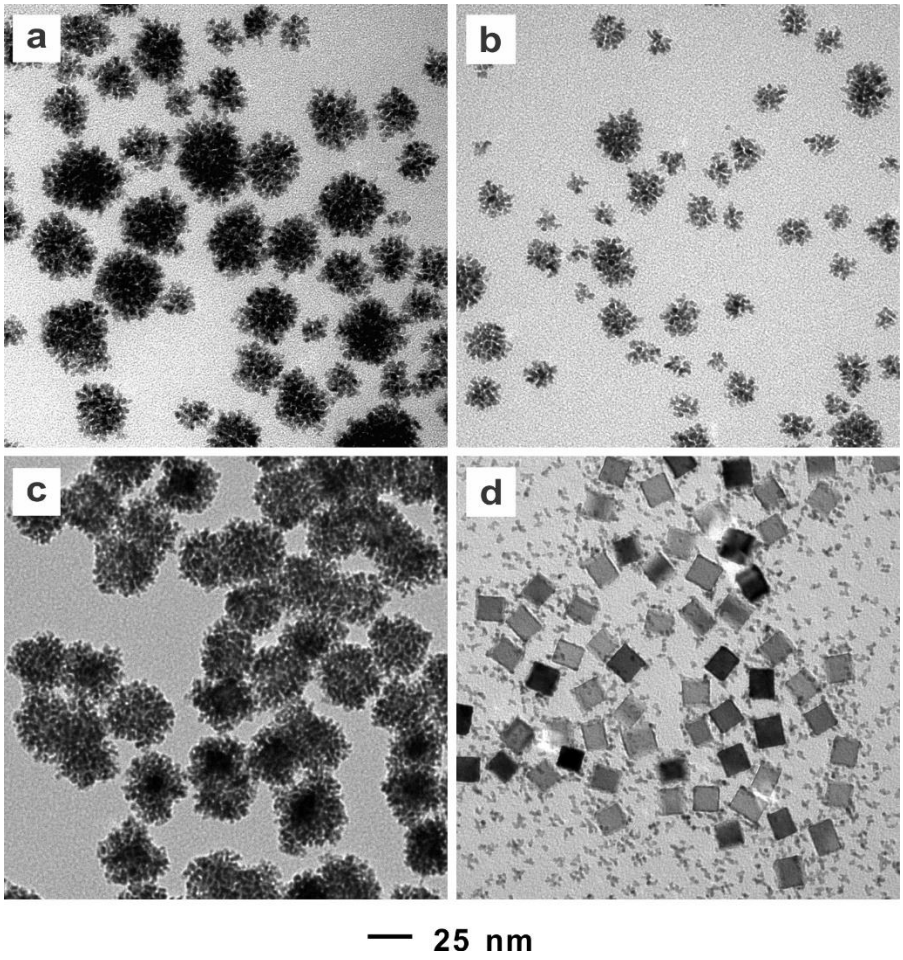

Figure 5.1. (a, b) TEM images of the products obtained when $PtCl_4^{2-}$ was reduced by AA at (a) 22 and (b) 100 °C, respectively, in the absence of pre-formed seeds. (c, d) TEM images of the products obtained by reducing $PtCl_4^{2-}$ with AA at (c) 22 and (d) 100 °C, respectively, in the presence of pre-formed Pd nanocubes as seeds.

To understand why products with different morphologies were formed at different reaction temperatures, I conducted a quantitative analysis of the reduction kinetics in an effort to elucidate the reduction pathway involved in the formation of Pt nanocrystals by following the methodology recently developed for the Pd system [12,13]. In general, the reduction of a Pt(II) precursor can also undergo two different pathways: solution-phase (eq. 1) *vs.* surface-based (eq. 2):

$$\mathrm{Pt(II)} + 2e^- \xrightarrow{k_1} \mathrm{Pt}^0 \qquad \text{(eq. 1)} \qquad \text{(solution reduction)}$$

$$\mathrm{Pt(II)} + \mathrm{Pt}_n^0 + 2e^- \xrightarrow{k_2} \mathrm{Pt}_{n+1}^0 \qquad \text{(eq. 2)} \qquad \text{(surface reduction)}$$

where Pt(II) is the precursor and Pt_n^0 represents the surface atoms on the nuclei or seeds. For solution reduction, the precursor ions are directly reduced to atoms in the solution phase. Surface reduction is an autocatalytic process, in which the precursor ions first adsorb onto the surface of the just-formed nuclei or pre-formed seeds and are then reduced to atoms. It is worth mentioning that the reducing agent can be assumed to take a more or less fixed concentration because it was used in large excess relative to the Pt(II) precursor. The total reduction rate of for Pt(II) precursor can thus be expressed as:

$$\text{rate} = k_1[\text{Pt(II)}] + k_2[\text{Pt(II)}][\text{Pt}_\text{n}^0] \qquad \text{(eq. 3)}$$

To quantitatively understand which reduction pathway was in dominance during the formation of Pt nanocrystals in the absence of pre-formed seeds, I used inductively-coupled plasma mass spectrometry (ICP-MS) to measure the concentration of Pt(II) remaining in the reaction solution at different time points (Figure 5.2a, b). As can be seen from Figure 5.2a, when the reduction was conducted at room temperature, the concentration of Pt(II) remained almost unchanged in the first 150 min and then underwent a sudden decrease. By fitting the experimental data with the Finke-Watzky model (eq. 3, see the Supporting Information for details) [14,15], I obtained a value of 2.97×10^{-6} min^{-1} for the rate constant k_1 (solution reduction), whereas the rate constant for surface reduction (k_2) was 2.89×10^{-2} min^{-1} mM^{-1}. When the reaction temperature was raised to 100 °C, the concentration of Pt(II) started to drop as soon as the reagents were mixed, and fitting to the experimental data gave values of 1.44 min^{-1} for k_1 and 3.05 min^{-1} mM^{-1} for k_2. Similar fittings were also carried out for the experimental data collected at other temperatures in the range of 22−100 °C, as shown in Figure 5.3.

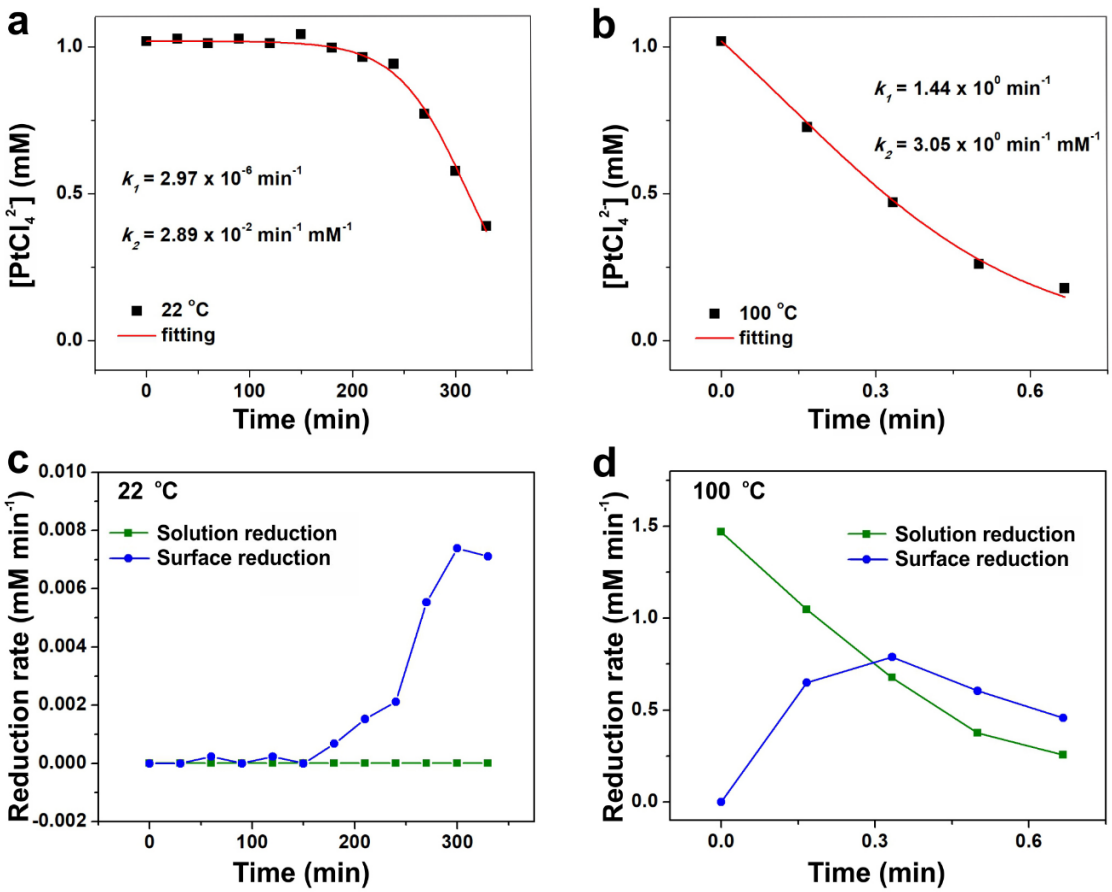

Figure 5.2. Quantitative analysis of the kinetic parameters for the reduction of Pt(II) precursors by AA at different reaction temperatures. (a, b) The concentration of $PtCl_4^{2-}$ precursor remaining in the reaction solution as a function of reaction time at two temperatures: (a) 22 °C and (b) 100 °C, respectively. The Finke−Watzky (F−W) model was used to fit the data for the reduction of $PtCl_4^{2-}$ precursor. (c, d) The rates of solution reduction and surface reduction for $PtCl_4^{2-}$ precursor as a function of reaction time corresponding to the data points in (a, b).

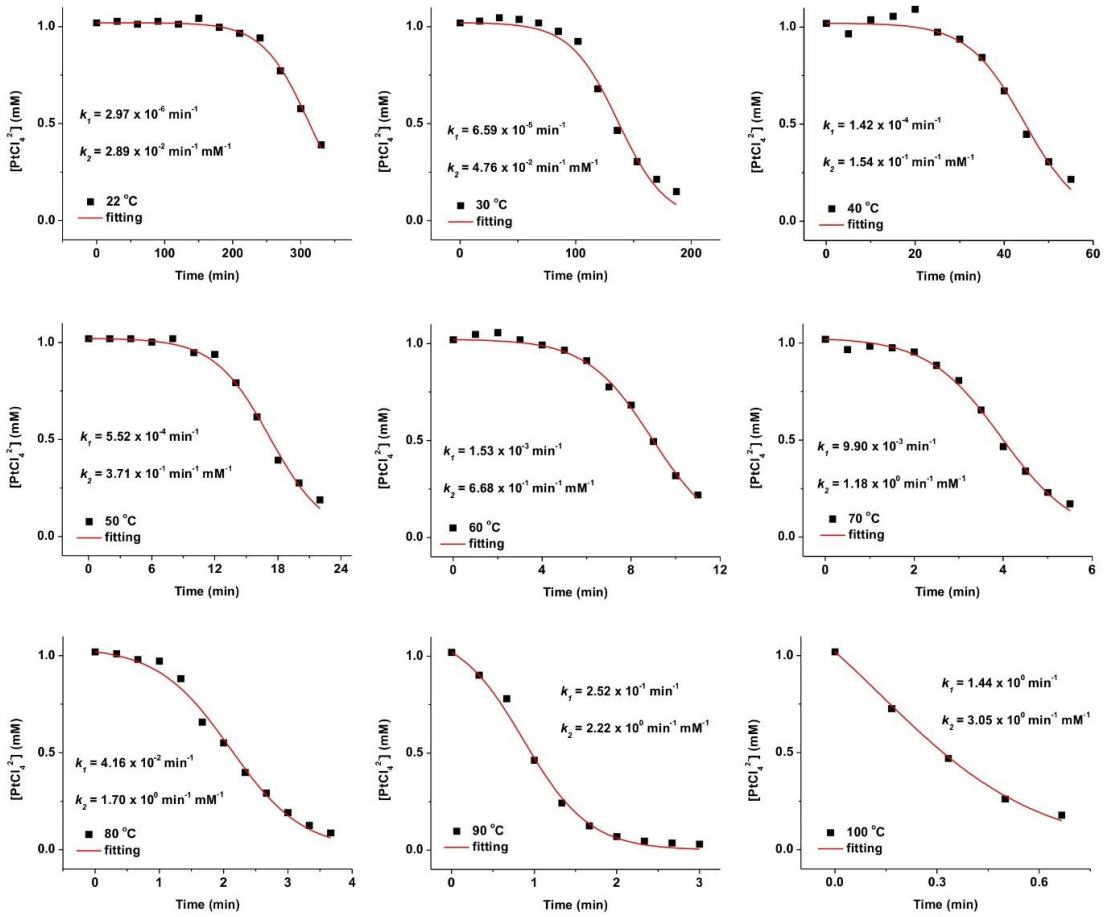

Figure 5.3. Plots showing the concentrations of Pt(II) precursor remaining in the reaction solutions as a function of time when the syntheses were conducted at different temperatures in the range of 22–100 °C in the absence of pre-formed seeds. The Finke-Watzky model was used to fit the data for the reduction of $PtCl_4^{2-}$ precursor by AA.

After acquiring the rate constants at each reaction temperature, I was able to calculate the reduction rate of each reduction pathway throughout the synthesis. As plotted in Figure 5.2c, d, both solution reduction and surface reduction occurred at very slow rates in the early stage of a synthesis conducted at 22 °C. Around 150 min into the synthesis, surface reduction was accelerated to take the dominance. In comparison, solution reduction and surface reduction occurred at much faster rates when the reaction temperature was raised to 100 °C, and solution reduction was in dominance during almost the entire span of the

synthesis. Only in a late stage did surface reduction become slightly faster than solution reduction.

Based on the kinetic analysis, I could now understand why the Pt nanocrystals took distinct morphologies when the syntheses were conducted at different temperatures. A schematic of the mechanism for the formation of Pt nanocrystals is shown in Figure 5.4a, b. When no pre-formed seeds were present, solution reduction followed by homogeneous nucleation, was the only possible pathway to generate Pt_n^0 nuclei and then seeds in the stage of nucleation (Figure 5.4a). After the formation of nuclei/seeds, the precursor could still be reduced in the solution and then deposited onto the nuclei/seeds for the growth. At the same time, the precursor could adsorb onto the surface of the nuclei/seeds and were then reduced through the autocatalytic surface reduction (Figure 5.4b). The proportions of these two reduction pathways are largely determined by the kinetics, which is highly dependent on the reaction temperature. When the reaction was conducted at a relatively low temperature such as 22 °C, both reduction pathways occurred at very slow rates and the majority of the reduction of the Pt(II) precursor was dominated by surface reduction (Figure 5.2c). Therefore, the number of nanocrystals formed was greatly reduced due to the limited events of homogeneous nucleation. Once the nuclei/seeds had been formed, the following reduction would preferentially occur on the surface of the nuclei/seeds for the nanocrystal to grow into larger sizes instead of generating additional nuclei/seeds. This led to the formation of relatively large assemblies of small Pt nanocrystals as the final products (Figure 5.1a). When the reaction temperature was increased to 100 °C, solution reduction was in dominance. The acceleration in solution reduction rate at the beginning of a synthesis resulted in more nuclei/seeds and thereby smaller assemblies of small

nanocrystals as the final products (Figure 5.1b). Additional TEM images showing assemblies of Pt nanocrystals obtained at other temperatures again confirm that the size of the assemblies decreased with the increase in reaction temperature (Figure 5.5). In the stage of growth, deposition of atoms derived from both surface and solution reduction can take place on the surface of the just-formed seeds, resulting in the formation of additional small nanocrystals attached to the surface of the seeds. Therefore, the final products were always assemblies of Pt nanocrystals no matter which reduction pathway was in dominance, but the size of the assemblies was significantly reduced when the contribution from solution reduction was increased and more nuclei/seeds were produced at the nucleation stage. The possible involvement of random aggregation of small Pt nanocrystals can be ruled out, otherwise the assemblies should take a larger size at a higher temperature as more small Pt nanocrystals were produced in the nucleation stage.

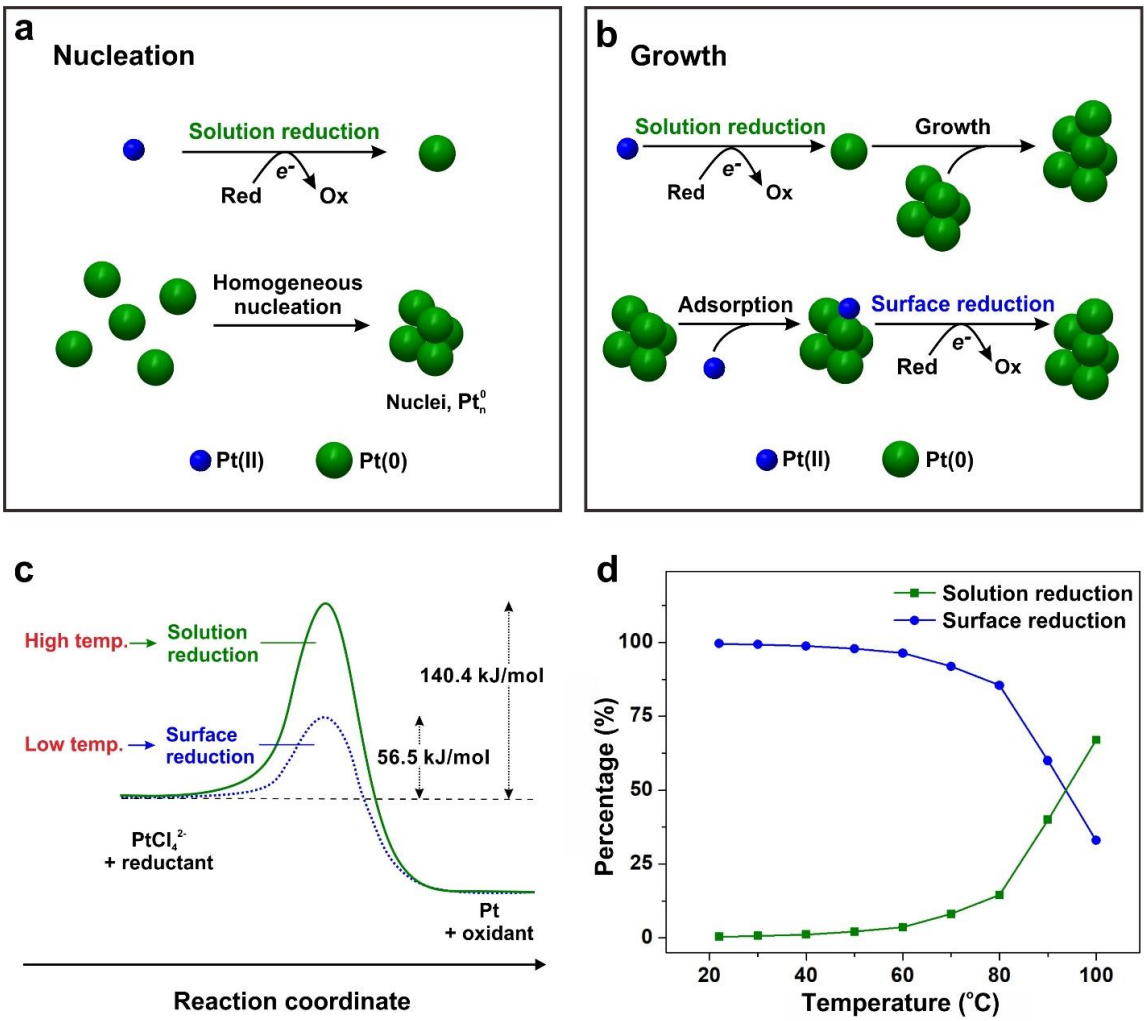

Figure 5.4. (a, b) Schematics showing the reduction pathways of a Pt(II) precursor in (a) nucleation and (b) growth stages, respectively, in the absence of pre-formed seeds. During nucleation, the Pt(II) precursor follows the solution reduction pathway to generate Pt atoms, followed by homogeneous nucleation to generate Pt_n^0 nuclei or seeds. During growth, the Pt(II) precursor undergoes either surface reduction or solution reduction to generate Pt atoms for their deposition onto the nuclei/seeds. (c) Potential energy diagrams corresponding to the conversion of Pt(II) ions to Pt atoms *via* two different pathways. (d) Temperature-dependent percentages of contributions of solution reduction and surface reduction, respectively, to the total reduction when the concentration of the Pt(II) precursor dropped from 1.02 to 0.5 mM.

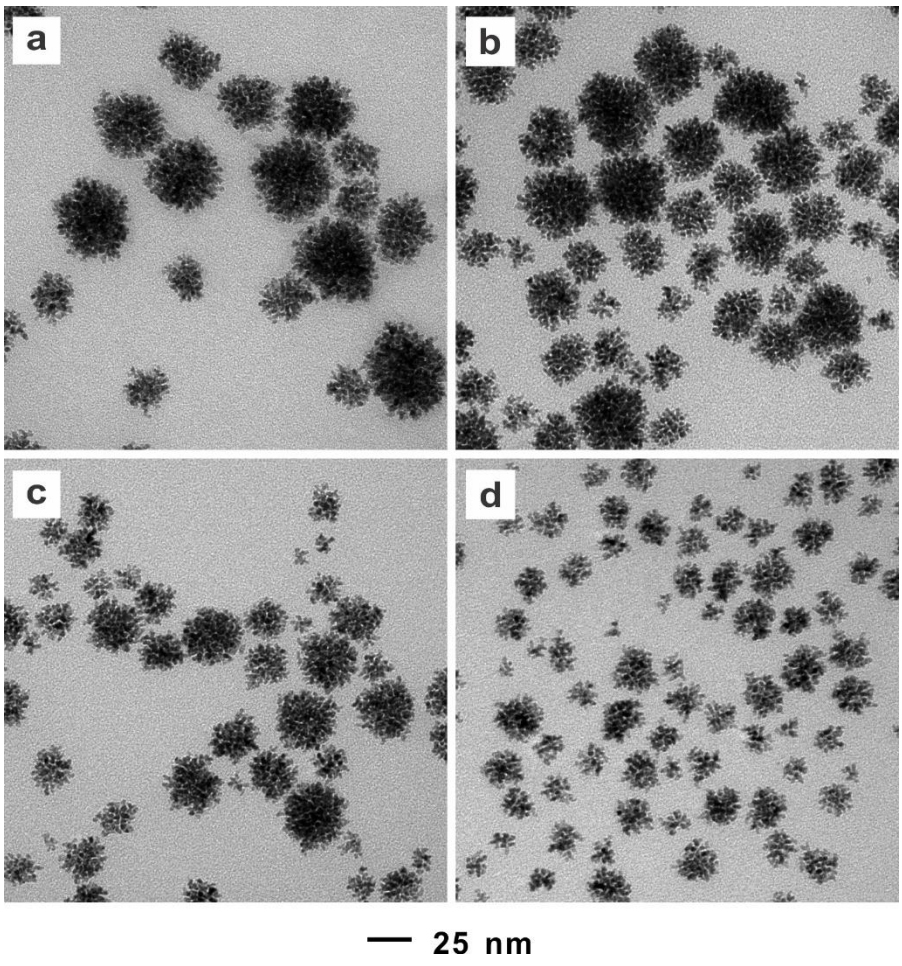

Figure 5.5. (a-d) TEM images of the products obtained when $PtCl_4^{2-}$ was reduced by AA at (a) 30, (b) 50, (c) 70, and (d) 90 °C, respectively, in the absence of pre-formed seeds.

When I switched to seed-mediated growth, a similar trend was also observed (Figure 5.1c, d). The small Pt nanocrystals were found to be exclusively attached to the surface of the Pd nanocube seeds at 22 °C, indicating limited homogeneous nucleation due to the suppression of solution reduction at a relatively low temperature. At 100 °C, small Pt nanocrystals were observed on the surface of the Pd nanocube seeds, but there was a relatively large proportion of assemblies of Pt nanocrystals in the solution, indicating the significant role of homogeneous nucleation caused by the acceleration in solution reduction kinetics.

Knowing the values of k_1 at k_2 at different reaction temperatures allowed us to calculate the activation energy of each reduction pathway [12]. By plotting lnk_1 and lnk_2 as a function of 1/T, the slope of the linear regression line could be used to calculate the activation energy of the reduction pathways using the Arrhenius equation (Figure 5.6). Figure 5.4c shows a potential energy diagram to illustrate the transformation of the Pt(II) precursor into elemental Pt through two different reduction pathways. The surface reduction has an activation energy of 56.5 kJ/mol, which is much lower than that (140.4 kJ/mol) of the solution reduction. Therefore, at low reaction temperatures, the reduction of the Pt(II) precursor prefers to undergo surface reduction due to the insufficient thermal energy to overcome the high energy barrier to solution reduction. Once the precursor ions have gained adequate thermal energy at high reaction temperatures, solution reaction will be preferred since the precursor ions can collide more frequently with the reducing agents than with the surface of nuclei/seed.

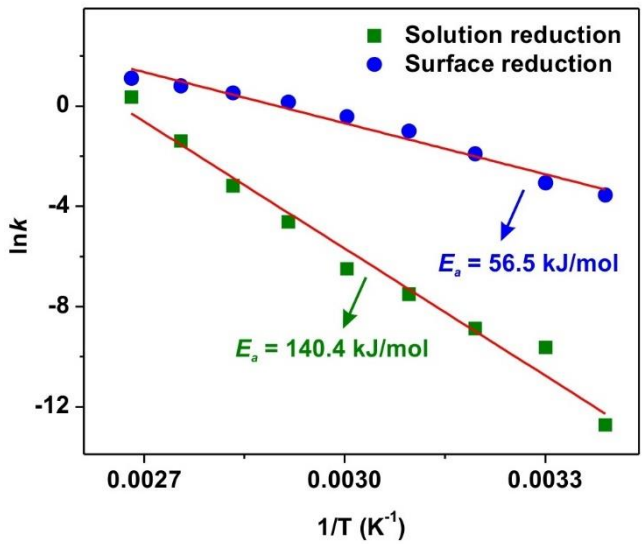

Figure 5.6. Determination of the activation energies for solution reduction and surface reduction, respectively. Plots showing lnk_1 and lnk_2 as a function of $1/T$ for solution reduction and surface reduction of $PtCl_4^{2-}$ precursor, where the slope of linear regression

line can be used to calculate the activation energy (E_a) of the corresponding reduction pathway using the Arrhenius equation.

The transition from surface reduction to solution reduction at elevated temperatures could be quantitatively compared by analyzing the contributions of these two reduction pathways to the total reduction of the Pt(II) precursor at different temperatures (Figure 5.4d). At low reaction temperatures (22–80 °C), more than 85% of the total reduction of the Pt(II) precursor underwent the surface reduction pathway. When the reaction temperature approached 90 °C, the contributions from surface reduction (60%) and solution reduction (40%) became comparable. The order was eventually reversed when the temperature was further raised to 100 °C. At this temperature, surface reduction only contributed 33% to the total reduction while solution reduction dominated the total reduction (67%). As can be seen from the plot, the temperature needed to switch the dominance of reduction pathway was around 93 °C.

5.3 Conclusion

In summary, I have quantitatively analyzed the reduction kinetics/pathway of $PtCl_4^{2-}$ by AA in the absence/presence of pre-formed seeds at different reaction temperatures. My results indicate that the Pt(II) precursor was exclusively reduced in the solution phase in the early stage of a synthesis for the generation of nuclei and then seeds through homogeneous nucleation regardless of the reaction temperature. During growth at a relatively low temperature (22–80 °C), the Pt(II) precursor preferentially adsorbed onto the surface of the seeds and was then reduced to atoms. When the temperature was greater than 90 °C, the Pt(II) precursor was preferentially reduced in the solution to generate Pt atoms for their subsequent deposition onto the seeds. Similar transition was also observed when

pre-formed Pd nanocubes were introduced into the reaction system to serve as seeds, in which surface reduction was in dominance at a low reaction temperature and solution reduction prevailed at a high reaction temperature. A quantitative understanding of the reduction kinetics and pathways of the Pt(II) precursor would offer insightful guidelines for the rational synthesis of Pt nanocrystals with controlled morphologies, in an effort to optimize their performance in various catalytic applications.

5.4 Experimental Section

Chemicals and materials. Sodium tetrachloropalladate (Na_2PdCl_4, ≥99.99%), potassium tetrachloroplatinate (K_2PtCl_4, ≥99.99%), L–ascorbic acid (AA, ≥99.0%), potassium bromide (KBr, ≥99.0%), and poly(vinylpyrrolidone) (PVP, $M_W \approx 55{,}000$) were all obtained from Sigma-Aldrich and used as received. Deionized (DI) water with a resistivity of 18.2 MΩ·cm at room temperature was used for all the experiments.

Quantitative analysis of the reduction kinetics of a Pt(II) precursor in the absence of seeds. I derived the reduction rate by analyzing the concentration of Pt(II) ions remaining in the reaction solution at different time points. For the synthesis of Pt nanocrystals, 8 mL of an aqueous solution containing 60 mg of AA and 100 mg of PVP were mixed in a 20-mL glass vial at a specific temperature of 22, 30, 40, 50, 60, 70, 80, 90, or 100 °C for 10 min under magnetic stirring. Next, 2.0 mL of aqueous $PtCl_4^{2-}$ (4.23 mg of K_2PtCl_4) was quickly added in one shot using a pipette. Meanwhile, the timer started running. An aliquot of 0.2 mL was sampled from the reaction solution at each time point (see Table 5.1) and immediately injected into 0.8 mL of aqueous KBr (500 mg/mL) to quench the reduction and thereby preserve the concentration of Pt(II) ions. Due to the use

of an excess amount of KBr, the Pt(II) ions were supposed to exist in the form of $PtBr_4^{2-}$. Then, the solution was centrifuged at 17,500 rpm for 30 min to precipitate out all the Pt nanocrystals, leaving behind Pt(II) ions in the supernatant for ICP-MS analysis. The Pt nanocrystals collected at the end of the reaction (see Table 5.1 for the reaction time for each temperature) were used for TEM imaging.

Table 5.1. Experimental parameters used for measuring the reduction kinetics of a Pt(II) precursor in the synthesis of Pt nanocrystals at different reaction temperatures.

	solvent	Pt precursor	Precursor injection	Reductant	Surfactant	Temperature	Reaction time /interval time
1	Water/ 10 ml	K_2PtCl_4/ 4.23 mg	one shot	AA/ 60mg	PVP/ 100 mg	100 °C	40 s/ 10 s
2	Water/ 10 ml	K_2PtCl_4/ 4.23 mg	one shot	AA/ 60mg	PVP/ 100 mg	90 °C	180 s/ 20 s
3	Water/ 10 ml	K_2PtCl_4/ 4.23 mg	one shot	AA/ 60mg	PVP/ 100 mg	80 °C	220 s/ 20 s
4	Water/ 10 ml	K_2PtCl_4/ 4.23 mg	one shot	AA/ 60mg	PVP/ 100 mg	70 °C	5.5 min/ 0.5 min
5	Water/ 10 ml	K_2PtCl_4/ 4.23 mg	one shot	AA/ 60mg	PVP/ 100 mg	60 °C	11 min/ 1min
6	Water/ 10 ml	K_2PtCl_4/ 4.23 mg	one shot	AA/ 60mg	PVP/ 100 mg	50 °C	22 min/ 2 min
7	Water/ 10 ml	K_2PtCl_4/ 4.23 mg	one shot	AA/ 60mg	PVP/ 100 mg	40 °C	55 min/ 5 min

Table 5.1. Experimental parameters used for measuring the reduction kinetics of a Pt(II) precursor in the synthesis of Pt nanocrystals at different reaction temperatures (continued).

	solvent	Pt precursor	Precursor injection	Reductant	Surfactant	Temperature	Reaction time /interval time
8	Water/ 10 ml	K_2PtCl_4/ 4.23 mg	one shot	AA/ 60mg	PVP/ 100 mg	30 °C	187 min/ 17 min
9	Water/ 10 ml	K_2PtCl_4/ 4.23 mg	one shot	AA/ 60mg	PVP/ 100 mg	22 °C	330 min/ 30 min

Preparation of 18-nm Pd nanocubes to be used as the seeds. The Pd cubic seeds with an edge length of 18 nm were synthesized using a previously reported protocol with some minor modifications [12]. Typically, 8 mL of an aqueous solution containing PVP (105 mg), AA (60 mg), and KBr (600 mg) was thoroughly mixed in a 20-mL vial at 80 °C under magnetic stirring for 10 min, then 3 mL of aqueous Na_2PdCl_4 (64.6 mM) was quickly added in one shot using a pipette. The vial was then capped and maintained at 80 °C for 3 h. After centrifugation and washing with water three times, the Pd seeds were dispersed in water for further use.

Seed-mediated growth of Pd-Pt nanocrystals. In a standard synthesis, 8 mL of an aqueous solution containing 60 mg of AA, 100 mg of PVP, 0.36 mg Pd nanocube seeds were mixed in a 20-mL glass vial at a specific temperature (22 or 100 °C) for 10 min under magnetic stirring. Next, 2 mL of aqueous $PtCl_4^{2-}$ (4.23 mg of K_2PtCl_4) was quickly added in one shot using a pipette. The reaction time was chosen to be the same as in the synthesis

without the involvement of pre-formed seeds. The reaction solution was centrifuged at 17,500 rpm for 30 min to precipitate out all the Pd-Pt nanocrystals for TEM characterizations.

Characterization methods. Transmission electron microscopy (TEM) images were taken using a Hitachi HT7700 microscope operated at 120 kV. The concentrations of Pt(II) were determined using an inductively-coupled plasma mass spectrometer (ICP-MS, NexION 300Q, PerkinElmer, Waltham, MA).

Calculation of the rate constants for solution reduction (k_1) and surface reduction (k_2) in the absence of pre-formed seeds based on the Finke−Watzky model [12-15].

$$\mathrm{Pt(II)} + 2e^- \xrightarrow{k_1} \mathrm{Pt}^0,\ n\mathrm{Pt}^0 \xrightarrow{homogeneous\ nucleation} \mathrm{Pt}_n^0 \qquad \text{(eq. S1)}$$

(solution reduction and homogeneous nucleation)

$$\mathrm{Pt}_n^0 + \mathrm{Pt(II)} + 2e^- \xrightarrow{k_2} \mathrm{Pt}_{n+1}^0 \qquad \text{(eq. S2)}$$

(surface reduction on the just-formed nuclei)

where Pt(II) is the precursor, and Pt_n^0 represents the surface atoms of the just-formed nuclei. The overall rate for the kinetically important steps (S1) and (S2) can be written as

$$\frac{-\mathrm{d}[\mathrm{Pt}^{2+}]}{\mathrm{d}t} = k_1[\mathrm{Pt(II)}] + k_2[\mathrm{Pt(II)}][\mathrm{Pt}_n^0] \qquad \text{(eq. S3)}$$

By implementing $[\mathrm{Pt}_n^0] = [\mathrm{Pt(II)}]_0 - [\mathrm{Pt(II)}]$, I obtain the following equation, which can be further integrated:

$$\frac{-\mathrm{d}[\mathrm{Pt(II)}]}{\mathrm{d}t} = k_1[\mathrm{Pt(II)}] + k_2[\mathrm{Pt(II)}]([\mathrm{Pt(II)}]_0 - [\mathrm{Pt(II)}])$$

$$\int_{[\mathrm{Pt(II)}]_0}^{[\mathrm{Pt(II)}]} \frac{-\mathrm{d}[\mathrm{Pt(II)}]}{[\mathrm{Pt(II)}](k_1 + k_2([\mathrm{Pt(II)}]_0 - [\mathrm{Pt(II)}]))} = \int_0^t \mathrm{d}t$$

$$\ln\left[\frac{(k_1 + k_2([\mathrm{Pt(II)}]_0 - [\mathrm{Pt(II)}]))[\mathrm{Pt(II)}]_0}{k_1[\mathrm{Pt(II)}]}\right] = (k_1 + k_2[\mathrm{Pt(II)}]_0) * t$$

Expressing the above equation in the exponential format yields the desired equation (4):

$$[\mathrm{Pt(II)}]_t = \frac{\frac{k_1}{k_2} + [\mathrm{Pt(II)}]_0}{1 + \frac{k_1}{k_2[\mathrm{Pt(II)}]_0} * \exp((k_1 + k_2[\mathrm{Pt(II)}]_0) * t)} \qquad \text{(eq. S4)}$$

5.5 Notes to Chapter 5

Part of this chapter is adapted from the paper "Quantitative Analysis of the Reduction Kinetics of a Pt(II) Precursor in the Context of Pt Nanocrystal Synthesis" accepted by *Chinese Journal of Chemical Physics* [16].

5.6 References

(1) Xia, Y.; Xiong, Y.; Lim, B.; Skrabalak, S. E. *Angew. Chem. Int. Ed.* **2009**, *48*, 60–103.

(2) Xia, Y.; Xia, X.; Peng, H.-C. *J. Am. Chem. Soc.* **2015**, *137*, 7947–7966.

(3) Xia, Y.; Gilroy, K. D.; Peng, H.-C.; Xia, X. *Angew. Chem. Int. Ed.* **2017**, *56*, 60–95.

(4) Zhang, L.; Roling, L. T.; Wang, X.; Vara, M.; Chi, M.; Liu, J.; Choi, S.-I.; Park, J.; Herron, J. A.; Xie, Z.; Mavrikakis, M.; Xia, Y. *Science.* **2015**, *349*, 412–416.

(5) Wang, X.; Choi, S.-I.; Roling, L. T.; Luo, M.; Ma, C.; Zhang, L.; Chi, M.; Liu, J.; Xie, Z.; Herron, J. A.; Mavrikakis, M.; Xia, Y. *Nat. Commun.* **2015**, *6*, 7594.

(6) Tsung, C.-K.; Kuhn, J. N.; Huang, W.; Aliaga, C.; Hung, L.-I.; Somorjai, G. A.; Yang, P. *J. Am. Chem. Soc.* **2009**, *131*, 5816–5822.

(7) Chen, W.; Ji, J.; Feng, X.; Duan, X.; Qian, G.; Li, P.; Zhou, X.; Chen, D.; Yuan, W. *J. Am. Chem. Soc.* **2014**, *136* (48), 16736–16739.

(8) Chen, J.; Lim, B.; Lee, E. P.; Xia, Y. *Nano Today* **2009**, *4* (1), 81–95.

(9) Peng, Z.; Yang, H. *Nano Today* **2009**, *4* (2), 143–164.

(10) Wang, X.; Figueroa-Cosme, L.; Yang, X.; Luo, M.; Liu, J.; Xie, Z.; Xia, Y. *Nano Lett.* **2016**, *16* (2), 1467–1471.

(11) Yang, T.-H.; Gilroy, K. D.; Xia, Y. *Chem. Sci.* **2017**, *8*, 6730–6749.

(12) Yang, T.-H.; Peng, H.-C.; Zhou, S.; Lee, C.-T.; Bao, S.; Lee, Y.-H.; Wu, J.-M.; Xia, Y. *Nano Lett.* **2017**, *17* (1), 334–340.

(13) Yang, T.-H.; Zhou, S.; Gilroy, K. D.; Figueroa-Cosme, L.; Lee, Y.-H.; Wu, J.-M.; Xia, Y. *Proc. Natl. Acad. Sci. U. S. A.* **2017**, *114* (52), 13619–13624.

(14) Watzky, M. A.; Finke, R. G. *J. Am. Chem. Soc.* **1997**, *119* (43), 10382–10400.

(15) Besson, C.; Finney, E. E.; And; Finke, R. G. *Chem. Mater.* **2005**, *17* (20), 4925–4938.

(16) Zhou, S.; Yang, T.H.; Zhao, M.; Xia, Y. *Chin. J. Chem. Phys.* **2018**, accepted.

CHPATER 6

CONCLUSIONS AND FUTURE DIRECTIONS

6.1 Conclusions

This dissertation covers several strategies for controlling the size, shape and surface properties of noble-metal nanocrystals. I began by developing an aqueous protocol for the one-pot synthesis of Ag nanocubes with an average edge length of 35-95 nm. Upon mixing CTAC with CF_3COOAg, AgCl nanoscale octahedra were immediately formed. The presence of room light and a reducing agent such as ascorbic acid offered a proper reducing power to generate the Ag_n nuclei and to continuously provide elemental Ag for the evolution of Ag_n nuclei into Ag nanocubes. The capping of {100} facets by Cl^- ions and the use of relatively low reaction temperature were both critical to retaining the sharp corners and edges on the Ag nanocubes. This synthetic method is appealing for bio-related applications, as well as plasmonic and SERS-based sensing, due to the involvement of aqueous solutions only. It also offers a more reproducible, environmentally friendly, and economical route to the synthesis of Ag nanocubes as compared to the widely used polyol process.

To further increase the purity of Ag nanocubes and to obtain Ag nanocubes at smaller sizes, I developed a seed-mediated protocol for the synthesis of small Ag nanocubes with sharp corners and edges in an aqueous system at room temperature. The colloidal stabilization capability, the specific binding towards {100} facets, and the strength of oxidative etching caused by the capping agent all played an essential role in sharpening the corners and edges of Ag cubic seeds in a site-selective fashion. Once the corners and edges

were sharpened, the seed-mediated growth underwent symmetry breaking or reduction, leading to the formation of Ag nanobars with aspect ratios up to 2. The sharpened Ag nanocubes can also serve as better sacrificial template for the fabrication of Au nanocages compared to the truncated counterpart. This research offers insights into the site-selective growth and symmetry breaking phenomena in nanocrystal growth. Compared to the more widely used polyol reduction, this synthetic method offers a milder and more environmentally friendly protocol.

After designing two synthetic protocols to achieve shape-control synthesis of noble-metal nanocrystals, I further developed an indirect ligand exchange method to precisely control the surface properties of Au nanocrystals. The method involved the deposition of an ultrathin layer of Ag to remove a strong capping agent such as CTAC from the surface of the Au nanocrystals. Subsequently, selective etching of the Ag layer allowed us to introduce citrate ions onto the surface of the nanocrystals. The complete ligand replacement was confirmed by multiple characterization techniques. Different from the conventional direct ligand exchange, this indirect method offers a facile and quick means to completely replace a strong ligand with an oppositely charged, weak ligand, and provides opportunities to modify nanocrystals with bio-benign surface groups for various applications.

Finally, I quantitatively analyzed the reduction kinetics of $PtCl_4^{2-}$ by AA in the absence/presence of pre-formed seeds at different reaction temperatures. Our results indicate that the Pt(II) precursor was exclusively reduced in the solution phase in the early stage of a synthesis for the generation of nuclei and then seeds through homogeneous nucleation regardless of the reaction temperature. During growth at a relatively low temperature (22–80 °C), the Pt(II) precursor preferentially adsorbed onto the surface of the

seeds and was then reduced to atoms. When the temperature was greater than 90 °C, the Pt(II) precursor was preferentially reduced in the solution to generate Pt atoms for their subsequent deposition onto the seeds. Similar transition was also observed when pre-formed Pd nanocubes were introduced into the reaction system to serve as seeds, in which surface reduction was in dominance at a low reaction temperature and solution reduction prevailed at a high reaction temperature. A quantitative understanding of the reduction kinetics and pathways of the Pt(II) precursor would offer insightful guidelines for the rational synthesis of Pt nanocrystals with controlled morphologies, in an effort to optimize their performance in various catalytic applications.

My research has advanced the synthesis of colloidal metal nanocrystals through careful experimental design, reduction kinetics analysis, and post-synthesis ligand exchange to control both the shape and surface properties of noble-metal nanocrystals.

6.2 Future Directions

The methods described in this dissertation aim to control the evolution of noble-metal nanocrystals with well-defined shapes and surface properties. Despite all the accomplishments I have achieved, there are still new directions to pursue.

Firstly, the water-based synthetic methods for the synthesis of Ag nanocubes can only produce nanocrystals less than 0.1 mg per batch of reaction. In order to use them as sacrificial materials to fabricate Au nanocages and/or use them as catalysts for reactions such as ethylene epoxidation, it is essential to develop strategies for scaling-up the production from milligram to the gram and kilogram level without sacrificing the quality control and significantly extending the time involved. To this end, droplet reactors are

promising in enabling the mass production of metal nanocrystals as our group has demonstrated for the case of Ag nanocubes using the polyol synthesis [1]. A similar system can be further extended to scale up the water-based synthesis of Ag nanocubes.

As mentioned above, the surface properties of noble-metal nanocrystals can significantly influence their performances in photonics, catalysis and biomedicine. In addition to controlling the surface properties of Au nanocrystals, it would be interesting to extend the indirect ligand exchange method to achieve complete ligand replacement on the surface of other noble-metal nanocrystals made of Ag, Pt, and Pd or even other types of inorganic nanocrystals. For example, semiconductor kesterite Cu_2ZnSnS_4 nanocrystals are often capped by oleic acid or oleylamine from the synthesis [2]. However, the insulating nature of these ligands limits the charge transport between the particles in application such as optoelectronic devices. Thus, the bulky ligands should be replaced by short organic ligands such as 1,2-ethylenediamine and 1,2-ethanedithiol to favor the increase of photoconductivity and carrier mobility. It is also possible to use Ag deposition and etching without introducing a second ligand to obtain nanocrystals with a clean surface to fully expose their active sites for catalysis.

Finally, the quantitative understanding of how reduction kinetics influence the resultant nanocrystals is still at its emerging phase. Similar methods can be extended to the one-pot synthesis of other Pt nanocrystals with well-defined shapes and sizes, and then to the seed-mediated growth of Pt nanocrystals. It is also unclear how to determine the reduction kinetics of high-valent precursor compounds such as $PtCl_6^{2-}$. The possible coexistence of $PtCl_6^{2-}$ and $PtCl_4^{2-}$ during the reduction can complicate the story, and more advanced mathematical models are needed to help determine the reduction kinetics of such

high-valent precursors [3]. A better understanding of the reduction kinetics can greatly advance the field of nanocrystal synthesis from the trial-and-error approach toward a more predictable research.

6.3 Notes to Chapter 6

Parts of this chapter are adapted from "Facile Synthesis of Silver Nanocubes With Sharp Corners and Edges in an Aqueous Solution" published in *ACS Nano* [4], "Site-selective Growth of Ag Nanocubes for Sharpening Their Corners and Edges, Followed by Elongation into Nanobars through Symmetry Reduction" published in *Journal of Materials Chemistry C* [5], "Enabling Complete Ligand Exchange on the Surface of Gold Nanocrystals through the Deposition and then Etching of Silver" recently submitted for publication, and "Quantitative Analysis of the Reduction Kinetics of a Pt(II) Precursor in the Context of Pt Nanocrystal Synthesis" accepted by *Chinese Journal of Chemical Physics* [6]. All of these publications were co-authored by me.

6.4 References

(1) Zhang, L.; Wang, Y.; Tong, L.; Xia, Y. *Langmuir* **2013**, *29*, 15719–15725.

(2) Zhang, Z.-X.; Zheng-Ji, Z.; Bing, B.; Ming-Hua, L.; Wen-Hui, Z.; Dong-Xing, K.; Wu, S.-X. *J. Nanoparticle Res.* **2015**, *17*, 463.

(3) Yang, T.-H.; Gilroy, K. D.; Xia, Y. *Chem. Sci.* **2017**, *8*, 6730–6749.

(4) Zhou, S.; Li, J.; Gilroy, K. D.; Tao, J.; Zhu, C.; Yang, X.; Sun, X.; Xia, Y. *ACS Nano* **2016**, *10*, 9861–9870.

(5) Zhou, S.; Mesina, D. S.; Organt, M. A.; Yang, T.-H.; Yang, X.; Huo, D.; Zhao, M.; Xia, Y. *J. Mater. Chem. C* **2018**, *6*, 1384–1392.

(6) Zhou, S.; Yang, T.H.; Zhao, M.; Xia, Y. *Chin. J. Chem. Phys.* **2018**, accepted.